

MEASUREMENT OF THE NEUTRON
(^3He) SPIN STRUCTURE AT LOW
 Q^2 AND THE EXTENDED
GERASIMOV-DRELL-HEARN SUM
RULE

Ioannis Kominis

A DISSERTATION
PRESENTED TO THE FACULTY
OF PRINCETON UNIVERSITY
IN CANDIDACY FOR THE DEGREE
OF DOCTOR OF PHILOSOPHY

RECOMMENDED FOR ACCEPTANCE
BY THE DEPARTMENT OF
PHYSICS

JANUARY 2001

© Copyright 2001 by Ioannis Kominis.

All rights reserved.

Abstract

This thesis presents the results of E-94010, an experiment at Thomas Jefferson National Accelerator Facility (TJNAF) designed to study the spin structure of the neutron at low momentum transfer, and to test the "extended" Gerasimov-Drell-Hearn (GDH) sum rule. The first experiment of its kind, it was performed in experimental Hall-A of TJNAF using a new polarized ^3He facility.

It has recently been shown that the GDH sum rule and the Bjorken sum rule are both special examples of a more general sum rule that applies to polarized electron scattering off nucleons. This generalized sum rule, due to Ji and Osborne, reduces to the GDH sum rule at $Q^2 = 0$ and to the Bjorken sum rule at $Q^2 \gg 1 \text{ GeV}^2$. By studying the Q^2 evolution of the extended GDH sum, one learns about the transition from quark-like behavior to hadronic-like behavior.

We measured inclusive polarized cross sections by scattering high energy polarized electrons off the new TJNAF polarized ^3He target with both longitudinal and transverse target orientations. The high density ^3He target, based on optical pumping and spin exchange, was used as an effective neutron target. The target maintained a polarization of about 35% at beam currents as high as $15\mu\text{A}$. We describe the precision ^3He polarimetry leading to a systematic uncertainty of the target polarization of 4% (relative). A strained GaAs photocathode was utilized in the polarized electron gun, which provided an electron beam with a polarization of about 70%, known to 3% (relative).

By using six different beam energies (between 0.86 and 5.06 GeV) and a fixed scattering angle of 15.5° , a wide kinematic coverage was achieved, with $0.02 \text{ GeV}^2 < Q^2 < 1 \text{ GeV}^2$ and $0.5 \text{ GeV} < W < 2.5 \text{ GeV}$ for the squared momentum transfer and invariant mass, respectively. From the measured cross sections we extract the ^3He spin structure functions $g_1^{^3\text{He}}$ and $g_2^{^3\text{He}}$. Finally, we determine the extended GDH sum for the range $0.1 \text{ GeV}^2 < Q^2 < 1 \text{ GeV}^2$ for ^3He and the neutron.

Acknowledgments

There has been a very large number of people who contributed to my training during the last four years and an equally large number of people who made possible the experiment that this thesis is concerned with. I am deeply grateful to all of them, and I am really pleased to have worked and to have been associated with them. A specific order in acknowledging those people individually would imply an order of importance, which is aesthetically unpleasing and far from reality. The interactions among a large group of people involved in learning the ropes of experimental physics and at the same time in making an experiment happen are quite complex, and therefore difficult to order. Up to this point the acknowledgement section exhibits a nice symmetry in the people-space. However, as happens with most symmetries in nature, this symmetry will be broken. It will be broken along the axis defined by Gordon Cates. Being my advisor, he has been the single most influential person in my graduate student career. I can not resist from expressing my deep appreciation for his support, his contribution to my training, and his responsibility for me feeling the joy and fulfillment that the last four breathtaking years brought about.

*Στους γονείς μου,
Κωνσταντίνο και Φωτεινή Κομίνη,
με τα θερμά μου συγχαρητήρια
για τον υιό τους.*

Contents

Abstract	iii
	iv
Acknowledgments	v
	vi
	viii
1 Introduction	1
1.1 Electron Scattering	1
1.2 Polarization Degrees of Freedom	5
1.3 Low Q^2 Region	6
1.3.1 The Gerasimov-Drell-Hearn (GDH) Sum Rule	7
1.4 Connection between the GDH and the Bjorken Sum Rules	7
1.5 The Significance of Neutron Spin Structure	7
1.5.1 DIS Limit	8
1.5.2 Low Q^2 Limit	8
1.5.3 Theoretical Inconsistencies with the Neutron	8
1.6 ^3He as an effective neutron target	8
1.7 Experiment E-94010	10
2 Theoretical Foundation of Experimental Observables	14
2.1 Polarized Electron Scattering	14
2.2 DIS Limit : Parton Model and Sum Rules	15
2.2.1 Parton Model	15

2.2.2	Sum Rules	16
2.3	$Q^2 = 0$ Limit : Gerasimov-Drell-Hearn Sum Rule	19
2.3.1	Forward Compton Scattering Amplitudes	21
2.4	Bridging the gap between $Q^2 = 0$ and $Q^2 = \infty$	23
2.4.1	Operator Product Expansion and Higher Twists: Bridging the gap from above	23
2.4.2	Generalized GDH Integral	24
2.4.3	Bridging the gap from below: Chiral Perturbation Theory	24
2.4.4	Unitary Isobar Model	26
3	Experimental Apparatus	29
3.1	The Accelerator and the Polarized Electron Source	29
3.2	Beam Energy Measurement	31
3.2.1	Introduction	31
3.2.2	Arc Measurement	31
3.2.3	E-P Measurement	32
3.2.4	$e^{-3}\text{He}$ Measurement	33
3.3	Hall-A Beamline	34
3.4	Beam Current Measurement	34
3.4.1	Effect of the Charge Uncertainty on Polarized Cross Section Differences	35
3.5	Beam Raster and Beam Position Monitors	36
3.6	Electron Beam Polarimetry	36
3.6.1	Møller Polarimetry	36
3.7	The Polarized ^3He Target	40
3.7.1	The Laser System	41
3.7.2	The Target Ladder	41
3.8	The High Resolution Spectrometers	43
3.9	The Detector Package	44
3.9.1	The Scintillators and the Trigger Setup	45
3.9.2	The Vertical Drift Chambers	46
3.9.3	Electron-Pion Separation	48

4	The Polarized ^3He Target	57
4.1	Introduction	57
4.2	Alkali Metal Optical Pumping	58
4.3	^3He Polarization Evolution	61
4.4	^3He Relaxation Mechanisms	62
4.4.1	Dipolar and Wall Relaxation	62
4.4.2	Relaxation due to Holding Field Inhomogeneity	63
4.4.3	Beam Induced Relaxation	63
4.5	Target Cells	65
4.5.1	Cell Construction	65
4.5.2	Cell Volumes	67
4.5.3	Cell Densities	68
4.5.4	Target Chamber Window Thicknesses	71
4.6	^3He Polarimetry	73
4.6.1	AFP as Polarization Monitor	73
4.6.2	Water Polarimetry	76
4.6.3	EPR Polarimetry	81
5	Data Analysis and Results	91
5.1	Data Acquisition and Replay	91
5.2	Extraction of Polarized Cross Sections from the Data	92
5.3	Spectrometer Optics and Acceptance	93
5.4	Elastic Cross Sections and Asymmetries	94
5.4.1	Elastic Cross Sections	94
5.4.2	Elastic Yield in Reference Cell Data	95
5.4.3	Elastic Asymmetries	97
5.5	Radiative Corrections	98
5.5.1	External Radiative Effects	99
5.5.2	Internal Radiative Effects	99
5.5.3	Iteration	99
5.5.4	Unpolarized Cross Sections	100
5.6	Extraction of $g_1^{^3\text{He}}$ and $g_2^{^3\text{He}}$	101

5.7	Extraction of Neutron Observables from ^3He Observables	107
5.7.1	Spin Structure Functions	107
5.7.2	Generalized GDH Integral	108
5.8	Measurement of GDH Integral	109
5.9	Summary and Outlook	109
A	Particle Identification Cuts and Efficiencies	114
B	Target Cell Volumes	118
C	Target Cell Densities	119

Introduction

1.1 Electron Scattering

Electron scattering has been a unique tool for the investigation of the structure of matter and its fundamental constituents since the beginning of this century.

Indeed, one of the milestone experiments that established the quantum theory of the atom, was the Franck-Hertz experiment in 1914. Albeit at an energy of a few eV, it was an electron scattering experiment with the electrons being accelerated by a grid in a glass tube and scattered off an atomic vapor, like mercury. Figure 1.1 displays some typical data showing the dependence of the detected electron current on the grid voltage. This is to be compared with the data taken eight decades later, by scattering electrons of 3 GeV energy, off protons (Figure 1.2).

It is the simultaneous evolution of the

instrumentation and the fundamental theories of subatomic physics that made the investigation of the structure of matter at such distance scales possible. Electron-hadron scattering

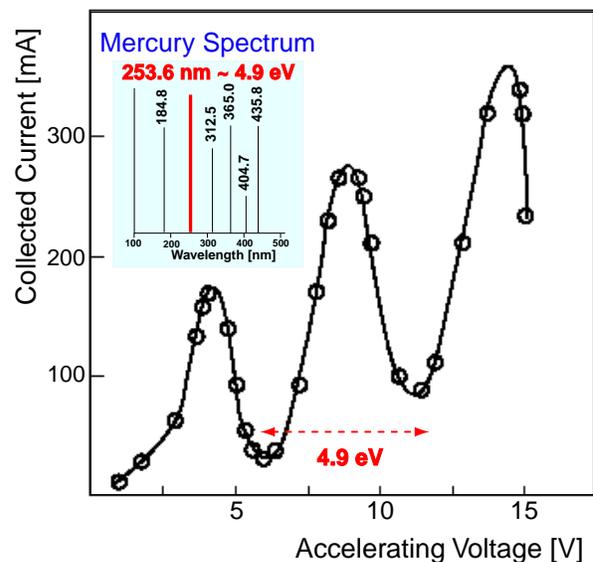


Figure 1.1: Franck-Hertz data for mercury, from [1].

as a probe of hadronic matter has the advantage that the governing electromagnetic interaction is weak, unlike hadron-hadron scattering [3]. At the same time it is strong enough, unlike neutrino-hadron scattering, that reasonable event rates can be achieved. Thus (neglecting for the moment radiative corrections) the vast majority of inclusive electron-hadron scattering experiments are described assuming the validity of the Born approximation, i.e. the one photon-exchange Feynman diagram shown in Figure 1.3,

where k_μ and s_μ (k'_μ and s'_μ) are the four-momentum and spin four-vector of the incident (scattered) electron, respectively. Similarly, P_μ and S_μ refer to the target nucleon (or nucleus), and X represent the undetected hadronic debris. The quantities measured in the laboratory in the inclusive scattering $A(e, e')X$ are the incident and scattered electron energies, E and E' , and the laboratory scattering angle θ . The electron-photon vertex is known from QED, whereas the unknown photon-nucleon vertex depends on two kinematic quantities, which are usually chosen to be the square

of the 4-momentum of the virtual photon, $Q^2 = -q^2$ and $\nu = q \cdot P/M$, where M is the target mass. In the laboratory frame (neglecting the electron mass, $m_e \ll E$)

$$Q^2 = 4EE' \sin^2 \theta / 2 \quad (1.1)$$

and ν is the electron energy loss :

$$\nu = E - E' . \quad (1.2)$$

Instead of ν , the variable x is often used, where $x = Q^2 / 2M\nu$. In the parton model, x represents the fraction of the nucleon momentum carried by the struck

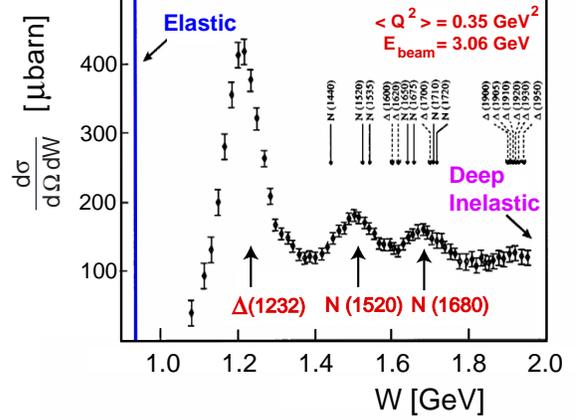


Figure 1.2: Electron-proton inclusive scattering cross section, from [2].

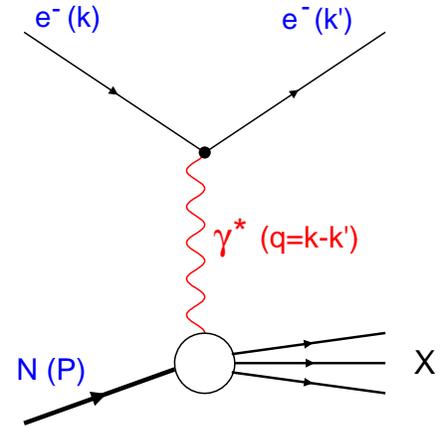


Figure 1.3: One photon approximation of e - N scattering.

parton. The invariant mass of the hadronic products of the scattering (X) is defined as

$$W^2 = (P + q)^2 = M^2 - Q^2 + 2M\nu \quad (1.3)$$

For elastic scattering off a nucleon $W = M$ and thus $x = 1$, whereas for scattering off a nucleus with A nucleons, $x = A$.

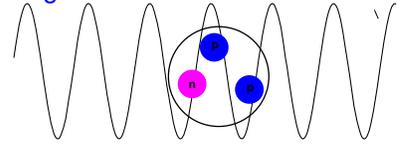
The advantage of describing the scattering process with the Born approximation is that in the cross section, the electron current

is clearly separated from the hadron current being probed. Furthermore, the ability to independently vary the momentum ($\mathbf{q} = \mathbf{k} - \mathbf{k}'$) and energy (ν) transferred to the target makes it possible to map the target response as a function of its excitation energy, with a spatial resolution that can be adjusted to the physical processes being studied. This spatial resolution is determined by the wavelength of the exchanged virtual photon :

$\lambda \approx \frac{1}{|\mathbf{q}|}$, where \mathbf{q} is the 3-momentum of the virtual photon. As can be seen in Figure 1.4, the nuclear response can be studied when Q^2 is less than 0.1 GeV^2 , whereas individual partons comprising the nucleons can be resolved in the high Q^2 region, usually defined as $Q^2 > 1 \text{ GeV}^2$. In the intermediate range there is a transition between the appropriate degrees of freedom describing the scattering, namely from the partonic (quark-gluon) to the meson-nucleon degrees of freedom. The fundamental description of the whole kinematic regime presents a great theoretical challenge, since QCD changes from a perturbative (calculable) to a non-perturbative theory in this transition region. The intuitive picture conveyed by Figure 1.4 can be put on firm grounds by considering the full kinematic dependence of the measured inclusive cross section on the $Q^2 - \nu$ plane, as shown in Figure 1.5. A few important features are worth-noticing: When $Q^2 = 2M_A\nu$, with M_A the nuclear mass, electrons are elastically scattered off the nucleus. The same condition

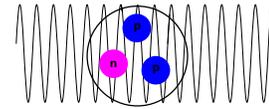
Nuclear (coherent) scattering

$$Q^2 < 0.1 \text{ GeV}^2$$



Transition Region

$$0.1 \text{ GeV}^2 < Q^2 < 1 \text{ GeV}^2$$



Parton (incoherent) scattering

$$Q^2 > 1 \text{ GeV}^2$$

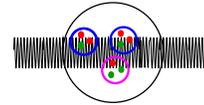


Figure 1.4: Distance scales probed by the virtual photon.

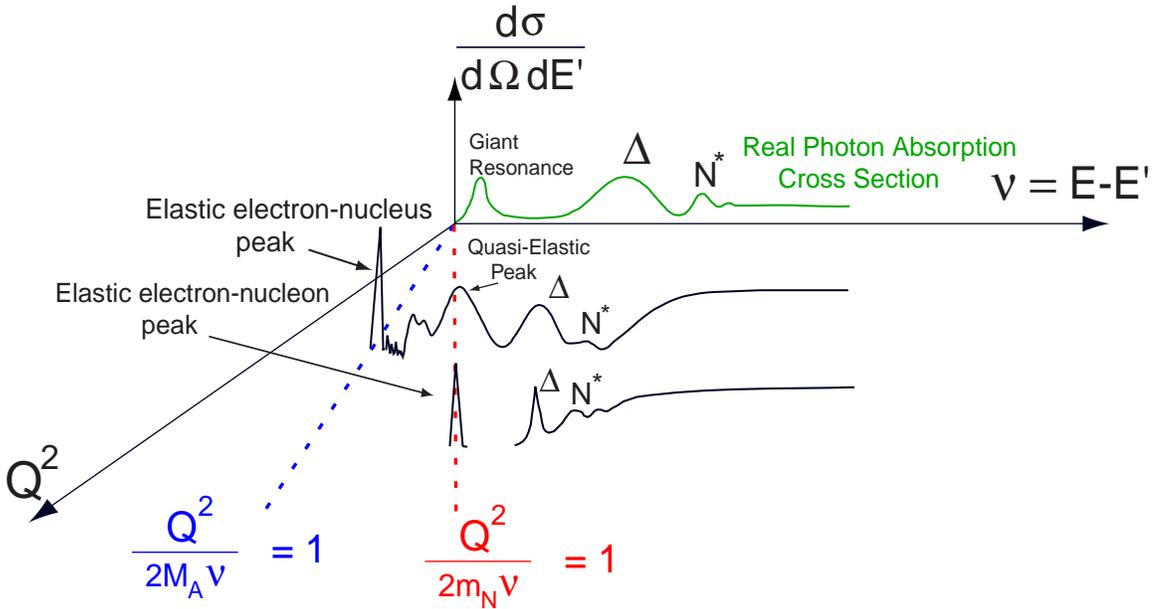


Figure 1.5: Cross section behaviour in the $Q^2 - \nu$ plane.

(with the nuclear mass replaced by the nucleon mass, m_N) holds for elastic scattering off a free nucleon. Due to Fermi motion, the elastic nucleon peak appears as a broadened peak (called the quasielastic peak) when the nucleon is in the nuclear medium. Both nuclear and nucleon elastic scattering are parametrized by the so-called elastic form factors, which are decreasing functions of Q^2 , since it is increasingly difficult for the nucleus (nucleon) to stay intact when the momentum transferred to it is large. At higher excitation energies nucleon resonances, such as the Δ -resonance, start to appear in the excitation spectrum. At even higher momentum transfer and excitation energy the scattering enters the inelastic continuum, dominated by scattering off the point-like nucleon constituents.

This is indeed the path electron scattering research followed historically, after the first electron-nucleus scattering experiment at 20 MeV by Lyman [4] in 1951, which observed deviations from the Mott cross section due to the nuclear charge distribution. The finite proton size became apparent in the pioneering work of Hofstadter [5] in 1955, scattering electrons of energy over 100 MeV off hydrogen. It is interesting to note that elastic electron nucleus (nucleon) scattering, being at the forefront of research during that period, is now used as a calibration method of the experimental apparatus (elastic form factors are known

from world data at a level better than 2%). The extensive investigations of nuclear and nucleon structure [6] (culminating in the Nobel prize award to Hofstadter in 1961) paved the way for the inelastic measurements that followed thereafter. Indeed, the deep inelastic scattering experiments that started at the 20 GeV SLAC accelerator in 1967 [7][9], originally intending to study the electroproduction of resonances as a function of Q^2 [8], finally revealed the nucleon substructure and led to the development of QCD. The discovery of Bjorken scaling, and subsequently of scaling violation, was one of the cornerstone experimental findings that established QCD as a fundamental theory of the strong interactions.

1.2 Polarization Degrees of Freedom

The advent of polarized beams and targets opened a new window in these investigations, namely the access to the spin degrees of freedom. Spin-dependent electron-nucleus scattering experiments can be categorized in two classes: those studying the fundamental problem of the spin-structure of the nucleus (nucleon), and those that use polarization degrees of freedom to extract physical quantities that are difficult or, impossible, to measure in unpolarized scattering. These quantities can be kinematically suppressed nucleon form factors that are difficult to extract from the measured cross sections, or, for example, resonance form factors summed over in the spin averaging performed in unpolarized scattering. The access to spin degrees of freedom greatly enhances the sensitivity of the measurements on these observables.

Experiment	Lab	Year	Target
E80 [11]	SLAC	1983	butanol
E130 [12]	SLAC	1987	butanol
EMC [13]	CERN	1988	ammonia
SMC [14]	CERN	1993	(deuterized) butanol
E142 [15]	SLAC	1993	helium-3
E143 [16]	SLAC	1994	(deuterized) ammonia
E154 [17]	SLAC	1995	helium-3
HERMES [15]	DESY	1996	hydrogen deuterium helium-3
E155 [19]	SLAC	1996	(deuterized) ammonia

Table 1.1: Some of the recent polarized DIS experiments.

A recent example of the second type of experiments is the precise measurement (better than 2%) of the neutron magnetic form factor, G_M^R [10], by measuring the transverse asymmetry A_{TV} in polarized quasielastic ${}^3\text{He}(e,e')$ scattering. The former type of experiments have been an active field of study during the last 17 years, providing a wealth of measurements, mainly in the Deep Inelastic Scattering (DIS) kinematic regime. E80 at SLAC was the first polarized scattering experiment, as shown in Table 1.1 (from [6]). A host of experiments followed in the last 13 years, mainly at high energy machines like SLAC, CERN, and recently HERA at DESY. The EMC experiment observed that the quark spin contribution to the proton spin was only $12 \pm 17\%$. This observation caused the so-called spin-crisis and drew a lot of attention of the subsequent experimental and theoretical effort. The experiments listed in Table 1.1 mapped the nucleon spin structure over a wide kinematic regime (DIS) and provided the data necessary to test fundamental QCD sum rules, such as the Bjorken sum rule. This sum rule relates the difference between the first moment of the proton's and neutron's spin structure function, g_1 , to the neutron's β -decay axial constant.

1.3 Low Q^2 Region

The intuitive picture provided by the Quark Parton Model (QPM) and the fact that the DIS regime was a testing ground of pQCD as a predictive tool were the main reasons that DIS has overwhelmingly been the kinematic regime of study so far (E143 was one of the first DIS experiments to extend its measurements below 1 GeV^2). It was realized, however, that the low Q^2 region ($Q^2 < 1 \text{ GeV}^2$) presents great interest and is of fundamental importance for number of reasons. For instance, relating to the DIS measurements, the contribution of resonant states in the mass region above $W=2 \text{ GeV}$ to the spin sum rules was thought to be important in interpreting the experimental findings, and hence necessitating their independent study [25]. Furthermore, the study of the nucleon's spin structure at low Q^2 is of interest in its own right. New degrees of freedom (for example, gluonic excitations, [25]) are likely to appear at low momentum transfer, revealing a nucleon structure beyond the simple constituent quark model. The non-perturbative nature of the strong interaction at low Q^2 makes theoretical predictions sparse, if not non-existent.

Of equal importance is the existence of testable sum-rules, derived on very general theoretical grounds.

1.3.1 The Gerasimov-Drell-Hearn (GDH) Sum Rule

The GDH sum rule, derived by Gerasimov, Drell and Hearn in 1966, applies at $Q^2 = 0$. It relates the difference in the total photoabsorption cross section on nucleons for photon-nucleon helicity $1/2$ and $3/2$ to the anomalous magnetic moment of the target nucleon.

1.4 Connection between the GDH and the Bjorken Sum Rules

Both of the aforementioned sum rules relate properties of the nucleon's ground state with integrals of the nucleon's spin structure functions, which are experimentally accessible. Thus global properties of nucleon structure theory can be tested, as has been extensively done in case of the Bjorken sum rule, and recently for the GDH sum rule (for the proton).

The connection between these two limits, that is, the generalization of these sum rules for intermediate Q^2 has been an active effort in recent years. As will be detailed in the following chapter, both the Bjorken and the GDH integrals can be shown to be limiting cases of one integral involving the nucleon's spin structure functions. Using twist expansions, the Bjorken sum rule can be evolved to Q^2 values as low as 0.5 GeV^2 . Chiral perturbation theory is applicable in the other extreme, and is believed to be able to evolve the GDH sum rule to a squared momentum transfer as high as $Q^2 = 0.2 \text{ GeV}^2$. These efforts attempt for the first time to describe hadronic structure by fundamental theory over the whole kinematic range, from the long to the short distances.

1.5 The Significance of Neutron Spin Structure

Since neutron targets do not exist and proton targets are experimentally well established, the question arises whether proton measurements alone are adequate to provide the data to support the aforementioned investigations, or if the experimental investigation of the neutron's structure is worthwhile. The answer to the latter question is yes, and there are a few important reasons, besides the mere interest to study the structure of both fundamental building blocks of matter.

1.5.1 DIS Limit

The Bjorken sum rule relates the difference between the proton and the neutron integrals of the structure function g_1 . Its strength relies on its model independence (as opposed to the violated Ellis-Jaffe sum rule), since the singlet contribution (as well as a_8 , see Section 2.2.2) disappears in the difference.

1.5.2 Low Q^2 Limit

If chiral perturbation theory is applied to evolve the GDH sum rule (for either the proton or the neutron) at low Q^2 , it is found that [26][27] whereas the leading order term is independent of Q^2 , the next-to-leading order (NLO) term has a strong Q^2 dependence. This limits the maximum value of Q^2 up to which the perturbative expansion is meaningful. Contrary to the individual terms, the difference between the proton and the neutron integrals yields a much reduced Q^2 dependence of the NLO term, thus extending the applicability of the theory. This is attributed to the fact that the $\Delta(1232)$ contribution, which dominates the individual terms, largely cancels in the difference.

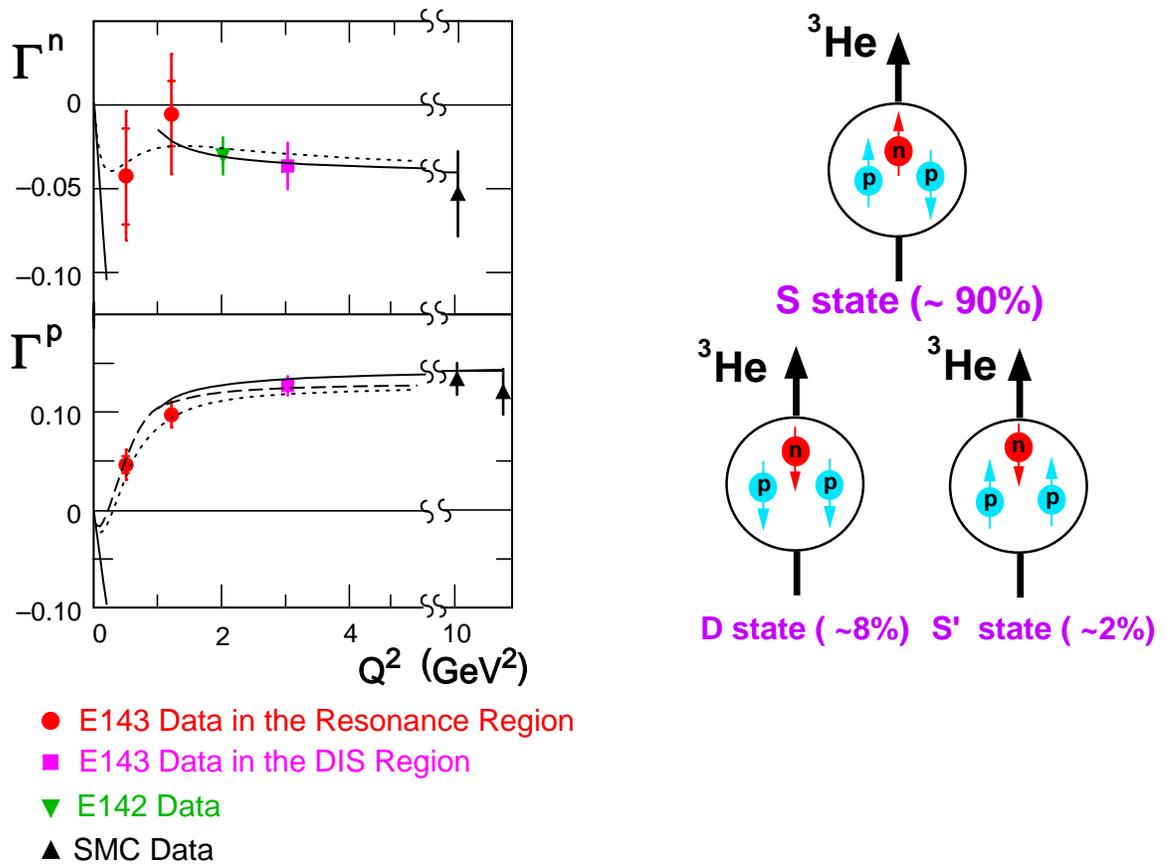
1.5.3 Theoretical Inconsistencies with the Neutron

More important, there has been evidence, that there are inconsistencies when applying theoretical predictions to the neutron, that do not show up for the proton. Early phenomenological models based on the relativistic quark model and fitting a set of resonances [22][24] or on analysis of pion photoproduction data [23] agree with the GDH prediction for the proton but not for the neutron.

1.6 ^3He as an effective neutron target

The study of the neutron spin structure at low Q^2 is thus not only physically interesting, but tied together with the progress of the nucleon structure program as a whole. Since there are no free neutrons, one has to revert to either deuterium or ^3He targets. Deuterium is a spin-1 nucleus, therefore the proton and the neutron have their spins aligned, parallel to the deuterium spin. Thus these targets have the disadvantage that the proton contribution to the polarized cross sections has to be subtracted using known proton data. This has the

result of amplifying the error of the extracted neutron structure functions. Figure 1.6(a) shows the first moments of g_1 , $\Gamma^{p(n)} = \int_0^1 g_1(x) dx$, for the proton and neutron measured by the E143 experiment at SLAC. The neutron data is extracted from deuterium data. On the other hand, ${}^3\text{He}$ is almost an ideal neutron target. As illustrated in Figure 1.6(b), apart from small admixtures of a D and an S' state, the ${}^3\text{He}$ nucleus is predominantly in an S state. The two protons have their spins antialigned, leaving the neutron as a carrier of the ${}^3\text{He}$ spin. Hence ${}^3\text{He}$ does not suffer from the same disadvantage as deuterium. However, as will be described in Chapter 5, the extraction of neutron quantities from measured ${}^3\text{He}$ data is not as straightforward in the resonance region as it is in the DIS region.



(a)

(b)

Figure 1.6: (a) E143 data on proton and neutron in the resonance and DIS region, along with DIS SMC and E142 data. (b) ${}^3\text{He}$ wavefunction, from [21].

1.7 Experiment E-94010

Experiment E-94010 provides for the first time neutron spin structure data at low Q^2 and is the first measurement of the Q^2 -evolution of the GDH sum rule. E-94010 successfully took data in the period between September 25th and December 24th 1998, in the Experimental Hall A of Thomas Jefferson National Accelerator Facility (TJNAF) in Newport News, Virginia.

The experiment measured inclusive polarized cross sections by scattering polarized electrons off a polarized ^3He target. It was the first experiment to use a polarized ^3He target at TJNAF. The target length was 40 cm and the density of ^3He nuclei was about $3 \times 10^{20} \text{ cm}^{-3}$. The target maintained a polarization of about 35% at beam currents as high as $15 \mu\text{A}$. The average luminosity was thus about $10^{36} \text{ cm}^{-2}\text{s}^{-1}$ and each target cell saw about 10 C of charge from the beam. Six different target cells were used.

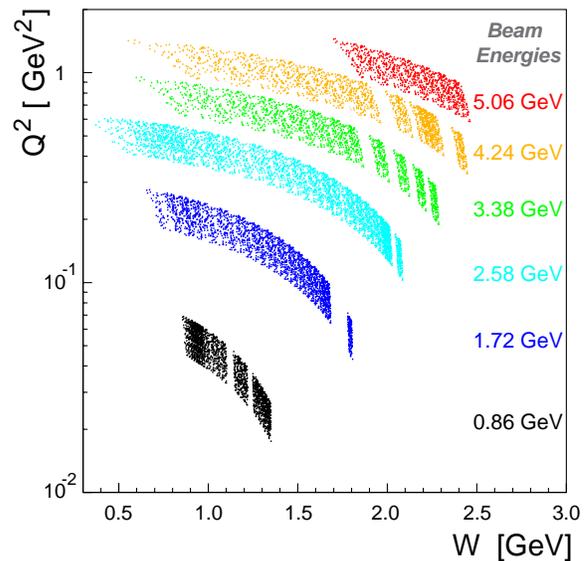


Figure 1.7: E-94010 kinematic coverage.

Kinematic Coverage

As shown in Figure 1.7, by using six different beam energies and a fixed scattering angle of 15.5° , the range of squared momentum transfer and invariant mass covered was $0.02 \text{ GeV}^2 < Q^2 < 1 \text{ GeV}^2$ and $0.5 \text{ GeV} < W < 2.5 \text{ GeV}$, respectively. The electron beam was in use for over 1000 hours, resulting in about 2300 runs totaling about 5 Terabytes of recorded data. This experiment was the first to utilize a strained GaAs cathode in the polarized electron gun, which provided beam with a polarization of about 70% and excellent availability.

Structure of the Thesis

The following chapter sets the theoretical foundations of the physical observables extracted from the measured data, which are presented in Chapter 5. The experimental apparatus (besides the ^3He target) used for the measurement is described in Chapter 3. Because of the author's intimate involvement in the preparation, operation and related data analysis of the ^3He Target, Chapter 4 is entirely devoted to its description.

Bibliography

- [1] G.B. West, Phys. Rep. **18**, 263 (1975)
- [2] L.S. Cardman, Nucl. Phys. A654, 73 (1999)
- [3] F. Gross, JLAB Publication CEBAF-85-003, 1985
- [4] E.M. Lyman, A.O. Hanson and M.B. Scott, Phys. Rev. **84**, 626 (1951)
- [5] R. Hofstadter and R.W. McAllister, Phys. Rev **98**, 217 (1955)
- [6] R. Hofstadter, Rev. Mod. Phys. **28**, 214 (1956)
- [7] R.E. Taylor, Rev. Mod. Phys., **63**, 573 (1991)
- [8] J.I. Friedman, Rev. Mod. Phys., **63**, 615 (1991)
- [9] H.W. Kendall, Rev. Mod. Phys., **63**, 597 (1991)
- [10] W. Xu *et al*, Phys. Rev. Letters **85**, 2900 (2000)
- [11] G. Baum *et al*, Phys. Rev. Lett **45**, 2000 (1980)
- [12] G. Baum *et al*, Phys. Rev. Lett **51**, 1135 (1983)
- [13] J. Ashman *et al* Phys. Lett. B206, 364 (1988)
- [14] D. Adams *et al*, Phys. Lett. B357, 248 (1995)
- [15] P.L. Anthony *et al*, Phys. Rev. Lett. **71**, 959 (1993)
- [16] K. Abe *et al*, Phys. Rev. Lett. **74**, 346 (1995)
- [17] K. Abe *et al*, Phys. Rev. Lett. **79**, 26 (1997)
- [18] A. Airapetian *et al*, Phys. Lett. B442, 484 (1998)

- [19] P.L. Anthony *et al*, Phys. Lett. B458, 529 (1999)
- [20] C.Y. Prescott, International School of Nucleon Structure, Ed. B. Frois, V.W. Hughes and N. De Groot, World Scientific, Singapore, 1997
- [21] R.W. Schulze and P.U. Sauer, Phys. Rev. C **38**, 38 (1993)
- [22] V.D. Burkert *et al*, JLAB Publication CEBAF-PR-91-023, 1991
- [23] I. Karliner, Phys. Rev. D **7**, 2717 (1973)
- [24] D. Drechsel, Prog. Part. Nucl. Phys., **34**, 181 (1995)
- [25] V.D. Burkert, JLAB Publication CEBAF-PR-94-001, 1994
- [26] V.D. Burkert, nucl-th/0005033
- [27] V.D. Burkert, JLAB Publication JLAB-PHY-00-33, 2000

Theoretical Foundation of Experimental Observables

2.1 Polarized Electron Scattering

The Feynman diagram describing electron-nucleon scattering in the one-photon exchange approximation is shown in Figure 2.1. The four momenta of the incoming and scattered electron are $k = (E, \mathbf{k})$ and $k' = (E', \mathbf{k}')$ respectively. For a nucleon at rest the four momentum is $P = (M, 0)$.

The scattering cross section for this process is [1]

$$\frac{d^2\sigma}{d\Omega dE'} = \frac{\alpha^2}{2MQ^4} \frac{E'}{E} L_{\mu\nu} W^{\mu\nu} \quad (2.1)$$

where $L_{\mu\nu}$ and $W^{\mu\nu}$ are the leptonic and hadronic tensors, respectively. The leptonic tensor is

$$L_{\mu\nu} = [\bar{u}(k', s') \gamma_\mu u(k, s)]^* [\bar{u}(k', s') \gamma_\nu u(k, s)] \quad (2.2)$$

The leptonic tensor can be written as a sum of symmetric and antisymmetric parts, which, summing over the unobserved scattered electron spin, s' , read

$$L_{\mu\nu} = L_{\mu\nu}^{(S)}(k; k') + iL_{\mu\nu}^{(A)}(k, s; k') \quad (2.3)$$

with

$$L_{\mu\nu}^{(S)}(k; k') = k_\mu k'_\nu + k'_\mu k_\nu - g_{\mu\nu}(k \cdot k' - m^2) \quad (2.4)$$

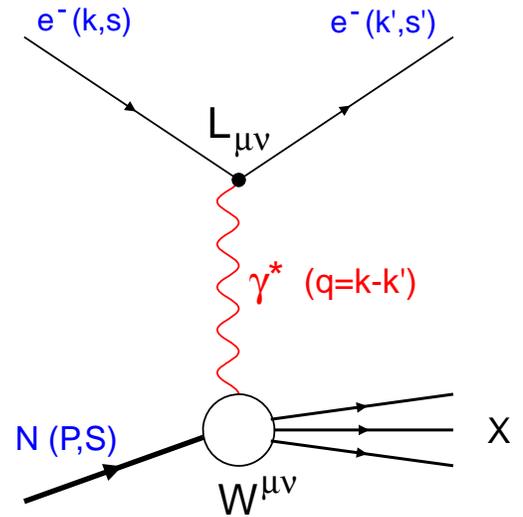


Figure 2.1: Feynman diagram for the process $N(e, e')X$.

$$L_{\mu\nu}^{(A)}(k, s; k') = m\epsilon_{\mu\nu\alpha\beta}s^\alpha(k - k')^\beta \quad (2.5)$$

The hadronic tensor [2],

$$W_{\mu\nu} = \frac{1}{2} \sum_X (2\pi)^3 \delta^4(P + q - p_X) \langle N | J_\mu(0) | X \rangle \langle X | J_\nu(0) | N \rangle \quad (2.6)$$

contains all the information on the structure of the target and the coupling of the target current, J_μ , to the virtual photon, γ^* . The target-nucleon ground state is $|N\rangle$. For exclusive scattering $|X\rangle$ denotes a specific hadronic final state, while for inclusive scattering one has to sum over all final states X. Similarly to the leptonic tensor, $W_{\mu\nu}$ can be decomposed into a symmetric and an antisymmetric part :

$$W_{\mu\nu}(q; P, S) = W_{\mu\nu}^{(S)}(q; P) + iW_{\mu\nu}^{(A)}(q; P, S) \quad (2.7)$$

The most general forms of $W_{\mu\nu}^{(S)}$ and $W_{\mu\nu}^{(A)}$ constrained by Lorentz and gauge invariance, as well as invariance under time reversal and parity, are :

$$W_{\mu\nu}^{(S)}(q; P) = (-g_{\mu\nu} + \frac{q_\mu q_\nu}{q^2})F_1 + \frac{1}{P \cdot q} [(P_\mu - \frac{P \cdot q}{q^2} q_\mu)(P_\nu - \frac{P \cdot q}{q^2} q_\nu)]F_2 \quad (2.8)$$

$$W_{\mu\nu}^{(A)}(q; P, S) = \frac{1}{P \cdot q} \epsilon_{\mu\nu\alpha\beta} q^\alpha S^\beta g_1 + \frac{1}{(P \cdot q)^2} [(P \cdot q)S^\beta - (S \cdot q)P^\beta]g_2 \quad (2.9)$$

where F_1, F_2 are the unpolarized structure functions whereas g_1, g_2 are the spin structure functions. All four structure functions depend on two invariants, usually chosen to be either Q^2 and $x = Q^2/2P \cdot q$, or Q^2 and W , the invariant mass of the hadronic final state. In the laboratory frame $x = Q^2/2M\nu$, where $\nu = E - E'$ is the electron energy loss.

2.2 DIS Limit : Parton Model and Sum Rules

2.2.1 Parton Model

The physical interpretation of the spin structure function g_1 is most straightforward in the Deep Inelastic Scattering (DIS) limit, defined by $Q^2, \nu \rightarrow \infty$, with x finite. In this limit the Quark Parton Model (QPM), employing the impulse approximation, is a very plausible description of the $\gamma^* - N$ scattering. As first suggested by Feynman, if one views the nucleon from an infinite momentum frame, the partons making it up will each share a finite fraction $0 < x_i < 1$ of the nucleon's momentum, $P \rightarrow \infty$, and will move closely parallel to P . Due to asymptotic freedom they behave almost like free and $\gamma^* - N$ scattering can be treated as an

incoherent sum (see Figure 2.2) of γ^* -parton scattering [5]. In this limit the structure functions scale, i.e. depend only on the Bjorken variable x , and not on Q^2 . If $q_f^+(x)$ ($q_f^-(x)$) is the momentum-fraction distribution of quarks and anti-quarks of flavor f with their spins in the same (opposite) direction as the nucleon spin, then [6]

$$F_1(x) = \frac{1}{2} \sum_f e_f^2 [q_f^+(x) + q_f^-(x)] \equiv \frac{1}{2} \sum_f e_f^2 q_f(x) \quad (2.10)$$

and

$$g_1(x) = \frac{1}{2} \sum_f e_f^2 [q_f^+(x) - q_f^-(x)] \equiv \frac{1}{2} \sum_f e_f^2 \Delta q_f(x) \quad (2.11)$$

where e_f is the charge of quark-flavor f in units of the electron charge.

Thus F_1 and g_1 represent the momentum and spin distribution of the quarks in the nucleon, respectively. In the parton model, $F_2 = 2xF_1$ and $g_2=0$.

2.2.2 Sum Rules

Various sum rules have been derived in order to test fundamental properties of the strong interactions. Based on fairly general assumptions, they relate moments of the spin structure functions to ground state nucleon properties. From (2.11) it follows, by taking into account only the light u,d and s quarks, that the first moment of $g_1(x)$ can be written as

$$\Gamma_1^p \equiv \int_0^1 g_1^p(x) dx = \frac{1}{2} \left(\frac{4}{9} \Delta u + \frac{1}{9} \Delta d + \frac{1}{9} \Delta s \right) \quad (2.12)$$

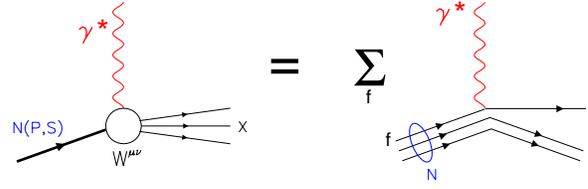


Figure 2.2: Photon-Nucleon Scattering in the Quark Parton Model.

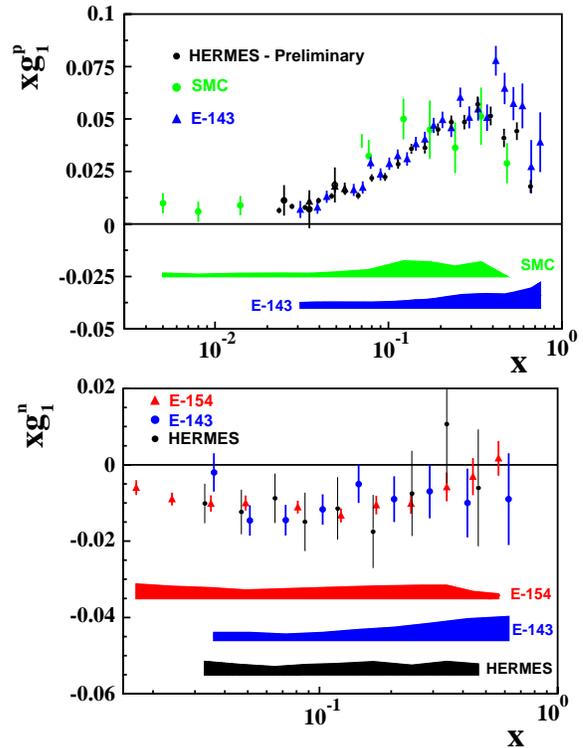


Figure 2.3: Existing $g_1^{(p)}(x)$ and $g_1^{(n)}(x)$ data.

$$\Gamma_1^n \equiv \int_0^1 g_1^n(x) dx = \frac{1}{2} \left(\frac{1}{9} \Delta u + \frac{4}{9} \Delta d + \frac{1}{9} \Delta s \right) \quad (2.13)$$

for the proton and neutron, respectively, with $\Delta q_f \equiv \int_0^1 \Delta q_f(x) dx$. A fundamental sum rule, first derived by Bjorken [7], concerns the difference $\Gamma_1^p - \Gamma_1^n$:

$$\Gamma_1^p - \Gamma_1^n = \frac{1}{6} (\Delta u - \Delta d) = \frac{1}{6} \frac{g_A}{g_V} \quad (2.14)$$

where g_A and g_V are the axial and vector coupling constants appearing in neutron β -decay. The reason that the nucleon weak couplings appear in the sum rule is that weak decays, as well as polarized DIS, probe the nucleon with an axial current of the form $\langle N', s' | \bar{q}_j \gamma^\mu \gamma_5 q_i | N, s \rangle$, where N and N' stand for the initial and final state nucleon, s and s' for the nucleon's polarization, and q_i and q_j for the quark fields of quark species i and j , respectively [8]. Assuming SU(3) flavor symmetry, or in the case of neutron decay only isospin symmetry, all these matrix elements can be related to

$$2M \Delta q_i s^\mu = \langle p, s | \bar{q}_i \gamma^\mu \gamma_5 q_i | p, s \rangle \quad (2.15)$$

with M the proton mass and $|p, s\rangle$ the proton state with polarization s^μ .

There are three diagonal combinations of these matrix elements. Two correspond to the generators of $SU(3)_f$ (non-singlet), namely $a_3 = \frac{g_A}{g_V} = \Delta u - \Delta d$ and $a_8 = \Delta u + \Delta d - 2\Delta s$. The third is the singlet combination $a_0 = \Delta \Sigma = \Delta u + \Delta d + \Delta s$. Thus the first moment of g_1 can be written as

$$\Gamma_1^{p(n)} = \pm \frac{1}{12} a_3 + \frac{1}{36} a_8 + \frac{1}{9} a_0 \quad (2.16)$$

where the $+$ ($-$) sign corresponds to the proton (neutron). Taking the difference, the Bjorken sum rule 2.14 follows. The foregoing is valid at the limit $Q^2 \rightarrow \infty$.

At large, but finite Q^2 , QCD radiative corrections have to be taken into account, as for example the graphs shown in Figure 2.4. The singlet and non-singlet matrix elements are each multiplied by a factor, C_S and C_{NS} , respectively. Up to first order in α_s , these factors are [9]:

$$C_{NS}(Q^2) = 1 - \frac{\alpha_s(Q^2)}{\pi} + \dots \quad (2.17)$$

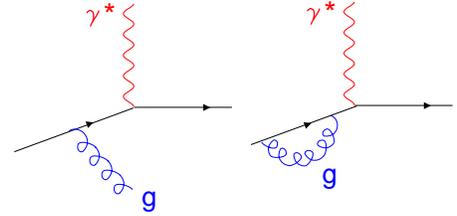


Figure 2.4: Gluon radiation and gluon emission-reabsorption graphs contributing to the corrections of Bjorken sum rule.

and

$$C_S(Q^2) = 1 - \frac{\alpha_s(Q^2)}{3\pi} + \dots \quad (2.18)$$

Thus the Bjorken sum rule reads:

$$\Gamma_1^p - \Gamma_1^n = \frac{1}{6}(\Delta u - \Delta d) = \frac{1}{6} \frac{g_A}{g_V} \left(1 - \frac{\alpha_s(Q^2)}{\pi} + \dots\right) \quad (2.19)$$

While the Bjorken sum rule assumes isospin symmetry only, another sum rule known as Ellis-Jaffe sum rule, predicted the individual moments Γ_1^p and Γ_1^n , assuming $SU(3)_f$ symmetry and neglecting the strange quark spin contribution to the nucleon spin, that is, $\Delta s = 0$. Using (2.16),(2.17),(2.18) and $a_0 = a_8$, it follows that :

$$\Gamma_1^{p,n}(Q^2) = \left(1 - \frac{\alpha_s(Q^2)}{\pi} + \dots\right) \left(\pm \frac{a_3}{12} + \frac{a_8}{36}\right) + \left(1 - \frac{\alpha_s(Q^2)}{3\pi} + \dots\right) \frac{a_8}{9} \quad (2.20)$$

Figure 2.5 shows the experimental verification of the Bjorken sum rule (1σ) and the disagreement between the data and the predictions of the Ellis-Jaffe sum rule (3σ).

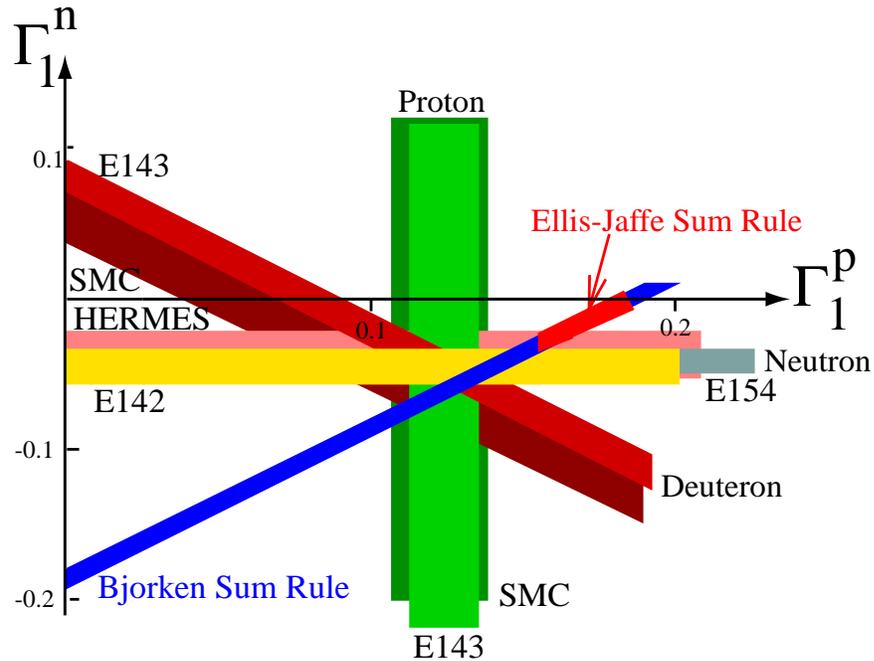


Figure 2.5: Plot of Γ_1^p and Γ_1^n , with the predictions of Bjorken and Ellis-Jaffe sum rules superimposed on the existing data, from [6].

2.3 $Q^2 = 0$ Limit : Gerasimov-Drell-Hearn Sum Rule

The GDH Sum Rule relates the anomalous magnetic moment of a nucleon (in fact any particle) to the integrated difference of photoabsorption cross-sections with photon and nucleon spin parallel or antiparallel. The sum rule is based on very general principles, and only one assumption, namely the high energy behavior of a Compton scattering amplitude. In 1954 Gell-Mann and Goldberger [10] and independently Low [11] showed that, up to terms linear in the photon energy ν , the amplitude for forward Compton scattering (Figure 2.6) off a spin-1/2 particle interacting with arbitrary local and renormalizable fields is

$$\mathcal{M} = -\frac{\alpha}{M} \mathbf{e}'^* \cdot \mathbf{e} - i\nu \frac{\alpha}{2M^2} \kappa_A^2 \boldsymbol{\sigma} \cdot (\mathbf{e}'^* \times \mathbf{e}) \quad (2.21)$$

where M and κ_A are the mass and anomalous magnetic moment of the nucleon, respectively, i.e. $\mu_{nucleon} = (1 + \kappa_A)\mu_N$, and $\mu_N = \frac{e\hbar}{2M_P}$ is the nucleon magneton, that is, the magnetic moment the nucleon would have were it a point particle. Their derivation was based on Lorentz and gauge invariance principles. On the other hand, it can be shown on general grounds [17] that

$$\mathcal{M} = \chi^\dagger [f_1(\nu) \mathbf{e}'^* \cdot \mathbf{e} + i\nu f_2(\nu) \boldsymbol{\sigma} \cdot (\mathbf{e}'^* \times \mathbf{e})] \chi \quad (2.22)$$

with \mathbf{e} the photon polarization vector. For photon and nucleon spins parallel or antiparallel, the respective amplitudes are

$$\mathcal{M}_{1/2} = f_1(\nu) + \nu f_2(\nu) \quad (2.23)$$

$$\mathcal{M}_{3/2} = f_1(\nu) - \nu f_2(\nu) \quad (2.24)$$

Based on the optical theorem (unitarity), the photoabsorption cross sections σ_i ($i=1/2, 3/2$) can be related to the imaginary part of the forward Compton scattering amplitude:

$$\sigma(\nu)_i = \frac{4\pi}{\nu} \text{Im}\{\mathcal{M}_i(\nu)\}. \quad (2.25)$$

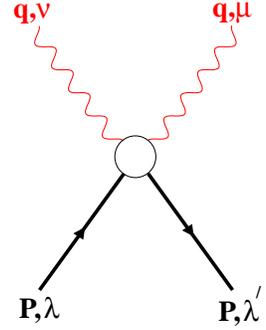


Figure 2.6: Feynman diagram for forward Compton scattering.

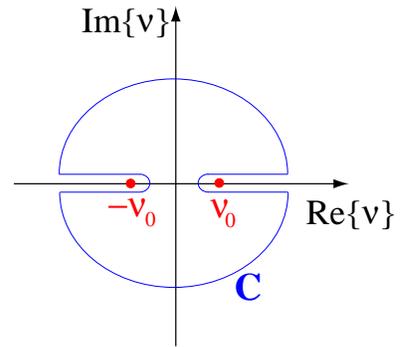


Figure 2.7: Complex ν plane.

Thus

$$\text{Im}\{f_1(\nu)\} = \frac{\nu}{8\pi}(\sigma_{1/2}(\nu) + \sigma_{3/2}(\nu)), \quad (2.26)$$

$$\text{Im}\{f_2(\nu)\} = \frac{1}{8\pi}(\sigma_{1/2}(\nu) - \sigma_{3/2}(\nu)). \quad (2.27)$$

Due to the equivalence of causality and analyticity [12], f_1 and f_2 can be analytically continued in the upper half complex ν plane. Applying Cauchy's Theorem for $f_2(\nu)$ on the contour C shown in Figure 2.7,

$$f_2(\nu) = \frac{1}{2\pi i} \oint_C \frac{d\nu'}{\nu' - \nu} f_2(\nu') \quad (2.28)$$

and using the no-subtraction hypothesis, that is assuming that $|f_2(\nu)| \rightarrow 0$, for $|\nu| \rightarrow \infty$, it follows that

$$f_2(\nu) = \frac{1}{\pi} \int_{\nu_0}^{\infty} d\nu' \frac{\nu'}{\nu'^2 - \nu^2} \text{Im}\{f_2(\nu')\} \quad (2.29)$$

ν_0 is the inelastic threshold [13] given by

$$\nu_0 = m_\pi + \frac{m_\pi^2}{2M} \approx 145 \text{ MeV} \quad (2.30)$$

Setting $\nu=0$ in (2.29) and using the low energy relation (2.21), it follows that

$$I_{GDH} \equiv \int_{\nu_0}^{\infty} \frac{d\nu}{\nu} [\sigma_{1/2}(\nu) - \sigma_{3/2}(\nu)] = -\frac{2\pi^2\alpha}{M^2} \kappa_A^2 \quad (2.31)$$

which is the GDH Sum Rule, first derived by Drell and

Hearn [15] and independently by Gerasimov [16].

For the proton, neutron and ^3He the GDH prediction is $I_{GDH}^p = -204 \mu\text{barn}$, $I_{GDH}^n = -233 \mu\text{barn}$ and $I_{GDH}^{^3\text{He}} = -496 \mu\text{barn}$, respectively. Figure 2.8 shows the data obtained recently [18] with the tagged polarized photon beam at the MAMI microtron in Mainz. Apart from the energy denominator, the data shown is the integrand of the GDH integral for the proton. The energy range accessible by the experiment was 200-800 MeV. In this range the GDH integral is found to be $-218 \pm 6 \mu\text{barn}$. By adding the estimates for the two other regions (threshold up to 200 MeV, and higher than 800 MeV) it follows [25] that the total result for the proton is $-202 \pm 10 \mu\text{barn}$.

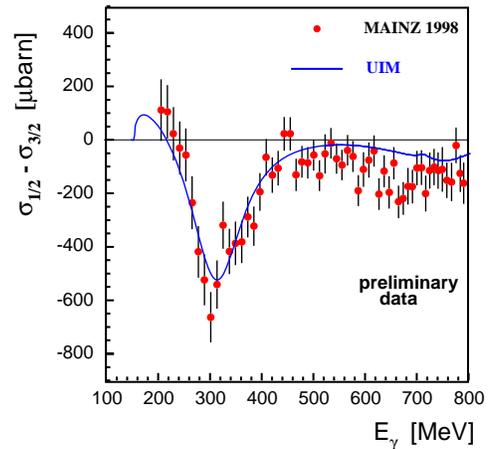


Figure 2.8: Mainz data on polarized photoabsorption cross sections for the proton, with UIM prediction [27].

2.3.1 Forward Compton Scattering Amplitudes

Consider virtual forward compton scattering in the nucleon rest-frame. The initial(final) helicities of the photon and nucleon are $h, \lambda(h', \lambda')$ respectively. The amplitude for this process is [3]

$$(T_{\mu\nu})_{\lambda'\lambda} = i \int d^4x e^{iq \cdot x} \langle p, \lambda' | T j_\mu(x) j_\nu(0) | p, \lambda \rangle. \quad (2.32)$$

From symmetry arguments, $T_{\mu\nu}$ has the same structure as $W_{\mu\nu}$, namely

$$T_{\mu\nu} = T_{\mu\nu}^{(S)} + iT_{\mu\nu}^{(A)} \quad (2.33)$$

with

$$T_{\mu\nu}^{(S)} = \tilde{F}_1 \left(-g_{\mu\nu} + \frac{q_\mu q_\nu}{q^2} \right) + \frac{\tilde{F}_2}{(p \cdot q)} \left[(P_\mu - \frac{P \cdot q}{q^2} q_\mu) (P_\nu - \frac{P \cdot q}{q^2} q_\nu) \right] \quad (2.34)$$

and

$$T_{\mu\nu}^{(A)} = \epsilon_{\mu\nu\alpha\beta} q^\alpha \left[\frac{\tilde{g}_1}{(p \cdot q)} + \frac{\tilde{g}_2}{(p \cdot q)^2} [(P \cdot q) S^\beta - (S \cdot q) P^\beta] \right]. \quad (2.35)$$

Note that Ji and Osborne [23] use S_1 and S_2 to denote \tilde{g}_1 and \tilde{g}_2 , which is the notation followed by Manohar [3]. The latter has been adopted here to avoid confusion with the nucleon spin vector S .

The hadron structure functions F_1 , F_2 , g_1 and g_2 are given by the discontinuity of \tilde{F}_1 , \tilde{F}_2 , \tilde{g}_1 and \tilde{g}_2 across the real ν -axis, respectively. For example,

$$g_1(\omega) = \frac{1}{2\pi} \text{Im} \{ \tilde{g}_1(\omega + i\epsilon) \}, \text{ etc} \quad (2.36)$$

This is a direct implication of the optical theorem, that is, the forward scattering amplitude is proportional to the total cross section. Thus a measurable physical quantity (nucleon structure function) can be related to a (calculable, in principle) amplitude. A generalization of the GDH Sum Rule at non-zero values of Q^2 rests on this connection, as will be described in more detail in Section 2.4.3 .

Consider z to be the angular momentum quantization axis, and the direction of the virtual photon. Then $q^\mu = (q^0, 0, 0, q^3)$ and the three polarization vectors of the photon are

$$\epsilon_+^\mu = -\frac{1}{\sqrt{2}}(0, 1, i, 0) \quad h = 1 \quad (2.37)$$

$$\epsilon_-^\mu = \frac{1}{\sqrt{2}}(0, 1, -i, 0) \quad h = -1 \quad (2.38)$$

$$\epsilon_0^\mu = \frac{1}{Q}(q^3, 0, 0, q^0) \quad h = 0 \quad (2.39)$$

The helicity amplitudes $\mathcal{M}(h, \lambda; h', \lambda')$ are given by

$$\mathcal{M}(h, \lambda; h', \lambda') = \epsilon_h^{*\mu} \epsilon_h^\nu T_{\mu\nu} \quad (2.40)$$

For a spin- J target particle there are $2J+3$ independent helicity amplitudes. By denoting $\lambda=1/2$ ($-1/2$) by \uparrow (\downarrow) the four helicity amplitudes describing forward photon-nucleon scattering are $\mathcal{M}_{+, \uparrow; +, \uparrow}$, $\mathcal{M}_{+, \downarrow; +, \downarrow}$, $\mathcal{M}_{0, \uparrow; 0, \uparrow}$ and $\mathcal{M}_{+, \downarrow; 0, \uparrow}$. The virtual photoabsorption cross section is given by

$$\sigma = \frac{4\pi^2\alpha}{KM} \text{Im}\{\mathcal{M}\} \quad (2.41)$$

where K is the virtual photon flux. For real photons $K=\nu$, the laboratory photon energy required to produce a final state X of invariant mass W , with $W^2 = M^2 + 2MK$. For virtual photons ($Q^2 \neq 0$) K is ill-defined. The usual convention, due to Hand [19], is that K satisfies the same relation, namely

$$K = \frac{W^2 - M^2}{2M} = \nu - \frac{Q^2}{2M} \quad (2.42)$$

Using (2.34), (2.35), (2.40), (2.41) and (2.36) it can be found that

$$\sigma_{\frac{3}{2}}^T \equiv \frac{4\pi^2\alpha}{KM} \text{Im}\{\mathcal{M}_{+, \uparrow; +, \uparrow}\} = \frac{4\pi^2\alpha}{KM} [F_1 - g_1 + \frac{2Mx}{\nu} g_2] \quad (2.43)$$

$$\sigma_{\frac{1}{2}}^T \equiv \frac{4\pi^2\alpha}{KM} \text{Im}\{\mathcal{M}_{+, \downarrow; +, \downarrow}\} = \frac{4\pi^2\alpha}{KM} [F_1 + g_1 - \frac{2Mx}{\nu} g_2] \quad (2.44)$$

$$\sigma_{\frac{1}{2}}^L \equiv \frac{4\pi^2\alpha}{KM} \text{Im}\{\mathcal{M}_{0, \uparrow; 0, \uparrow}\} = \frac{4\pi^2\alpha}{KM} [-F_1 + F_2(\frac{M}{\nu} + \frac{1}{2x})] \quad (2.45)$$

$$\sigma'_{LT} \equiv \frac{4\pi^2\alpha}{KM} \text{Im}\{\mathcal{M}_{+, \downarrow; 0, \uparrow}\} = \frac{4\pi^2\alpha}{K} \gamma(g_1 + g_2) \quad (2.46)$$

where $\gamma = \frac{Q^2}{\nu}$.

By defining σ'_{TT} as

$$\sigma'_{TT} = \frac{1}{2}(\sigma_{\frac{1}{2}}^T - \sigma_{\frac{3}{2}}^T) \quad (2.47)$$

it follows from (2.43) and (2.44) that

$$\sigma'_{TT} = \frac{4\pi^2\alpha}{KM} (g_1 - \gamma^2 g_2) \quad (2.48)$$

The GDH sum rule can be rewritten in terms of $\sigma'_{TT}(Q^2 = 0)$, namely

$$\int_{\nu_0}^{\infty} 2 \frac{d\nu}{\nu} \sigma'_{TT} = -\frac{2\pi^2\alpha}{M^2} \kappa_A^2 \quad (2.49)$$

2.4 Bridging the gap between $Q^2 = 0$ and $Q^2 = \infty$

2.4.1 Operator Product Expansion and Higher Twists: Bridging the gap from above

QCD provides a tool for the starting point of calculating the forward Compton scattering amplitude 2.32, namely the Operator Product Expansion (OPE). In the limit $d \rightarrow 0$, the product of two local operators, $\mathcal{O}_\alpha(d)\mathcal{O}_\beta(0)$, can be written as [3]

$$\lim_{x \rightarrow 0} \mathcal{O}_\alpha(d)\mathcal{O}_\beta(0) = \sum_k c_{\alpha\beta k}(d)\mathcal{O}_k(0) \quad (2.50)$$

The coefficient functions $c_{abk}(d)$ are c-numbers and $\mathcal{O}_k(0)$ are local operators. Both depend on the QCD renormalization scale μ^2 . Physically this expansion represents a separation of long-distance from short-distance effects. The latter are contained in the coefficient functions, which are calculable in perturbative QCD [21][20], whereas the former (non-perturbative) will be represented by the matrix elements of the local operators $\mathcal{O}_k(0)$. These operators are quark and gluon operators of arbitrary spin n and dimension d , written as $\mathcal{O}_{d,n}^{\mu_1 \dots \mu_n}$. The matrix element entering (2.32) is

$$\langle p, s | \mathcal{O}_{d,n}^{\mu_1 \dots \mu_n} | p, s \rangle, \quad (2.51)$$

which is proportional to

$$M^{d-n-2} \mathcal{S}[p^{\mu_1} \dots p^{\mu_n}] \quad (2.52)$$

and to

$$M^{d-n-2} \mathcal{S}[s^{\mu_1} p^{\mu_2} \dots p^{\mu_n}] \quad (2.53)$$

for an axial operator. \mathcal{S} projects out the completely symmetric, traceless component of its tensor argument. It turns out that the contribution of these operators to the forward scattering amplitude is proportional to $(\frac{Q}{M})^{2+n-d} = (\frac{Q}{M})^{2-t}$, where the twist of the operator is defined as $t=d-n$. Table 2.1 summarizes the twist of the quark fields ψ , the gluon field tensor $G_{\mu\nu}$ and the covariant derivative D^μ . Since any gauge invariant operator contains at least two quark fields, or two gluon field tensors, the lowest twist is 2.

	ψ	$G_{\mu\nu}$	D^μ
dimension	3/2	2	1
spin	1/2	1	1
twist	1	1	0

Table 2.1: Dimension, spin and twist of quark field, gluon field tensor and covariant derivative.

Thus in the DIS limit twist-2 operators dominate. As Q^2 is lowered, higher twist operators start to be important. A host of sum rules can be formally derived from OPE. As shown by Jaffe and Ji [20], keeping twist-2 and twist-3 operators only, and using the aforementioned connection between spin structure functions and the Compton amplitude $T_{\mu\nu}$, an infinite set of sum rules on g_1 and g_2 follows:

$$\int_0^1 x^n g_1(x, Q^2) dx = \frac{1}{2} \sum_i a_i^n(\mu^2) F_{2,i}^n(Q^2, \mu^2), \quad n = 0, 2, 4, \dots \quad (2.54)$$

$$\int_0^1 x^n g_2(x, Q^2) dx = -\frac{n}{2(n+1)} \left(\sum_i a_i^n(\mu^2) F_{2,i}^n(Q^2, \mu^2) - \sum_i d_i^n(\mu^2) F_{3,i}^n(Q^2, \mu^2) \right), \quad n = 2, 4, \dots \quad (2.55)$$

where the scalar matrix elements depend on the nucleon structure and the renormalization scale μ^2 at which the operators are defined. $F_{2,i}^n$ and $F_{3,i}^n$ are the c-number coefficient functions. The Bjorken sum rule readily follows from (2.54) by applying it for $n=0$ both for the proton and for the neutron and taking their difference.

2.4.2 Generalized GDH Integral

The GDH integral can be generalized for any value of Q^2 , by introducing the Q^2 -dependent integral

$$I_{GDH}(Q^2) = \frac{2M^2}{Q^2} \int_0^{x_0} g_1(x, Q^2) dx \rightarrow \begin{cases} -\frac{1}{2}\kappa_A^2 & \text{for } Q^2 \rightarrow 0 \\ \frac{2M^2}{Q^2}\Gamma_1 + \mathcal{O}(Q^{-4}) & \text{for } Q^2 \rightarrow \infty \end{cases}, \quad (2.56)$$

where

$$x_0 = Q^2 / (2Mm_\pi + m_\pi^2 + Q^2) \quad (2.57)$$

refers to the inelastic threshold of one-pion production and Γ_1 is the previously defined first moment of $g_1(x)$, $\Gamma_1 = \int_0^1 g_1(x) dx$. The $Q^2 \rightarrow 0$ limit of I_{GDH} follows from (2.48) and (2.49). Because the upper limit of integration in (2.56) is smaller than 1 at any finite Q^2 , there is no elastic contribution to the integral.

2.4.3 Bridging the gap from below: Chiral Perturbation Theory

In 1989 Anselmino et al [22] used the strong Q^2 dependence of the generalized GDH integral (but with an upper integration limit of 1) as an argument that would possibly resolve the spin crisis. They attributed the discrepancy between the EMC extraction of $\Delta\Sigma$ at

$Q^2 = 10 \text{ GeV}^2$ and the simple quark model prediction to the Q^2 dependence of (2.56). They also constructed a phenomenological model based on vector meson dominance to predict the behavior of I_{GDH} as a function of Q^2 and therefore to correct the interpretation of the EMC data. As argued by Ji and Osborne [23], however, the inclusion of the elastic contribution in (2.56) and the continuous variation of I_{GDH} from $Q^2 = 0$ to $Q^2 = \infty$ are incompatible, since the elastic contribution is absent at $Q^2 = 0$, dominating at small Q^2 and negligible (due to the abrupt fall of the form factors) at high Q^2 . Ji *et al* [24] extended the GDH sum rule at $Q^2 \neq 0$ and calculated the small- Q^2 dependence of I_{GDH} using chiral perturbation theory. Using the dispersion relation connecting the spin structure function $g_1(\nu, Q^2)$ with the forward compton amplitude $\tilde{g}_1(\nu, Q^2)$, they show that

$$\int_{\nu_0}^{\infty} g_1(Q^2, \nu) \frac{d\nu}{\nu} = \frac{1}{4} \left[\tilde{g}_1(Q^2, \nu = 0) \right]_{no \text{ elastic}} \quad (2.58)$$

where the contribution from the elastic intermediate state has been subtracted from the rhs of (2.58). The above equation represents a generalized GDH sum rule, since the rhs is a well defined quantity, calculable in principle. At low Q^2 chiral perturbation theory provides a natural tool to calculate $\left[\tilde{g}_1(Q^2, \nu = 0) \right]_{no \text{ elastic}}$, using the pion mass m_π and the nucleon momentum p as small compared to any other scales in the problem, and hence as the appropriate expansion parameters. Ji *et al* find that $\left[\tilde{g}_1(Q^2, \nu = 0) \right]_{no \text{ elastic}}$ is independent of Q^2 at $\mathcal{O}(p^3)$, whereas at $\mathcal{O}(p^4)$

$$\left[\tilde{g}_1^{\mathcal{O}(p^4)}(0, Q^2) \right]_{no \text{ elastic}} = \frac{g_A^2 \pi m_\pi}{8(4\pi f_\pi)^2 M} \left[-2\kappa_1 + \left(4\kappa_1 + \frac{Q^2}{m_\pi^2} \kappa_2 \right) \times \sqrt{\frac{m_\pi^2}{Q^2}} \sin^{-1} \sqrt{\frac{Q^2}{4m_\pi^2 + Q^2}} \right] \quad (2.59)$$

with $\kappa_1 = 5 + 6\kappa_V + (1 + 6\kappa_S)\tau^3$, $\kappa_2 = 3 + 6\kappa_V + (3 + 10\kappa_S)\tau^3$, and $\kappa_S = -0.120$ and $\kappa_V = 3.706$ are the experimental values of the isoscalar and isovector anomalous magnetic momentum of the nucleon, respectively, and $\tau^3 = \pm 1$ for the proton and the neutron, respectively. The small Q^2 prediction for the generalized GDH integral I_{GDH} is

$$I_{GDH}^p(Q^2) = -\frac{\kappa_p^2}{4} + 6.85 Q^2 (\text{GeV}^2) + \dots \quad (2.60)$$

$$I_{GDH}^n(Q^2) = -\frac{\kappa_n^2}{4} + 5.54 Q^2 (\text{GeV}^2) + \dots \quad (2.61)$$

for the proton and the neutron, respectively.

2.4.4 Unitary Isobar Model

Using the definitions (2.46),(2.48) of the longitudinal-transverse and transverse-transverse cross sections, σ'_{LT} and σ'_{TT} , respectively, the generalized GDH integral I_1 , defined in (2.56), can be written as

$$I_1(Q^2) = -\frac{M^2}{4\pi^2\alpha} \int_{\nu_0}^{\infty} \frac{1-x}{1+\gamma^2} (\sigma'_{TT} + \gamma\sigma'_{LT}) \frac{d\nu}{\nu}. \quad (2.62)$$

The unitary isobar model (UIM), developed by the Mainz group [27][28][26], calculates the cross sections σ'_{LT} and σ'_{TT} and provides a prediction for $I_1(Q^2)$, based on a multipole analysis of single pion photo- and electroproduction. Figure 2.9 shows the predicted dependence of I_1 on Q^2 for the proton and for the neutron. It is seen that, while the model is in accord with the GDH sum rule at the real photon point ($Q^2 = 0$) for the proton, this is not the case for the neutron.

The behavior exhibited by I_1 , illustrated in Figure 2.9, triggered a host of theoretical work in recent years. The strong variation with Q^2 , starting from the real photon limit, the zero crossing, up to the DIS limit, is a direct manifestation of the change of the relevant degrees of freedom, namely the transition from resonance-driven coherent processes to incoherent scattering off the nucleon constituents.

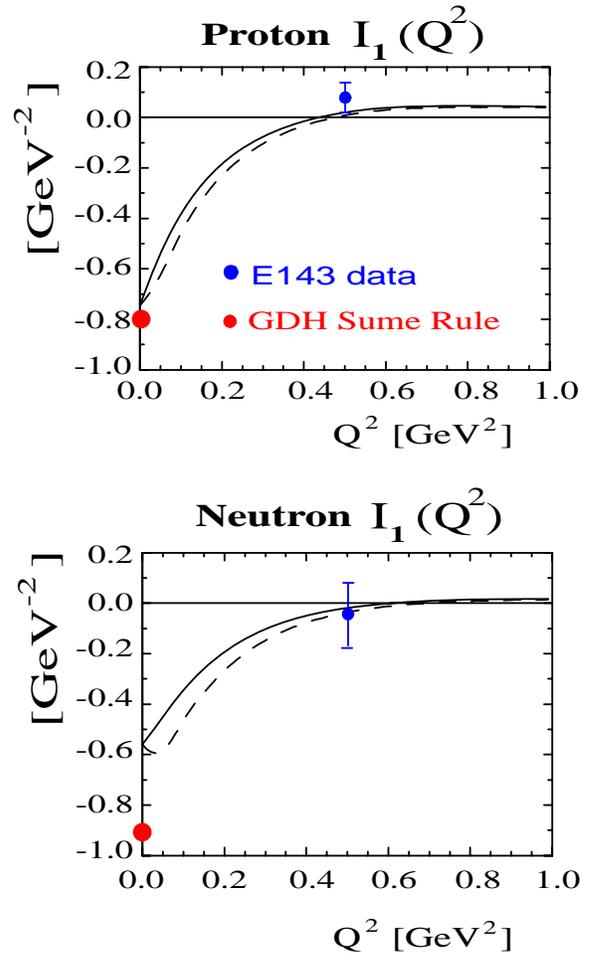


Figure 2.9: UIM prediction for $I_1(Q^2)$, from [25]. The integrals are integrated up to $W_{max} = 2$ GeV. The solid (dashed) lines contain (omit) the σ'_{LT} contribution.

Bibliography

- [1] M. Anselmino, A. Efremov, E. Leader, Phys. Rep. **261** (1995)
- [2] W. Melnitchouk, Jlab Publication, JLAB-THY-00-18 (2000)
- [3] A.V. Manohar, hep-ph/9204208
- [4] F.E. Close, Rep. Prog. Phys. **42**, 1285 (1979)
- [5] S.D. Drell, SLAC Publications, SLAC-PUB-5720, 1992
- [6] M.C. Vetterli, hep-ph/9812420
- [7] J.D. Bjorken, Phys. Rev. **148**, 1467 (1966)
- [8] U. Stiegler, Phys. Rep. **277**, 1 (1996)
- [9] P.J. Mulders and T. Sloan, hep-ph/9806314
- [10] M. Gell-Mann, M.L. Goldberger, Phys. Rev. **96**, 1433 (1954)
- [11] F.E. Low, Phys. Rev. **96**, 1428 (1954)
- [12] J. Toll, Phys. Rev. **104** 1760 (1956)
- [13] R. Pantförder, Ph.D. Thesis, University of Bonn, 1998
- [14] M. Gell-Mann, M.L. Goldberger, W.E. Thirring, Phys. Rev. **95** 1612 (1954)
- [15] S.D. Drell and A.C. Hearn, Phys. Rev. Letters **16**, 908 (1966)
- [16] S.B. Gerasimov, Sov. Journal of Phys. **2**, 430 (1966)
- [17] C. Itzykson and J.B. Zuber, *Quantum Field Theory*, McGraw-Hill, 1980
- [18] M. Duren, Nucl.Phys.Proc.Suppl. **79** 766 (1999)

- [19] L.N. Hand, Phys. Rev **129**, 1834 (1963)
- [20] R.L. Jaffe and Xiangdong Ji, Phys. Rev. D **43**, 724 (1991)
- [21] J. Kodaira, Prog. Theor. Phys. Suppl. **120** 37 (1995)
- [22] M. Anselmino, B.L. Ioffe, and E. Leader, Sov. J. Nucl. Phys. **49**, 136 (1989)
- [23] X. Ji and J. Osborne, hep-ph/9905410
- [24] X. Ji, C. Kao and J. Osborne, Phys. Lett B472, 1 (2000)
- [25] D. Drechsel, S.S. Kamalov and L. Tiator, hep-ph/0008306
- [26] L. Tiator, D. Drechsel and S.S. Kamalov, nucl-th/0005061
- [27] D. Drechsel, O. Hanstein, S.S. Kamalov and L. Tiator, Nucl. Phys. **A645**, 145 (1999)
- [28] D. Drechsel, S.S. Kamalov, G. Krein and L. Tiator, Phys. Rev. D **59**, 094021

Experimental Apparatus

3.1 The Accelerator and the Polarized Electron Source

The Continuous Electron Beam Accelerator Facility (CEBAF) of Jefferson Lab has the capability of delivering cw beam to three experimental halls. The racetrack shaped accelerator is shown in Figure 3.1. The source of the injector is a strained GaAs cathode providing polarized beam of about 70% polarization (at the time of E-94010) and maximum current of $50\text{-}70\mu\text{A}$, depending on the quantum efficiency of the photocathode. The beam first enters the first accelerator module, where it is accelerated to 45 MeV, and then injected into the North Linac.

At the end of the North Linac, the beam enters the east recirculation arc and continues into the South Linac. Both linacs consist of 20 cryomodules and provide a nominal gain of 400 MeV. However, this gain can be tuned up to about 500 MeV, if required by the experimental halls. Each cry-

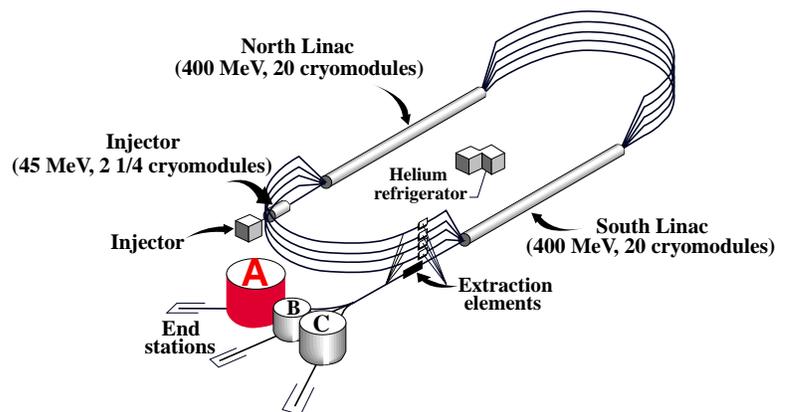


Figure 3.1: Thomas Jefferson National Accelerator Facility.

omodule contains [1] eight 1497 MHz superconducting niobium cavities operating at 2 K, powered by a 5 kW klystron [2] and providing a gradient of 6.5 MV/m. At the end of the South Linac the beam can either be extracted into the experimental halls, or circle around

the west recirculation arc for another pass around the accelerator. There can be a maximum of 5 passes, which brings the maximum beam energy to about 5 GeV. By tuning the RF in the superconducting cavities [3] the energy gain of each pass can be tuned by a few tens MeV. At the extraction point there are deflecting cavities and septum magnets that guide the beam into the experimental halls, each hall receiving an electron bunch at a frequency of 499 MHz, the bunch length being 1.7 ps.

The polarized source is an evolved version of the GaAs source first used at SLAC in 1978 [4]. Its operation is governed by two basic principles [5] : **(i)** illumination of the semiconductor with circularly polarized light to produce polarized electrons in the conduction band, and **(ii)** addition of monolayer coverages of alkali metals (usually cesium) and oxidants (like NF_3) to the surface of the photocathode, with the effect of lowering the work function and permitting the polarized electrons to escape. It was only recently (1990's) established that strained GaAs photocathodes can produce much higher polarizations.

As is shown in Figure 3.2(a), due to the degeneracy of the $P_{3/2}$ sub-levels of the valence band, both the $m = 1/2$ and the $m = 3/2$ sub-levels can absorb light (red arrows). Due to the relative transition probabilities (1:3), the maximum achievable polarization in the conduction band is 50%. By growing a thin film of GaAs on a $\text{GaAs}_{1-x}\text{P}_x$ substrate, a uniaxial stress perpendicular to the emitting surface is produced, and the degeneracy is lifted (Figure 3.2(b)). The theoretical maximum polarization is in this case 100%, since only the $m = 3/2$ sublevel can absorb the light. In practice polarizations over 70% are obtained. The

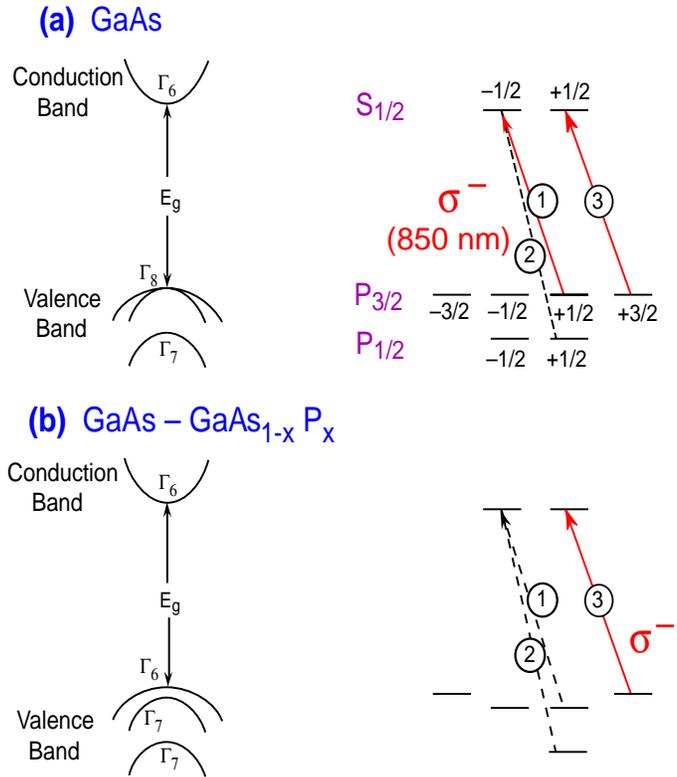


Figure 3.2: Energy level diagram for (a) bulk and (b) strained GaAs, from [4].

polarized beam exiting the source has imposed on it the accelerator RF structure [6], by virtue of three lasers operating at 499 MHz, which produce three interleaved bunches that are then delivered to the experimental halls. The intensity of each laser meets the current requirement of each hall. The helicity of the lasers, and hence the helicity of the electron beam, is continuously flipped by means of a Pockels cell, at a rate of 1 Hz (30 Hz at the very beginning of the experiment). Thus, the effects of long term drifts of the beam parameters on the event count rates per helicity state are avoided.

3.2 Beam Energy Measurement

3.2.1 Introduction

The accurate knowledge of the beam energy is very crucial for the whole physics program of Hall A, since many scattering parameters (such as momentum transfer) as well as the physical quantities to be measured (such as elastic cross sections) sensitively depend on beam energy [11].

Currently there exist two methods for measuring the beam energy, the e-p measurement, based on elastic electron-proton scattering, and the arc-measurement, based on beam deflection in a known magnetic field in the beamline. Both methods provide an accuracy of $\frac{\delta E_{beam}}{E_{beam}} \approx 10^{-4}$.

3.2.2 Arc Measurement

The arc-measurement relies on the 40m long bending section of the beamline (the “arc” section) located after the beam switch-yard and before the Hall-A End Station. It consists of 8 dipole magnets, each followed by

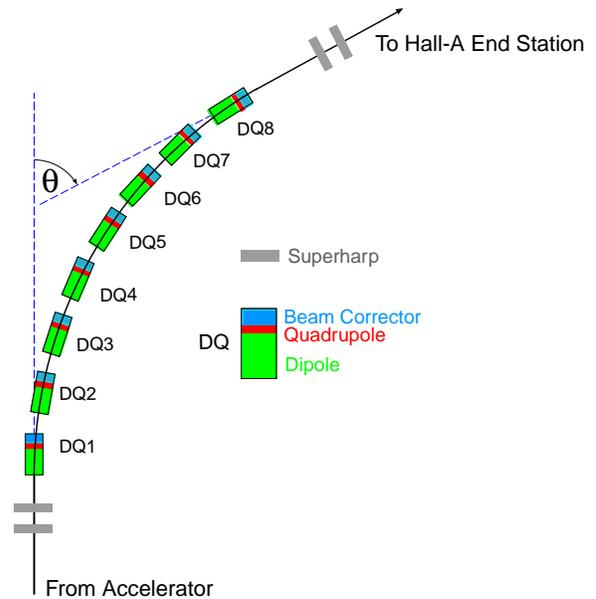


Figure 3.3: The arc section of the beamline.

a quadrupole magnet and a beam corrector magnet, as shown in Figure 3.3. This configuration results in an achromatic (quadrupoles on) bend of 34.3° . If the arc is operated in

the dispersive mode (quadrupoles off), the beam energy is related to the field integral along the path of the beam, $\int B dl$, and the total bend angle, θ , as:

$$E_{beam} = \frac{e}{\theta c} \int B dl \quad (3.1)$$

The bend angle θ is measured by two pairs of wire scanners (superharps), one located upstream, and the other downstream of the arc. Each scanner moves horizontally three vertical tungsten wires ($20 \mu m$ in diameter) across the beam. The induced bremsstrahlung is detected by a PMT located a few meters downstream. A typical accuracy of the horizontal position of the beam barycenter with respect to the external fiducial is $15 \mu m$. The survey of both pairs of external fiducials is done optically. The resultant relative error of the bend angle is about 2.2×10^{-5} . The field integral is determined by an accurate measurement of the field of a reference dipole magnet, powered in series

with the 8 arc dipoles. All arc dipoles have been pre-calibrated relative to the reference dipole on the ‘‘Dipole Stand’’ of Jefferson Laboratory. The relative error of the field integral is about 10^{-4} , and is the dominant error in the energy measurement.

3.2.3 E-P Measurement

In this method the beam energy is determined by measuring the electron scattering angle θ_e and the proton recoil angle θ_p in the elastic reaction ${}^1H(e, e')p$ [12]. Let $k_\mu = (E, \mathbf{k})$ and $p_\mu = (M, 0)$

be the incoming electron and target proton 4-vectors, respectively, $k'_\mu = (E', \mathbf{k}')$ and $p'_\mu = (E_p, \mathbf{p})$ the scattered electron and proton 4-vectors. Using 4-momentum conservation ($k_\mu + p_\mu = k'_\mu + p'_\mu$), it follows that the beam energy is given by

$$E_{beam} = M \frac{\cos\theta_e + \sin\theta_e / \tan\theta_p - 1}{1 - \cos\theta_e} \quad (3.2)$$

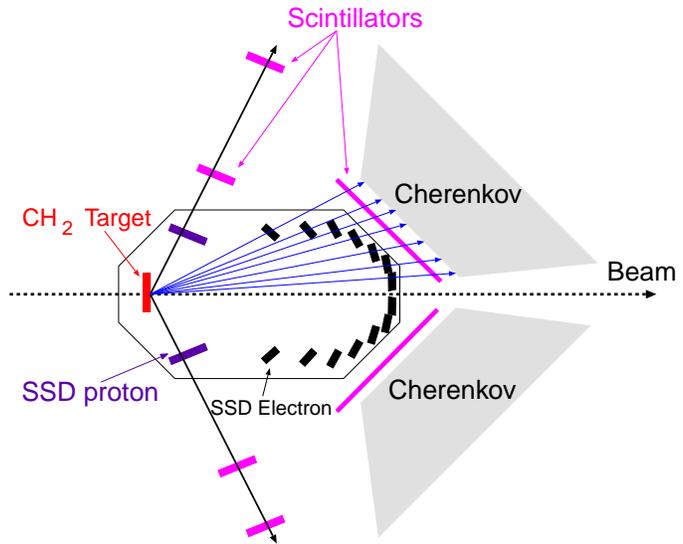


Figure 3.4: Sideview of the e-p apparatus.

The arrangement of the measuring apparatus is schematically shown in Figure 3.4. The recoil proton is detected at an angle of about 60° , in coincidence with the scattered electron, which is detected at an angle between 9° and 40° , depending on beam energy.

The deviation of the position and direction of the beam from its ideal trajectory will obviously shift the beam energy extracted from (3.2), by introducing a shift $\delta\theta$ to the angles θ_e and θ_p . The real scattering angles would then be $\theta_e - \delta\theta$ and $\theta_p + \delta\theta$, respectively. To cancel the first order dependence on $\delta\theta$, the beam energy is measured by two detectors, positioned symmetrically with respect to the ideal beam trajectory as depicted in Figure 3.4. Then the average $E_{beam} = (E_1 + E_2)/2$ will depend only to second order on $\delta\theta$.

The scintillators provide the trigger and the Cherenkov detectors are used for electron identification. The coplanarity requirement for the incident and scattered electron and the recoil proton is used to select the elastic events. The scattering angles are determined by the Silicon Strip Detectors (SSD), which have a bin width of $100 \mu\text{m}$. The spatial resolution is $28 \mu\text{m}$ [13].

The target is a $13 \mu\text{m}$ thin rotating $(CH_2)^n$ tape, and the uncertainty in its position (about $10 \mu\text{m}$) is one of the main sources of systematic errors, the other being the detector position uncertainty (about $15 \mu\text{m}$). The resulting relative error of the measurement is between 1.5×10^{-4} and 3.0×10^{-4} .

	e-p	Arc	e- ^3He
1-pass	-	-	862.0
2-pass	1717.9	-	1716.9
3-pass	-	2584.0	-
4-pass	3381.8	3385.0	-
5-pass	4238.6	4240.5	-
5-pass	-	5059.3	-

Table 3.1: Results of energy measurements.

3.2.4 e- ^3He Measurement

With 1-pass and 2-pass beams, data were collected on elastic $^3\text{He}(e, e')$ scattering, to serve as a combined systematic check of both the ^3He target and the spectrometers (see section 5.4). From the elastic peak, and knowing the absolute momentum setting of the spectrometers (see section 3.8), the beam energy can be calculated [3]. Table 3.1 shows the results

of all measurements.

3.3 Hall-A Beamline

The Hall-A beam line, starting after the arc section and leading up to the target (Figure 3.5) consists of a Compton polarimeter (not used in this experiment), two Beam Current Monitors (BCM) and the Unser monitor (for absolute beam current measurement) in between them, the fast raster, the e-p device, and the Moller beam polarimeter.

Furthermore, along the beamline there are a number of Beam Position Monitors (BPM). At the end of the beamline there is the target pivot, which is viewed by the two magnetic spectrometers, the electron spectrometer (E-Arm) and the hadron spectrometer (H-Arm). The latter is used for detection of hadrons in coincidence ex-

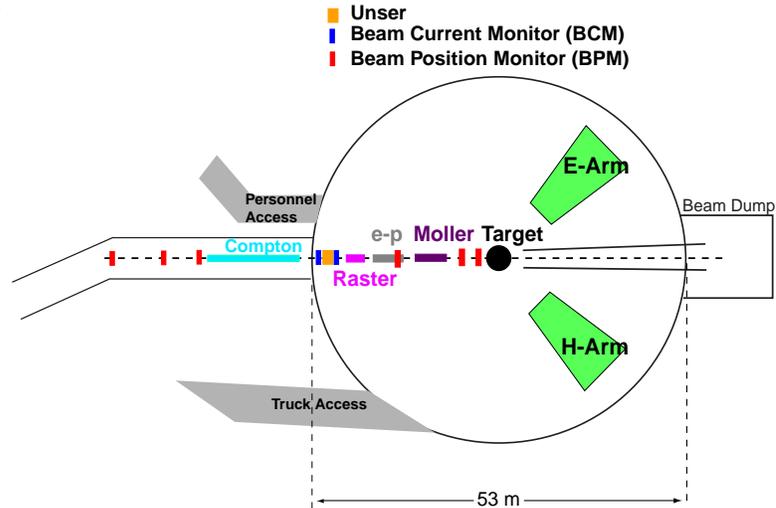


Figure 3.5: Hall-A beamline.

periments. However, E-94010 is an inclusive experiment, and both spectrometers were used for detecting electrons. All the beamline elements will be described in more detail in the following sections.

3.4 Beam Current Measurement

Relative changes of the beam current are monitored by two Beam Current Monitors (BCMs) which are located 25 m upstream the target. The BCMs are stainless steel cavities tuned to the beam frequency (1497 MHz). In each cavity there are two coaxial loop antennas, one used for calibration, and the other for picking up the beam-induced (TM_{010} mode) signal. Between the two BCMs there is an UNSER monitor, which is [7] a zero flux current transformer designed for absolute non-destructive (as opposed to the Faraday cup located

at the injector) current measurement. The Unser monitor is calibrated by passing a known current through a wire inside the beampipe. It requires extensive magnetic shielding and temperature stabilization to reduce noise and zero drift. As its output signal drifts significantly on a time scale of several minutes, it cannot be used to continuously monitor the beam current. Thus the BCMs are calibrated against the Unser in dedicated calibration runs, and they provide the long term current monitoring. During the calibration runs the beam is turned on and off for a few times. When it is on the current is set at about $40 \mu\text{A}$, since the Unser monitor has an absolute uncertainty of 250 nA [8], independent of current. When the beam is off, the Unser output drift is measured and removed afterwards when calibrating the cavities. During normal data taking the signals from the BCM cavities are fed into the data stream in two ways, the sampled data and the integrated data. The sampled data results from digitizing the instantaneous cavity voltages at quasi-regular intervals (4 sec, 10 sec or 50 sec). The integrated data results from down-converting the cavity signals to DC and then generating a signal the frequency of which is proportional to that DC level (so called VTOF converter). This signal is fed into a frequency counter, the time integrated output of which (being proportional to the total charge) is included as part of the charge scaler event in the scaler file. The uncertainty of the current measurement is no more than 1%, resulting primarily from the nonlinear BCM response at low currents (a few μA).

3.4.1 Effect of the Charge Uncertainty on Polarized Cross Section Differences

The physics observables are extracted from the difference of polarized cross sections $\sigma^+ - \sigma^-$, where σ^+ (σ^-) represents the cross section with beam and target polarizations being parallel (antiparallel). These cross sections are proportional to the event counts, N^\pm , in each beam helicity state, normalized by the accumulated charge, Q^\pm , so that

$$\sigma^+ - \sigma^- \sim \frac{N^+}{Q^+} - \frac{N^-}{Q^-} = \frac{1}{Q^+} \left(N^+ - \frac{Q^+}{Q^-} N^- \right) \quad (3.3)$$

Since the systematic error of the charge is not helicity correlated, the error in $\frac{Q^+}{Q^-}$ cancels at first order. Hence the error in $\sigma^+ - \sigma^-$ due to the charge uncertainty, δQ , is proportional to δQ , that is, less than 1%.

3.5 Beam Raster and Beam Position Monitors

In order to avoid locally overheating the target, the electron beam has to be rastered. The raster hardware is located 23 m upstream of the target. It consists of two sets of steering magnets, which steer the beam in the plane transverse to the central beam direction. A pair of amplitude-modulated ($f_{mod} = 49$ Hz, square-root shape) sine waves of frequency 20 kHz is applied to the magnets, the two sine waves having a phase difference of $\frac{\pi}{2}$. The resulting beam spot has an elliptical envelope, with dimensions 4 mm \times 4 mm, approximately. The transverse position of the beam on the target and

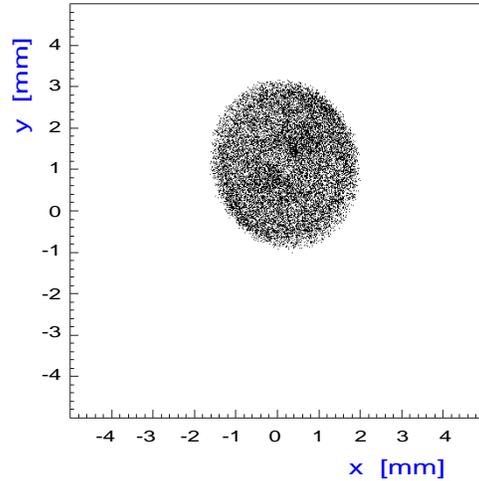


Figure 3.6: Typical beam spot resulting from beam rastering.

the angle with respect to the nominal beam direction are measured by two Beam Position Monitors (BPM) located 1.3 m and 7.5 m upstream the target. Each BPM consists [7] of a 4-wire antenna array tuned to the fundamental frequency of the beam. The standard difference-over-sum technique is then used to determine the relative position of the beam to within 100 μ m. The absolute position of the BPMs can be calibrated by (beam destructive) wire scanners (superharps) which are located adjacent to each of the BPMs. The combined use of raster current data and BPM data [9] results in an uncertainty of $\Delta x = \Delta y \approx 0.2$ mm in the beam position x and y.

3.6 Electron Beam Polarimetry

3.6.1 Møller Polarimetry

Møller polarimetry utilizes high energy polarized electron scattering off a fixed target of polarized electrons. By measuring the asymmetry of the scattered electron rates with beam and target polarizations parallel or antiparallel, the beam polarization can be determined once the target polarization is known.

The Møller polarimeter consists of a magnetized ferromagnetic foil that provides the polarized electron target, a spectrometer (3 quadrupoles and a dipole) to define the kinematic range of the scattered electrons, and a detector.

In lowest order, Møller scattering is described by the two diagrams shown in Figure 3.7. The incoming electrons have momentum and spin vectors $k_{1(2)}$ and $s_{1(2)}$, respectively, and the polarization of the outgoing electrons is unobserved. Since $s = (k_1 + k_2)^2 \leq 5 \times 10^{-3} GeV^2$, and $M_Z^2 \approx 10^4 GeV^2$, the Z^0 -exchange diagrams

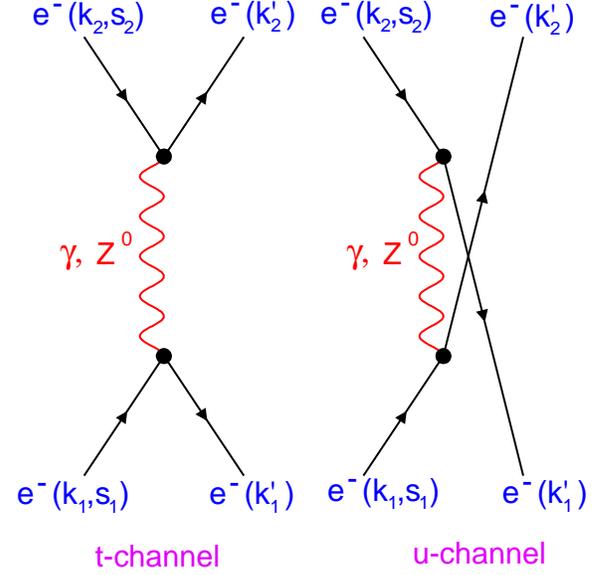


Figure 3.7: Lowest order Møller scattering diagrams.

are negligible. If the beam and target electron polarizations are denoted by P^b and P^t , respectively, then the polarized cross section is given by [10]

$$\frac{d\sigma}{d\Omega}(P^b, P^t) = \frac{d\sigma_{unpol}}{d\Omega} \left(1 + \sum_{i=X,Y,Z} P_i^b P_i^t A_{ii} \right) \quad (3.4)$$

with

$$\frac{d\sigma_{unpol}}{d\Omega} = \frac{\alpha^2}{s} \left(\frac{3 + \cos^2 \theta_{CM}}{\sin^2 \theta_{CM}} \right)^2 \quad (3.5)$$

$$A_{ZZ} = - \frac{(7 + \cos^2 \theta_{CM}) \sin^2 \theta_{CM}}{(3 + \cos^2 \theta_{CM})^2} \quad (3.6)$$

$$A_{XX} = - \left(\frac{\sin^2 \theta_{CM}}{3 + \cos^2 \theta_{CM}} \right)^2 \quad (3.7)$$

and

$$A_{YY} = -A_{XX} \quad (3.8)$$

with θ_{CM} being the center of mass scattering angle. It is also assumed that the scattering plane is the X-Z plane with the electron beam direction along the Z-axis. It is easily seen that $|A_{ZZ}^{max}| = |A_{ZZ}(\theta_{CM} = 90^\circ)| = \frac{7}{9}$ and $|A_{XX}^{max}| = |A_{XX}(\theta_{CM} = 90^\circ)| = \frac{1}{9}$. At $\theta_{CM} = 90^\circ$, the laboratory-frame scattering angle θ_{LAB} will be

$$\theta_{LAB} \approx \sqrt{\frac{2m_e}{E_{beam}}} = \frac{1.83^\circ}{\sqrt{E_{beam}[\text{GeV}]}} \quad (3.9)$$

and the unpolarized cross-section

$$\left(\frac{d\sigma_{unpol}}{d\Omega}\right)_{\theta_{CM}=90^\circ} = \frac{182.5}{E_{beam}[\text{GeV}]} \quad \mu\text{barn/sr} \quad (3.10)$$

Measured Asymmetries

In order to cancel the influence of the small transverse polarization component that the beam may have, two asymmetry measurements are made, one with the angle of the foil and the beam being $\theta \approx 20^\circ$ and the other at an angle $\pi - \theta \approx 160^\circ$, as shown in Figure 3.8. The corresponding asymmetries will then be:

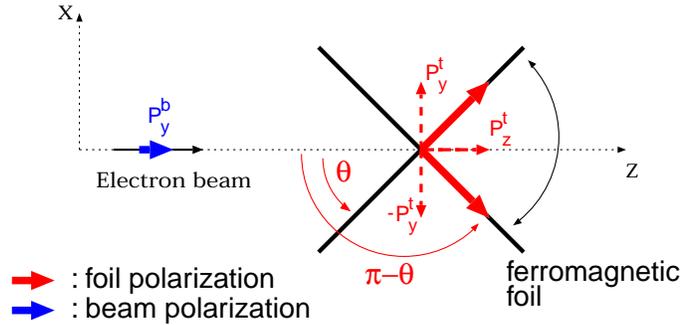


Figure 3.8: Møller target orientation.

$$A_{measured}^\theta = A_{ZZ}P_Z^bP_Z^t\cos\theta + A_{XX}P_X^bP_X^t\sin\theta \quad (3.11)$$

$$A_{measured}^{\pi-\theta} = -A_{ZZ}P_Z^bP_Z^t\cos\theta + A_{XX}P_X^bP_X^t\sin\theta \quad (3.12)$$

Then the beam longitudinal polarization will be $(A_{measured}^\theta - A_{measured}^{\pi-\theta})/2P_Z^t\cos\theta$.

Møller Polarimeter

A schematic layout of the Møller polarimeter is shown in Figure 3.9. The polarized electron target is a $12\mu\text{m}$ thick supermendur foil, the relative angles of which are measured by a scale engraved on the target holder. The absolute angle of the foil with respect to the beam is determined from the event rates. The foil is magnetically saturated by two external Helmholtz coils providing a field of about 300 G along the

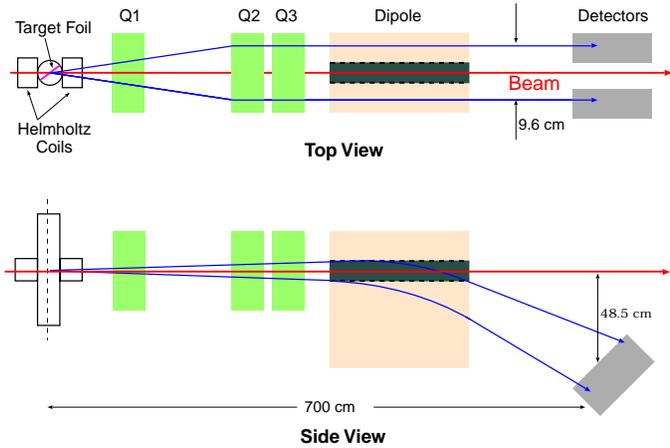


Figure 3.9: Møller polarimeter apparatus.

beam axis at the target center. The foil magnetization is measured by changing the field and measuring the voltage across the pick-up coils wound around the foil. The results of all the measurements done during the experiment are displayed in Figure 3.10. The error-bars of the individual measurements shown are statistical only. The systematic error of the measurement is about 3%, and it is dominated by the uncertainty in the target foil polarization.

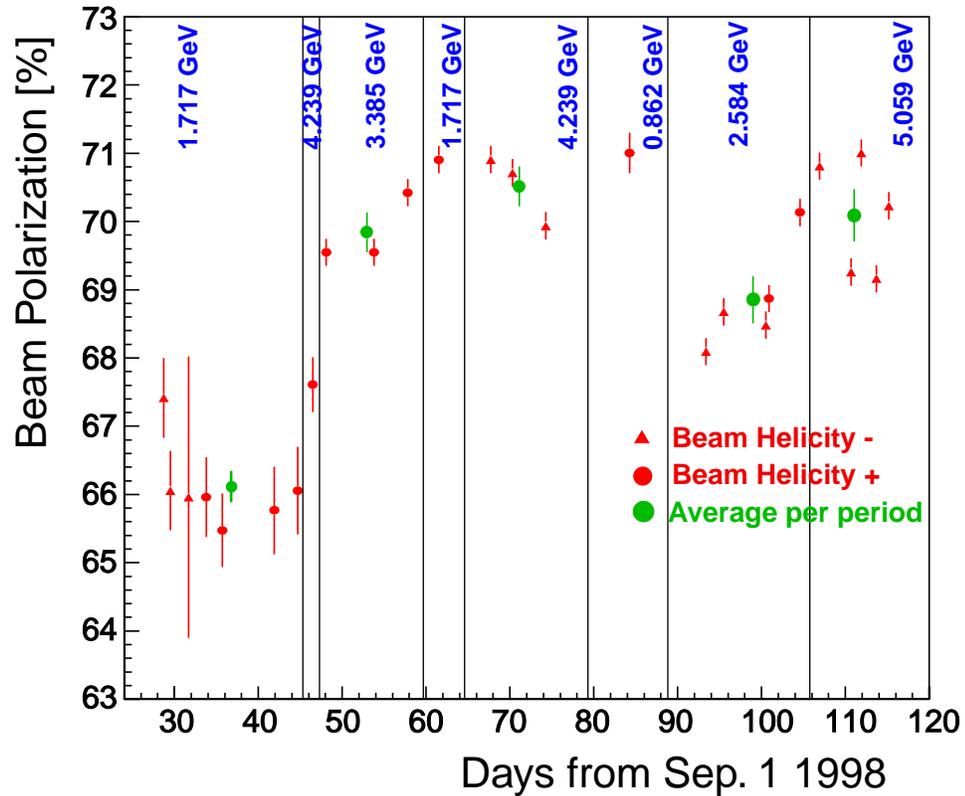


Figure 3.10: E-94010 beam polarization history.

3.7 The Polarized ^3He Target

The ^3He target is based on alkali-metal optical pumping and spin exchange with ^3He . The principles of operation are described in detail in Chapter 4. Here we will briefly describe the general layout of the target, as part of the experimental apparatus. The schematic shown in Figure 3.11 illustrates the basic components of the ^3He target, which are the laser system and the target assembly. Two pairs of Helmholtz coils (only one of which is shown in Figure

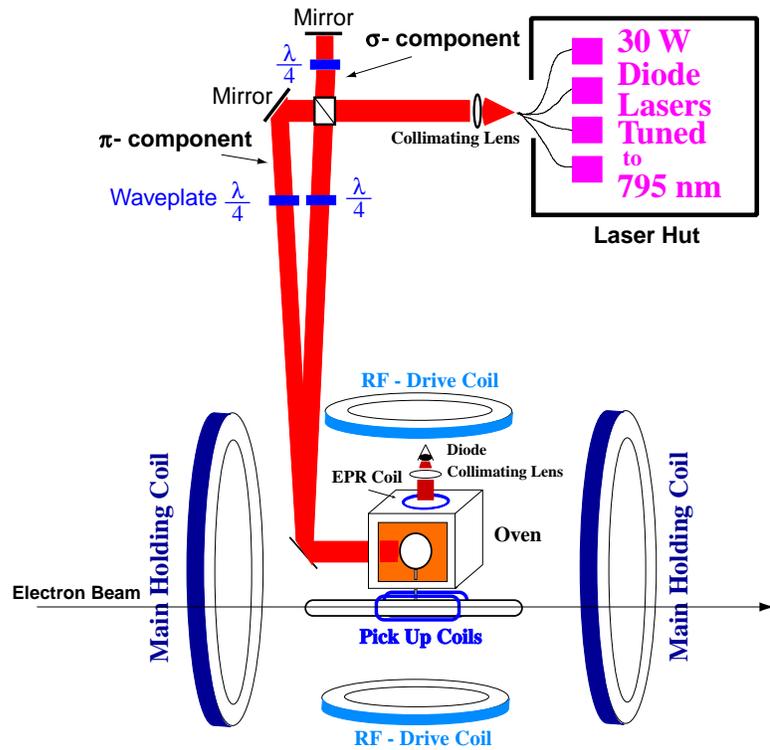


Figure 3.11: Simplified diagram of the polarized ^3He target.

3.11) create a holding field of 25 Gauss. The two pairs of coils are perpendicular to one another and at 19° with respect to the beamline, in order not to block the scattered electrons. The direction of the field can be arbitrarily set at any angle with respect to the electron beam (see Figure 3.12), by relatively adjusting the currents flowing through the Helmholtz coils. This angle was set at either 0° (longitudinal pumping), or 90° (transverse pumping).

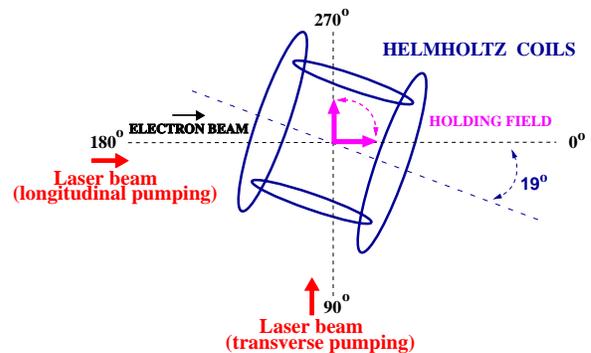


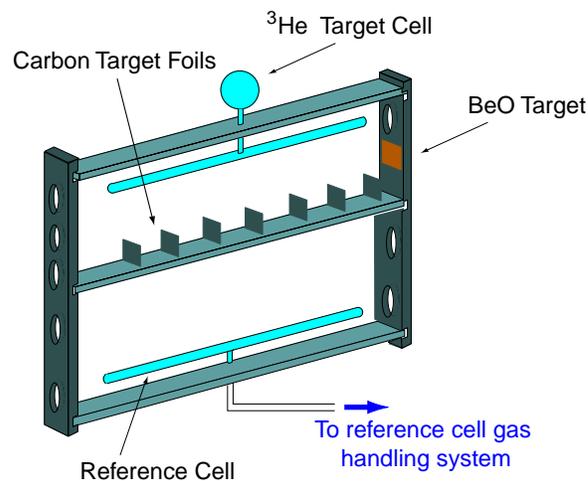
Figure 3.12: Optical pumping geometry with actual Helmholtz coils orientation.

3.7.1 The Laser System

The laser system for optical pumping consisted of seven 30W-diode lasers tuned at 795 nm (Rubidium D1 line), four of which were dedicated to longitudinal and three to transverse pumping. The system of optics used to direct the divergent (12°) laser beam on to the target starts with a collimating lens. A polarizing cube is used to split the light into σ and π components. The π component passes through the cube, reflects off a mirror and then passes through a quarter-waveplate on to the target. The σ component is deflected by the cube by 90° in the direction away from the target. It passes through a quarter-waveplate and is reflected off a mirror into the same waveplate. Its polarization has thus been rotated by 90° . It then passes straight through the cube and through another quarter-waveplate on towards the target. The helicity of the pumping light was -1. The helicity of the longitudinal pumping lasers could be reversed by inserting a half-waveplate in their path. All lasers with the polarizing optics were housed in a concrete hut located near the target in Hall A.

The RF coils, pick-up coils and the EPR coil are used for polarimetry, as described in Chapter 4. The actual ^3He targets are glass cells, the upper (spherical) part of which is located in an oven, as depicted in Figure 3.11.

The oven is heated to $170 - 180^\circ\text{C}$, in order to produce Rb vapor to be optically pumped. An 800 W resistive element was used to heat the air flowing into the oven. The oven temperature was regulated by an RTD (Resistive Thermocouple Device) mounted in the oven.



3.7.2 The Target Ladder

The glass cells were mounted on a target ladder, shown in Figure 3.13, which was attached to the oven. At the bottom of the ladder there is a glass cylinder (reference cell) connected to a gas handling system. Data were acquired with the reference cell at three different modes:

Figure 3.13: Target ladder.

(i) Reference cell filled with N₂

The ³He glass cells contain a small amount of N₂ that assists the optical pumping process. The reference cell data were useful in studying the N₂ dilution.

(ii) Reference cell filled with ³He

Data were taken on elastic ³He(*e, e'*) scattering, in order to check our understanding of the ³He target density in operating conditions using the relative event rates resulting from different (known) ³He pressures in the reference cell.

(iii) Empty reference cell

These data were used in studying the scattering off the cell windows. The Carbon foils shown on the target ladder are used for spectrometer optics studies. The BeO foil is used during beam tuning and for checking the rastered beam pattern. The oven with the attached ladder were being held by a rod that could be moved up or down in order to place the desired target into the beam path.

3.8 The High Resolution Spectrometers

Experimental Hall A is equipped with two very similar High Resolution Spectrometers, the Electron Spectrometer (Electron-Arm) and the Hadron Spectrometer (Hadron-Arm). The latter is known as such because it is used for detection of hadrons in coincidence experiments. As E-94010 was an inclusive measurement, both spectrometers were used to detect electrons, effectively doubling the detection solid angle. Figure 3.14 shows the arrangement



Figure 3.14: High Resolution Spectrometers in Hall-A.

of the spectrometers in the Hall. The Electron (Hadron) spectrometer has a minimum angle of 12.5° (12.5°) with respect to the beamline, and a maximum angle of 165° (130°). During E-94010 the central angles of both spectrometers were fixed at $\theta = 15.5^\circ$, known with an uncertainty of about 0.05° , by comparing the position of the back of the spectrometers to inscribed marks on the floor of the hall. As shown in Figure 3.15, the spectrometers consist of a three quadrupoles and a dipole, all with superconducting coils, in a QQDQ configuration. The central magnetic field in the dipoles, B_0 , is measured by two NMR probes in the Electron-Arm dipole and one NMR probe in the Hadron-Arm dipole. The central momentum will then be $p_0 = \Gamma B_0$, where Γ is the spectrometer constant. To measure Γ the absolute beam energy is required. Elastic $^{12}\text{C}(e, e')$ data was collected in the electron spectrometer in September 1999 [15], followed by ARC and e-p energy measurements. From the elastic peak position, Γ_e can be calculated. By taking coincidence $^{12}\text{C}(e, e'p)$ data with the hadron spectrometer, and measuring the missing energy of the $1p_{1/2}$ state, Γ_h can be calculated using the previously measured Γ_e . It was found that $\Gamma_e = 270.0$ MeV/kG and $\Gamma_h = 269.45$ MeV/kG, both known with an uncertainty of 10^{-3} . The entrance windows of both spectrometers are covered with a 0.18 mm Kapton foil, separated from the scattering chamber by 20 cm of air. After the entrance window and before the first quadrupole there is a box containing three collimators, a sieve slit for optics studies, an 8 cm thick, 6 msr

Spectrometer Properties

Bending Angle	45°
Optical Length	23.4 m
Momentum Range	0.3-4.0 GeV/c
Momentum Acceptance	10%
Momentum Resolution	10^{-4}
Angular Acceptance (Resolution)	
Horizontal	30 mrad (0.5 mrad)
Vertical	65 mrad (1.0 mrad)
Solid Angle	6 msr
Transverse Length	
Acceptance (Resolution)	10 cm (0.1 cm)

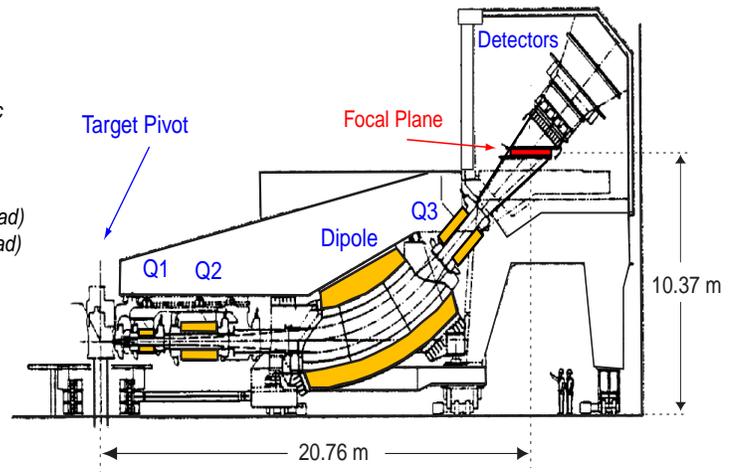


Figure 3.15: High Resolution Spectrometer and basic properties, from [14].

rectangular collimator for defining the acceptance limits of the spectrometer (this was in place for the entire experiment), and an empty collimator.

The Table in Figure 3.15 summarizes the nominal properties of the spectrometer, as given by [14]. The detector hut is separated from the last quadrupole (Q3) by a 0.1 mm thick titanium window.

3.9 The Detector Package

The detectors that are found in the shield house of each spectrometer, just after the quadrupole Q3 (there is a titanium window after the exit of Q3), are shown in Figure 3.16. They start with two vertical drift chambers, used for particle tracking,

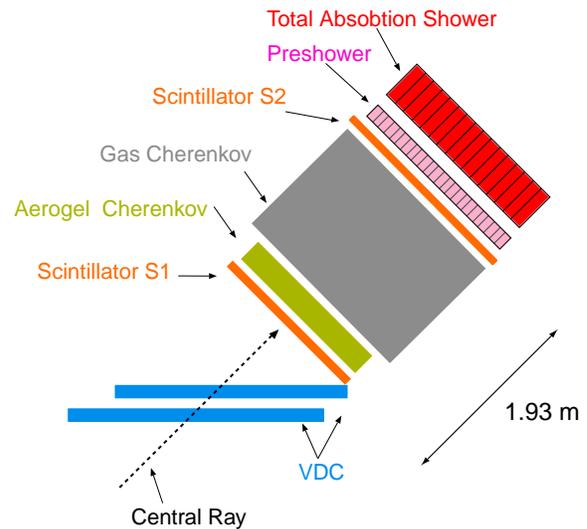


Figure 3.16: Electron-Arm detector package.

followed by one of the two scintillator planes that provide the primary trigger. The gas Cherenkov and the lead-glass calorimeter (consisting of a preshower and a total absorption shower in the Electron-Arm, and just a preshower in the Hadron-Arm) are used for particle

identification. Experiment E-94010 did not use the aerogel cherenkov detectors, nor the carbon analyzer in the Hadron-Arm (which is used for recoil hadron polarimetry). The detector components will be described in more detail in the following sections.

3.9.1 The Scintillators and the Trigger Setup

Scintillators provide the main trigger, called S-Ray, in each spectrometer arm. Each scintillator plane consists of 6 paddles of active area (Bicron BC-408 plastic, 1.1 g/cm^3) viewed by two 2-inch Burle 8575 photomultiplier tubes.

The active volume of the paddles in scintillator S1 (S2) is 36.0 cm (transverse direction) \times 29.3 cm (dispersive direction) \times 0.5 cm ($60.0 \text{ cm} \times 37.0 \text{ cm} \times 0.5 \text{ cm}$). The S-Ray trigger is formed by requiring that scintillator paddles S1 and S2 both fired (both phototubes in each paddle must fire), and that the paddle combination in S1 and S2 belongs to an allowed set. This set demands that the track made approximately a 45° angle with the hall floor. Assuming that paddle N of scintillator S1 fired, then the signal of scintillator S2 must come from paddle N-1, N, or N+1. Table 3.9.1 summarizes the various trigger types.

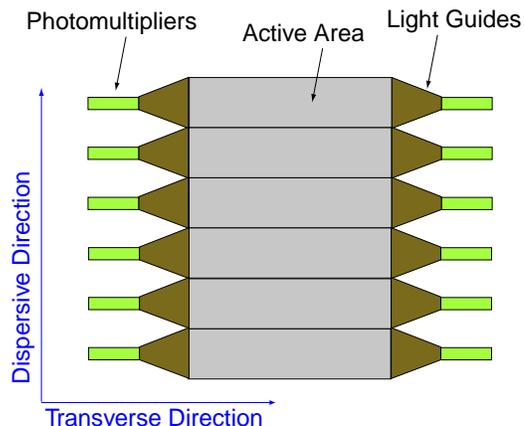


Figure 3.17: Scintillator.

Raw Trigger Type	Description
S1	E-Arm S-Ray (S1 AND S2)
S2	NOT E-Arm S-Ray and one missing out of S1,S2,Cherenkov
S3	H-Arm S-Ray (S1 AND S2)
S4	NOT H-Arm S-Ray and one missing out of S1,S2
S5	S1 and S3 in coincidence (not used in this experiment)

Triggers S1-S5 are counted by the scalers and fed into the Trigger Supervisor (TS). The scalers count the number of triggers of each type produced. Other quantities, such as beam charge, are counted by the scalers. There are three scalers associated to each of these quantities. One counts regardless of the beam helicity, while the other two count only for a given helicity cycle. The Trigger Supervisor provides the interface between the trigger

hardware and the computer data acquisition system. A prescale factor of N is applied independently to each trigger type, that is, TS ignores $N-1$ triggers of that type until the N -th trigger arrives. The accepted triggers are known as $T1 - T5$. The prescale factors are chosen according to the Data Acquisition rate (DAQ), so that the deadtime stays at an acceptable level (usually 30%)

Deadtime

The deadtime is the ratio of the time that the DAQ cannot register an incoming event during a given time interval, over that interval. There are two distinct sources of deadtime: the electronics deadtime and the computer (DAQ) deadtime. The former is less than $1\mu\text{s}$, whereas the latter is the dominant. It results from the time it takes the DAQ system to build an event (about $400\ \mu\text{s}$). The normal event size is about 1 kByte. The computer deadtime limits the maximum achievable DAQ rate to about 2 kHz. During 70% of the experiment we used one DAQ for both arms. For the last 30% of the run a second, independent DAQ was installed, increasing the acquisition rate to 5 kHz.

Trigger Inefficiency

The trigger inefficiency during E-94010 reached values as high as 10%. This was attributed to deteriorating vacuum in the scintillator phototubes. The trigger inefficiency of the electron (hadron) arm was measured by using the secondary triggers $T2$ ($T4$), after applying electron identification cuts in the Cherenkov and Shower detectors. For the Electron-Arm it is given by

$$Inefficiency = \frac{p_2 T_2}{p_1 T_1 + p_2 T_2} \quad (3.13)$$

where p_1 (p_2) is the prescale factor of the main (secondary) Electron-Arm trigger. The same expression holds for the Hadron-Arm with the replacement of $(T1, p1)$ and $(T2, p2)$ with $(T3, p3)$ and $(T4, p4)$, respectively.

3.9.2 The Vertical Drift Chambers

The Vertical Drift Chambers (VDCs) are integral to the performance of the spectrometers, since they are responsible for particle tracking. Both spectrometers are equipped with a

dual-VDC system, each VDC consisting of two wire planes in the standard U-V configuration, as shown in Figure 3.20. The lower VDC almost coincides with the spectrometer focal plane and the one above it enables a precise angular reconstruction of the scattered particle trajectories. Each wire plane has 368 4% gold-plated tungsten sense wires, $20\mu\text{m}$ in diameter and 4.24 mm apart. Each VDC has three high voltage plates at -4 kV, one between the two wire planes, which are 26 mm apart, and two on opposite sides, 26 mm away from each wire plane. The gas supplied to the VDC at a rate of about 10 lt/h is a 62%/38% argon-ethane (C_2H_6) mixture. As shown in Figure 3.20, the ionization electrons created by the incident particle travel from the particle trajectory towards the sense wires on the path of least time. This time is measured by a Time-to-Digital Converter (TDC), which is fed by the sense wire. All TDCs have a common stop provided by the event trigger. Knowing the drift velocity ($50\mu\text{m}/\text{ns}$), the perpendicular distance from the trajectory to the wire plane at each of the fired wires is thus extracted. A track at a nominal (extreme) angle of 45° (52°) with respect to the lab triggers five (three) wires. The per-plane FWHM position resolution achieved is $225\mu\text{m}$ [16].

VDC Efficiency

The hardware efficiency of the VDC wires is almost 100%, so it does not contribute to the VDC inefficiency. The latter is determined by the software inefficiency, that is the ratio of misreconstructed electron tracks to the total number of tracks. Figure 3.19 is a representative distribution of the number of reconstructed tracks, after proper electron identification cuts (see next section) have been applied.

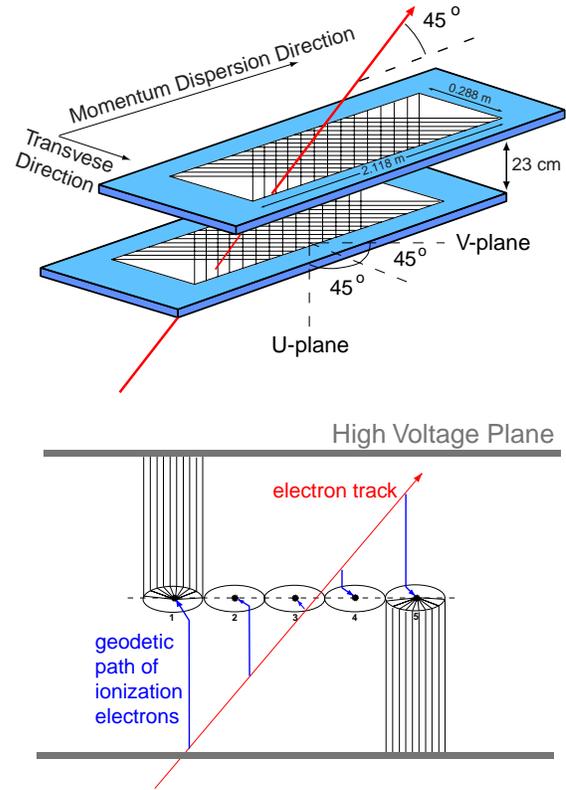


Figure 3.18: Geometry of VDCs.

As can be seen, 99% of the events are one-track events. Zero- three- and four-track events represent about 0.2% of the events and can be safely neglected. There are, however, about 1% two-track events present. They can be attributed [3] to particles knocked off by electrons at the edge of the acceptance and can be cut away, to be included in calculation of the VDC efficiency. Consequently the VDC efficiency is always better than 99%.

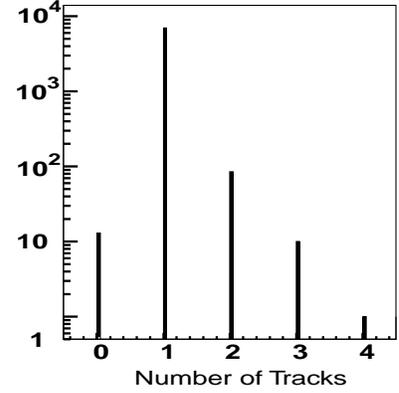


Figure 3.19: Event distribution for the number of tracks in the Electron-Arm.

3.9.3 Electron-Pion Separation

If the energy loss ν is bigger than a threshold value,

$$\nu_{thres} = \frac{1}{2m_n} [Q^2 + (m_p + m_\pi)^2 - m_n^2] \quad (3.14)$$

then pions will be produced through the reaction $\gamma^* + n \rightarrow \pi^- + p$. The detector components responsible for π^-/e^- separation are the threshold Gas-Cherenkov Detector and the Preshower/Shower calorimeter (only preshower in the Hadron-Arm).

The Gas Cherenkov Detector

The radiator in the Cherenkov detector is CO_2 , the index of refraction of which is, at STP, $n=1.00041$ (at the sodium D line) [18].

Any charged particle must have $\beta \geq 1/n$ to produce Cherenkov radiation. Thus, at threshold, $\gamma_{thres} = 35$. For an electron momentum of 0.3 GeV/c, $\gamma_e = 600$, whereas for a pion momentum of 4 GeV/c, $\gamma_\pi = 29$. Thus pions are completely suppressed over the whole momentum range of the spectrometer (0.3-4.0 GeV/c), and electrons always trigger the detector (with an actual inefficiency less than 10^{-3} , as reported in [18]).

The Cherenkov detector provides a pion rejection factor of about 100. The maximum π/e ratio in the kinematics of this experiment

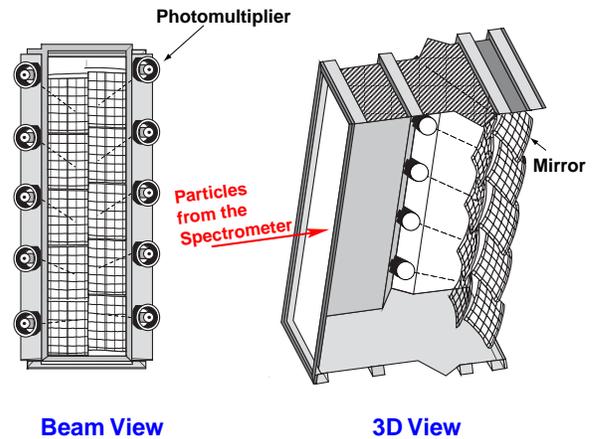


Figure 3.20: Cherenkov detector.

was $(\pi/e)_{max} \approx 5$. Thus the data would be diluted with pions up to 5%, if the Cherenkov detector alone was the only means of $e - \pi$ separation. Furthermore, pions can knock off electrons (so called δ -electrons) in the material preceding and including the gas-Cherenkov. The δ -electrons will trigger the Cherenkov, and would be misidentified as "good" electrons, were the Cherenkov the only detector available for particle identification. Both of the aforementioned problems are overcome by the electromagnetic shower calorimeter. The shower detector provides an additional pion rejection factor of about 30, bringing the pion dilution of the data to the neglectable level of no more than 0.2%. Moreover, the shower detector can separate δ - from "good"- electrons based on the deposited energy. In the following, the methodology of $e - \pi$ separation with the combined use of the Cherenkov and shower detectors will be detailed.

Electron Arm Total Absorption Shower Detector

The Shower detector in the Electron-Arm is a total absorption calorimeter, consisting of two parts : a preshower, made out of 48 blocks ($35 \times 10 \times 10$ cm) , and contributing 3.7 radiation lengths seen by the beam, and a total absorption shower, consisting of 96 blocks ($15 \times 15 \times 35$ cm), providing 14 additional radiation lengths. The layout of these detectors is shown in Figure 3.21. The preshower (shower) is made of lead-glass TF-1 (SF-5), and each block is viewed from the side (from behind) by a Hamamatsu R3036 photomultiplier.

Shower Detector Calibration

A cluster is defined as a group of blocks (2×3 for the preshower and 3×3 for the shower) which have an energy deposition. An electron crossing the detector would ideally form a cluster in both the preshower and the shower, and the positions of these clusters should coincide with the point on each detector, which the reconstructed track would cross. One has to calibrate the preshower and the shower together, since the sum of the energies deposited in them is the energy of the incoming electron, that is, $E_e = p_e$, where p_e is the electron momentum. The calibration procedure consists of selecting electron events, identifying the main clusters in the preshower and shower detectors, and minimizing the following functional, using the

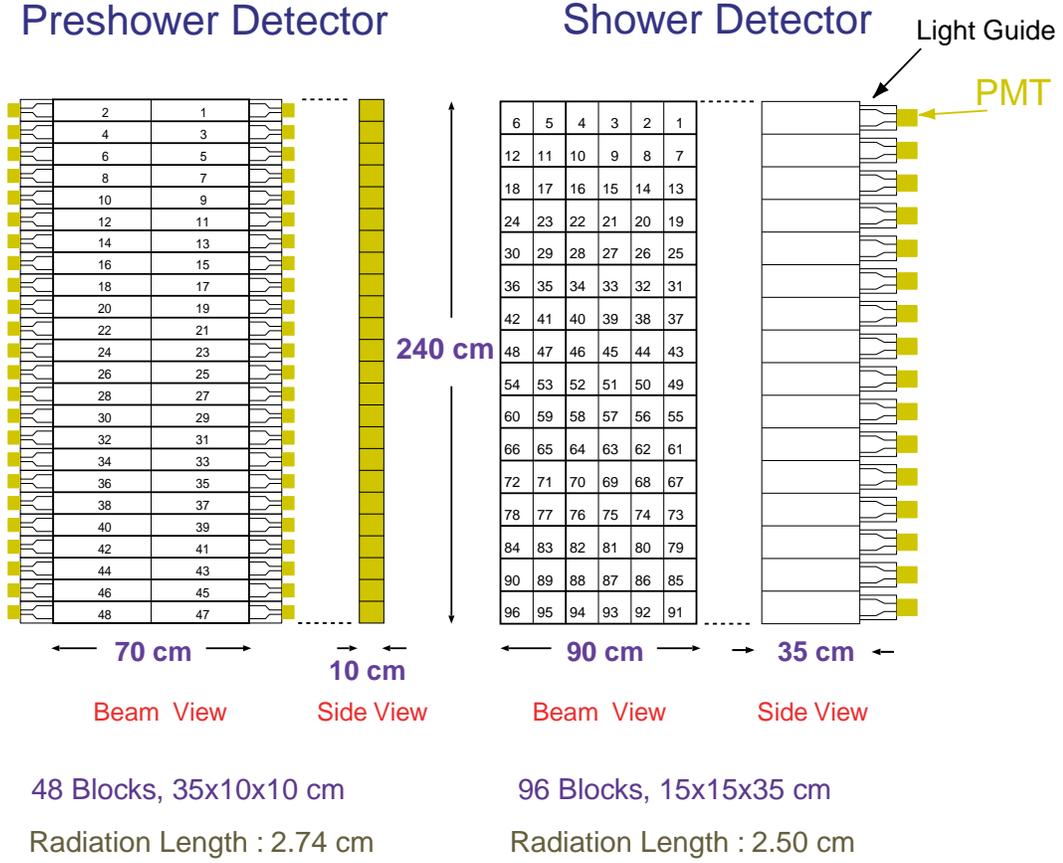


Figure 3.21: Shower detector of Electron-Arm, beam view.

calibration coefficients C_j^{psh} and C_j^{sh} as free parameters:

$$\chi = \sum_{i=1}^N \left[\sum_{j \in M_{psh}^i} C_j^{psh} (A_{j,psh}^i - P_{j,psh}) + \sum_{j \in M_{sh}^i} C_j^{sh} (A_{j,sh}^i - P_{j,sh}) - p_e^i \right]^2 \quad (3.15)$$

where

N is the number of events used for the calibration

M_{psh} is the cluster identified in the preshower

$A_{j,psh}^i$ is the amplitude of the j -th block of the preshower that fired in the i -th event

$P_{j,psh}$ is the pedestal of the j -th block of the preshower

p_e^i is the electron momentum in the i -th event

and similarly for the shower variables M_{sh} , $A_{j,sh}^i$ and $P_{j,sh}$. Figure 3.22 shows the dependence of the relative width of the electron E/p peak as measured after the detector response

has been calibrated. The width of the electron E/p peak resulting from a Gaussian fit is σ .

e- π Separation in the Electron Arm

The Cherenkov cut, that is, the requirement that the Cherenkov detector triggered is the first cut applied, in order to achieve e- π separation. Figure 3.23(a) shows the E/p distribution measured by the preshower detector, where E is the sum of the energies deposited in the preshower and the shower, $E_{\text{preshower}}$ and E_{shower} , respectively. Figure

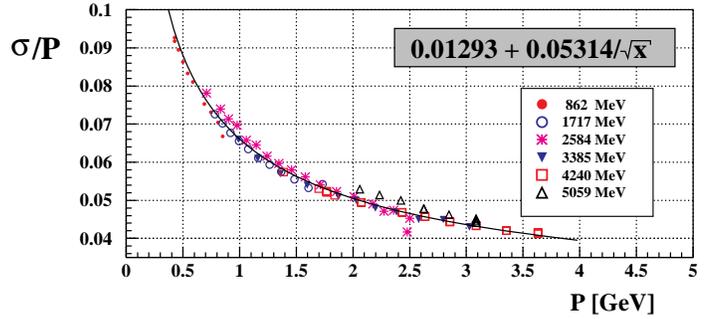


Figure 3.22: Resolution of Electron-Arm preshower/shower detector as a function of electron momentum, from [20].

3.23(b) shows the same distribution after the Cherenkov cut has been applied. As men-

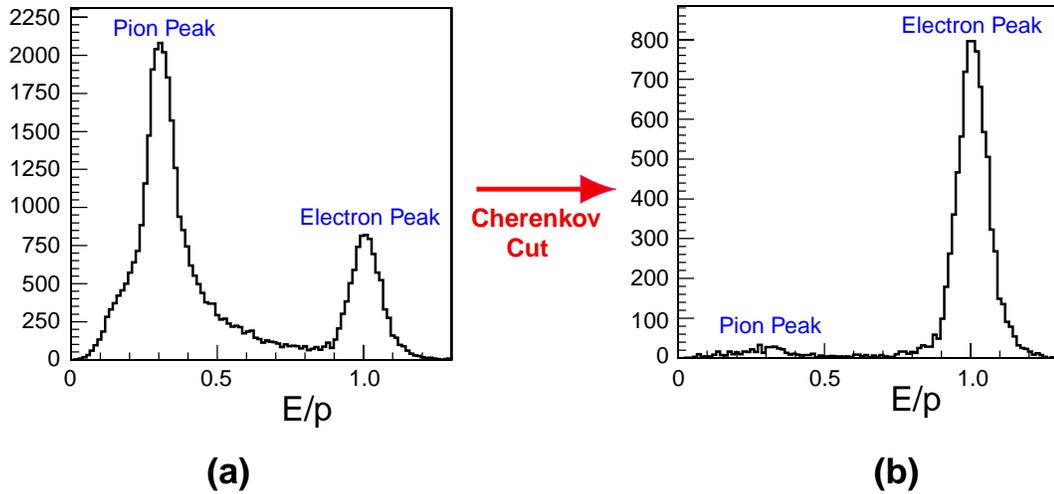


Figure 3.23: Effect of the Cherenkov cut on the E/p distribution in the shower detector. (a) E/p distribution prior to the cut. (b) E/p distribution after the cut. For the data shown the beam energy is $E_{\text{beam}}=5058$ MeV and the spectrometer momentum setting $p_0=2046$ MeV.

tioned before, the pion rejection factor that the Cherenkov cut provides is about 150. An additional factor between 1 and 2 is gained by applying a cut in $E_{\text{preshower}}/p$, as shown

in Figure 3.24(a). Finally, a cut is applied in E/p (Figure 3.24(a)), which suppresses the pions by a factor of about 10. The total pion rejection factor is thus $\pi_{rejection} \approx 2000$. The cuts in the preshower and in the sum of shower and preshower are chosen so that they

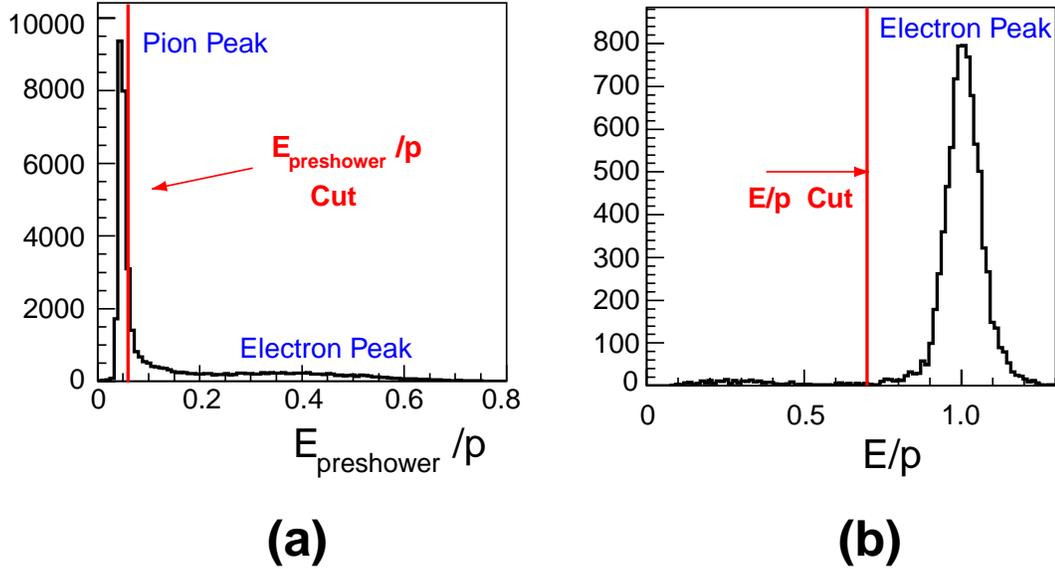


Figure 3.24: (a) $E_{preshower}/p$ cut. (b) E/p cut.

maximize the total pion rejection factor and at the same time minimize the loss of "good" electron events, that is, maximize the electron identification efficiency, ID_{eff} . The latter is estimated by using the Cherenkov detector as a selector of "good" electron events. If N_{total} is the number of the events that triggered the Cherenkov, and N_{cut} the number of events that remain after the shower cuts are applied, then $ID_{eff} = N_{cut}/N_{total}$. We selected the cuts applied so that for all kinematic settings ID_{eff} was bigger than 0.99, and the pion dilution of the data sample can be neglected.

$e-\pi$ Separation in the Hadron-Arm

In contrast to the Electron-Arm, the shower detector of the Hadron-Arm consists of only a preshower, of a geometry similar to the Electron-Arm preshower.

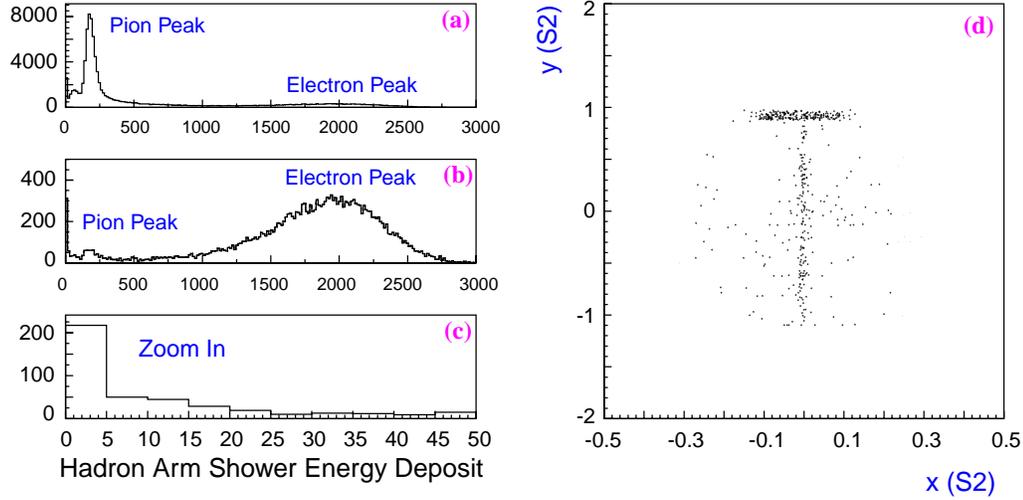


Figure 3.25: (a) Hadron-Arm preshower energy deposition (b) Low energy event coordinates on scintillator S2. The beam energy is $E_{beam}=5058$ MeV and the spectrometer momentum setting $p_0=2046$ MeV.

Therefore, an E/p cut is lacking in this case. In Figure 3.25 we show a typical distribution of the deposited energy in the Hadron-Arm preshower. Figure 3.25(a) is the preshower energy without any cuts, whereas in Figure 3.25(b) a Cherenkov cut has been applied. In this case, one cannot simply apply a cut on the $E_{preshower}$ to separate the electron peak from the suppressed pion peak (Figure 3.25(b), because of the zero-energy peak (shown blown up in Figure 3.25(c), which contains both pions and electrons. This peak contains about 2% of the events, which is not negligible. The origin of this peak is shown in Figure 3.25(d), where we plot the x and y coordinates of the Scintillator 2 (positioned before the preshower) for the events lying under this peak. As one can see, these events correspond to particles crossing the detector at the intersection of the 2 blocks, and at the top, where presumably 2 blocks are dead. Consequently, the selection strategy followed is that all events that trigger the Cherenkov are accepted as "good" electrons, and a dilution due to penetrating pions is calculated by measuring the ratio of events under the suppressed pion peak shown in Figure 3.25(b).

The results of the electron-pion separation for both the Electron- and the Hadron-Arm are tabulated in Appendix A.

Bibliography

- [1] C. Leemann, Jlab Publication CEBAF-PR-88-001
- [2] C.E. Rees , JLAB Publication JLAB-ACO-98-03, 1998
- [3] R.S. Suleiman, Ph.D. Thesis, Kent State University, 1999
- [4] J.E. Clendenin *et al*, SLAC Publication SLAC-PUB-7619, 1997
- [5] C.K. Sinclair, Jlab Publication CEBAF-PR-89-002, 1989
- [6] C.K. Sinclair, Jlab Publication JLAB-ACC-99-11, 1999
- [7] Hall A Experimental Equipment Operations Manual,
<http://hallaweb.jlab.org/document/OPMAN/node24.html>
- [8] P.E. Ulmer, [http : //www.jlab.org/ ~ fissum/e89003/learned.html](http://www.jlab.org/~fissum/e89003/learned.html)
- [9] A. Deur, E-94010 Technical Note, [http : //www.jlab.org/e94010/tech_notes.html](http://www.jlab.org/e94010/tech_notes.html)
- [10] A. Czarnecki, W. Marciano, Phys. Rev. D, **53**, 1066 (1996)
- [11] P. Ulmer *et al*, Physics Requireents on the Determination and Stability of the Parameters of the Beam, Jlab Tech. Note, TN 90-255
- [12] J. Berthot and P. Vernin, Nucl. Phys. News, Vol. 9, 4 (1999)
- [13] O. Ravel, Ph.D. Thesis, Universite Blaise Pascal, DU 951
- [14] CEBAF Conceptual Design Report, 1990
- [15] Liyanage Nilanga, Private Communication
- [16] K.G. Fissum *et al*, Jlab Technical Note, JLAB-TN-00-016

- [17] A. Deur, Ph.D. Thesis, University Blaise Pascal, 2000
- [18] M. Iodice *et al*, Nucl. Instr. and Meth. in Phys. Res. A **411**, 223 (1998)
- [19] A. Deur, Jlab Technical Note, JLAB-TN-98-028
- [20] K. Slifer, [http : //www.jlab.org/e94010/tech_notes.html](http://www.jlab.org/e94010/tech_notes.html)

The Polarized ^3He Target

4.1 Introduction

The polarized ^3He target is based on spin-exchange optical pumping, which involves optical pumping of an alkali metal, such as rubidium, the polarization of which is transferred to ^3He through spin-exchange collisions. The physics of optical pumping dates back to 1950 and has been extensively reviewed by Happer [1]. Optical pumping is a method to produce population imbalances among the ground- or excited-state magnetic sublevels of atoms, using their interaction with light. For the simplified case of nuclear spin $I = 0$, the process of optical pumping the magnetic sublevel $m = 1/2$ of the Rb ground state is depicted in Figure 4.1. Polarized (σ^+) resonance light at 794.8 nm excites the D1 ($5^2S_{1/2} \rightarrow 5^2P_{1/2}$) transition of Rb, preferentially depleting the $m = -1/2$ ground-state Zeeman sublevel, because of angular momentum conservation.

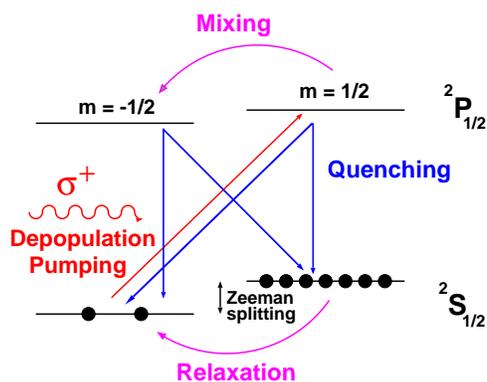


Figure 4.1: Optical pumping of an alkali atom neglecting hyperfine structure.

The admixture of a small amount of N_2 quenches both P-state sublevels, thus reducing polarization losses from radiation trapping. At a magnetic field of 25 Gauss, typical for low field pumping, the thermal ground state polarization for such an atom would be (at room temperature):

$$P_{thermal} \approx \frac{2\mu_B B}{k_B T} \approx 10^{-5}, \quad (4.1)$$

compared to polarizations close to 1 achieved by optical pumping. Since the ground state of this atom has only two levels, it can be described by a $2 \otimes 2$ density matrix ρ , given by [2]

$$\rho = \frac{1}{2} + 2\langle \mathbf{S} \rangle \cdot \mathbf{S}. \quad (4.2)$$

For example, for a fully polarized ground state, with $\langle \mathbf{S} \rangle = \frac{1}{2}\mathbf{z}$, ρ is

$$\rho^{pol} = \begin{pmatrix} 1 & 0 \\ 0 & 0 \end{pmatrix} \quad (4.3)$$

In contrast, for an unpolarized ground state, with $\langle \mathbf{S} \rangle = 0$, ρ is

$$\rho^{unpol} = \begin{pmatrix} 1/2 & 0 \\ 0 & 1/2 \end{pmatrix} \quad (4.4)$$

The squared length $(\rho | \rho)$ of ρ , defined by $(\rho | \rho) \equiv Tr[\rho^\dagger \rho]$ is for the first case $(\rho^{pol} | \rho^{pol})=1$, whereas for the unpolarized case, $(\rho^{unpol} | \rho^{unpol})=1/2$. In general, optical pumping will increase ρ towards ρ^{pol} , and relaxation processes will try to decrease it towards ρ^{unpol} .

4.2 Alkali Metal Optical Pumping

The foregoing can be generalized [3] to the actual case of nonzero nuclear spin (for example, for ^{85}Rb $I = 5/2$), where the hyperfine structure has to be taken into account. The ground-state Hamiltonian in the presence of a static magnetic field $\mathbf{B} = B_z \mathbf{z}$ is :

$$\mathcal{H}_g = A_g \mathbf{I} \cdot \mathbf{S} + g_S \mu_B S_z B_z - \frac{\mu_I}{I} I_z B_z \quad (4.5)$$

The eigenstates of H_g are $|FM\rangle$, where F is the total angular momentum of the state in the limit $B_z \rightarrow 0$, and M the eigenvalue of $F_z = I_z + S_z$ (M is a good quantum number for any B_z). Figure 4.2 displays the eigenvalues of \mathcal{H}_g (for ^{85}Rb) as a function of the applied field, as expressed by the Breit-Rabi formula [4]

$$E(F, M) = -\frac{h\Delta\nu}{2(2I+1)} - g_I \mu_B B M \pm \frac{1}{2} h\Delta\nu \left\{ 1 + \frac{4M}{2I+1} x + x^2 \right\}^{1/2} \quad (4.6)$$

with

$$x = \frac{(g_J + g_I) \mu_B B}{h\Delta\nu} \quad (4.7)$$

and [5] $g_J=2.0023$, $g_I=-0.0003$ and $\Delta\nu=3035.732$ MHz. The $+(-)$ sign corresponds to $F = I + \frac{1}{2}$ ($F = I - \frac{1}{2}$).

The density matrix is now a 12×12 matrix (in general $(4I + 2) \times (4I + 2)$) and it can be written as

$$\rho = \phi + \Theta \cdot \mathbf{S} \quad (4.8)$$

where ϕ and Θ are purely nuclear operators. The time evolution of the density matrix can be attributed to two distinct processes: optical pumping and relaxation. Spin exchange with ^3He is one of the relaxation mechanisms, but it will be considered separately.

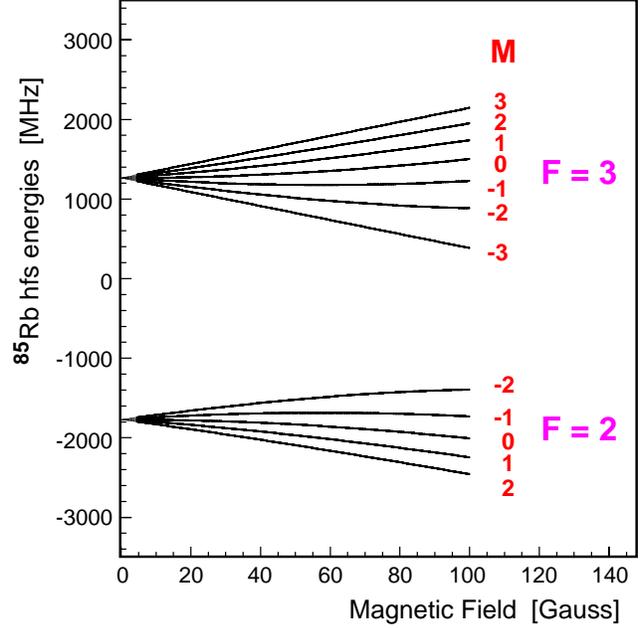


Figure 4.2: Ground state magnetic sublevels of ^{85}Rb .

Optical Pumping

The rate of change of ρ due to optical pumping is given by

$$\frac{d\rho_{op}}{dt} = R[\phi(1 + 2\mathbf{s} \cdot \mathbf{S}) - \rho] + \frac{1}{i\hbar}[\delta\mathcal{E}_{op}, \rho], \quad (4.9)$$

where \mathbf{s} is the photon spin and $\delta\mathcal{E}_{op}$ describes light shifts due to real and virtual transitions [3][6]. The mean pumping rate per unpolarized alkali-metal atom, R , is given by

$$R = \int_0^\infty \Phi(\nu)\sigma(\nu)d\nu, \quad (4.10)$$

where $\Phi(\nu)$ is the photon flux in $\text{sec}^{-1}\text{cm}^{-2}\text{Hz}^{-1}$ and $\sigma(\nu)$ the D1-light absorption cross section for unpolarized atoms. For a laser beam of power $P_{lasers}=90\text{ W}$, radius $r \approx 3\text{ cm}$ and a Gaussian profile centered around $\lambda_0 = \frac{c}{\nu_0}=794.8\text{ nm}$ having a width $\sigma_\lambda \approx 2\text{ nm}$, it is

$$\int_{-\infty}^{+\infty} \Phi(\nu)d\nu = \frac{P_{lasers}}{\pi r^2 h \nu_0} \approx 10^{19}\text{ photons/cm}^2\text{s} \quad (4.11)$$

and

$$\Phi(\nu_0) = \frac{1}{\sqrt{2\pi}\sigma_\nu} \int_{-\infty}^{+\infty} \Phi(\nu)d\nu \approx 5 \times 10^6\text{ photons/cm}^2\text{sHz} \quad (4.12)$$

Furthermore, $\int_{-\infty}^{+\infty} \sigma(\nu)d\nu = \pi r_e c f$, where $r_e = 2.82 \times 10^{-13}\text{ cm}$ is the classical electron radius and the $f=1/3$ is the oscillator strength for D1-light. The absorption cross section $\sigma(\nu)$ has

a Lorentzian shape with a width γ determined by the ^3He density (see section 4.5.3). For $\gamma \approx 200$ GHz, it follows that the cross section at resonance is

$$\sigma(\nu = \nu_0) = \frac{2\pi}{\gamma} \int_{-\infty}^{+\infty} \sigma(\nu) d\nu \approx 3 \times 10^{-14} \text{ cm}^2 \quad (4.13)$$

Under these assumptions, the optical pumping rate turns out to be $R \approx 4 \times 10^4 \text{ s}^{-1}$. With σ^+ (σ^-) light the state being optically pumped is $F = 3, M = 3$ ($F = 3, M = -3$).

Spin Exchange

The spin exchange interaction between the electron spin \mathbf{S} of Rb and the nuclear spin \mathbf{K} of ^3He is a contact interaction of the form $V_{se} = \alpha(R)\mathbf{K} \cdot \mathbf{S}$ where R is the internuclear separation. This interaction brings about a time evolution of the Rb density matrix given by

$$\left(\frac{d\rho}{dt}\right)_{se} = \frac{1}{T_{se}}[\phi(1 + 4\langle\mathbf{K}\rangle \cdot \mathbf{S}) - \rho] + \frac{1}{i\hbar}[\delta\mathcal{E}_{se}, \rho] \quad (4.14)$$

where $\frac{1}{T_{se}} = \kappa_{se}[^3\text{He}]$ is the spin-exchange rate per Rb atom, with $\kappa_{se} \equiv \langle v\sigma_{se} \rangle$ the velocity-averaged spin-exchange cross section, given by [8]

$$\kappa_{se} = (6.7 \pm 0.6) \times 10^{-20} \text{ cm}^3 \text{ s}^{-1} \quad (4.15)$$

The frequency-shift operator, $\delta\mathcal{E}_{se}$, produces a shift in the Rb Zeeman frequencies, proportional to the ^3He polarization. This shift will be used for ^3He polarimetry (see Section 4.6.3). The Rb- ^3He binary collisions result in an effective magnetic field $\delta\mathbf{B}$ experienced by Rb, such that $\delta\mathcal{E}_{se} = \delta\mathbf{B} \cdot (\mu_B g_S \mathbf{S})$. The classical field produced by a polarized ^3He sample of spherical geometry would be $\delta\mathbf{B}_{cl} = \frac{8\pi}{3} \frac{\mu_K}{K} [^3\text{He}] \langle \mathbf{K} \rangle$. Due to the Rb- ^3He binary collisions [11], $\delta\mathbf{B}_{cl}$ is enhanced by a factor κ_0 , so that

$$\delta\mathbf{B} = \kappa_0 \frac{8\pi}{3} \frac{\mu_{He}}{K} [^3\text{He}] \langle \mathbf{K} \rangle \quad (4.16)$$

Other Rb relaxation mechanisms

The Rb spin depolarization rate is given by [8]

$$\gamma_{Rb} = \kappa'_{sd}[\text{Rb}] + \kappa''_{sd}[\text{N}_2] + (\kappa_{sd} + \kappa_{se})[^3\text{He}] \quad (4.17)$$

where

$$\kappa'_{sd} = 4.2 \times 10^{-13} \text{ cm}^3 \text{ s}^{-1} \quad (4.18)$$

$$\kappa_{sd}(T = 450\text{K}) = 2.0 \times 10^{-18} \text{ cm}^3\text{s}^{-1} \quad (4.19)$$

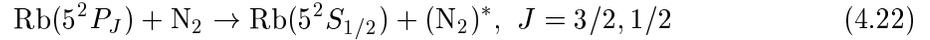
$$\kappa_{sd}'' = 8.0 \times 10^{-18} \text{ cm}^3\text{s}^{-1} \quad (4.20)$$

are the Rb-Rb, Rb- ^3He and Rb- N_2 spin destruction coefficients, respectively, and κ_{se} is given in (4.15). Since $[\text{N}_2] \approx 0.1$ amg, the contribution of the latter is negligible. For usual operating conditions, $[\text{Rb}] \approx 4 \times 10^{14} \text{ cm}^{-3}$, and $[^3\text{He}] \approx 10$ amg. Thus

$$\gamma_{sd} \approx 160_{Rb-Rb} + 560_{Rb-He} = 720 \text{ s}^{-1} \quad (4.21)$$

N_2 quenching

Nitrogen is used as a quenching gas in order to suppress the radiative decay of the Rb excited state, thus preventing Rb depolarization by the unpolarized scattered light.



As described in (4.22), the Rb excitation energy is transferred to translational, vibrational or rotational energy of N_2 . The quenching cross section is [9] $\sigma_q \approx 5 \cdot 10^{-15} \text{ cm}^2$. For a typical nitrogen density of $[\text{N}_2] \approx 0.1$ amg (and using the Rb thermal velocity) the characteristic quenching time is about $\tau_{quench} \approx 2$ ns, much smaller than $\tau_{radiative} = 28$ ns. Even though it is reduced by the presence of N_2 , the Rb relaxation due to radiation trapping is significant. The relaxation rate is [10]

$$\Gamma_{rad. trapping} = fR(1 - P_{Rb}) \quad (4.23)$$

where $f = \gamma_{radiative} / (\gamma_{quench} + \gamma_{radiative})$, and P_{Rb} the average Rb polarization. If the Rb polarization is estimated from (4.27) by using the known spin exchange- and relaxation rates, it is found that $P_{Rb} \approx 0.7$. Thus, from (4.23) it follows that $\Gamma_{rad. trapping} \approx 800 \text{ s}^{-1}$.

4.3 ^3He Polarization Evolution

The density matrix describing the ensemble of ^3He nuclei is

$$\rho_{He} = \frac{1}{2} + 2\langle \mathbf{K} \rangle \cdot \mathbf{K} \quad (4.24)$$

with \mathbf{K} the ^3He nuclear spin. ρ_{He} evolves in time under the influence of the spin exchange hamiltonian, $\alpha\mathbf{K} \cdot \mathbf{S}$, and the hamiltonians describing the nuclear relaxation processes. The

time evolution of $\langle \mathbf{K} \rangle$ due to the former, neglecting the magnetic field shift due to polarized Rb, [3] is

$$\frac{d}{dt}\langle \mathbf{K} \rangle = \gamma_{se}(\langle \mathbf{S} \rangle - \langle \mathbf{K} \rangle) \quad (4.25)$$

where $\gamma_{se} = [\text{Rb}](v\sigma_{se})$. Spin exchange also causes relaxation of the ^3He nuclei. Furthermore, there are three other processes dominating ^3He nuclear relaxation, as described in the following section, their total contribution being represented by Γ . Thus the time evolution of the ^3He polarization evolution is determined by

$$\frac{dP_{He}}{dt} = \gamma_{se}P_{Rb} - (\gamma_{se} + \Gamma)P_{He}. \quad (4.26)$$

The equilibrium ^3He polarization is obviously

$$P_{He}^{\infty} = \frac{\gamma_{se}}{\gamma_{se} + \Gamma}P_{Rb}. \quad (4.27)$$

γ_{se} strongly depends on temperature, and for the operating conditions in this experiment ($T_{pumping} \approx 180 \text{ }^\circ\text{C}$), $\gamma_{se}^{-1} \approx 10 - 12 \text{ h}$.

4.4 ^3He Relaxation Mechanisms

4.4.1 Dipolar and Wall Relaxation

The ^3He - ^3He magnetic dipolar interaction [7] sets a lower bound to the ^3He relaxation rate Γ , namely

$$\Gamma \geq \Gamma_{dipolar} = \frac{[{}^3\text{He}]}{744} \text{ h}^{-1} \quad (4.28)$$

This holds at room temperature, whereas at optical pumping temperatures of about 450 K, $\Gamma_{dipolar}$ is about 5% smaller. Thus for ^3He densities of 10 amagat, $1/\Gamma_{dipolar} \approx 80 \text{ h}$. The other dominant relaxation mechanism is wall relaxation. The average lifetime of the target cells used, T , where

$$1/T = \Gamma_{dipolar} + \Gamma_{wall} \quad (4.29)$$

was about 35 h, which means that Γ_{wall} contributed on the average $1/60 \text{ h}^{-1}$ to the relaxation rate.

4.4.2 Relaxation due to Holding Field Inhomogeneity

The relaxation time due to field inhomogeneities in the holding field is [12]

$$\frac{1}{T_{\nabla B}} = D \frac{|\nabla B_x|^2 + |\nabla B_y|^2}{B_z^2} \quad (4.30)$$

where D is the ^3He self-diffusion coefficient ($\approx 0.2 \text{ cm}^2/\text{s}$). $T_{\nabla B}$ can be estimated by approximating ∇B_x , ∇B_y by $\frac{dB_z}{dz}$, which was measured to be [13], see Section 4.6.1)

$$\frac{dB_z}{dz} = 4.2 \pm 0.5 \text{ mGauss/cm} \quad (4.31)$$

Thus $T_{\nabla B} \approx 10^4 \text{ h}$ and is completely negligible.

4.4.3 Beam Induced Relaxation

When the electron beam is passing through the target cylinder, there is an additional relaxation mechanism caused by beam-induced ^3He ionization. The energy loss of high energy electrons in Helium is characterized by the constant $E' \approx 2\text{MeVcm}^2/\text{g}$. The total energy loss along the target of length L will then be

$$\Delta E = \frac{dE}{dx} L = E' M [^3\text{He}] L \quad (4.32)$$

with $M = M_{^3\text{He}} = 5 \cdot 10^{-24} \text{ g}$. The mean energy expended by an electron for the creation of a $^3\text{He}^+$ ion is [14] $E_0 = 32 \text{ eV}$. So the ionization rate induced by an electron beam of current I (in particles/s) will be

$$\gamma_{ion}^{beam} = I N_{ion}^1 = \frac{I}{E_0} E' M [^3\text{He}] L \quad (4.33)$$

If the beam has an area A_b , then the number of ^3He atoms in the beam path is $N_{He} = [^3\text{He}] A_b L$, so the ionization rate per ^3He atom, Γ_i will be

$$\Gamma_i = \frac{I}{A_b} \frac{1}{E_0} E' M \quad (4.34)$$

The beam-induced relaxation rate of ^3He will thus be $\Gamma_{beam} = n_d \Gamma_i = (n_a + n_m) \Gamma_i$, where n_d is the number of ^3He atoms depolarized for each atom ionized. n_a and n_m represent the contribution to Γ_{beam} due to the atomic ions produced ($^3\text{He}^+$) and the molecular ions formed ($^3\text{He}_2^+$), respectively. Due to the presence of the small quantity of N_2 , the contribution of the latter is completely suppressed [15]. The contact interaction between the unpaired electron of $^3\text{He}^+$ and the ^3He nucleus causes polarization transfer from the latter to the former, a

process that by itself conserves polarization. Charge exchange collisions with other atoms (for example, N_2) or the cell walls bring about the irreversible loss of nuclear polarization. The atomic depolarization number n_a has a value between 0 and 1, depending on the partial pressures of the gases present. Since there is no exact expression for n_a , for the following we will use just the fact that $n_a \leq 1$.

Estimate of Γ_{beam}^{max} under typical conditions

For a beam current of $I=10 \mu\text{A}$ and a beam radius of $r_b = 100 \mu\text{m}$, it follows that the ionization rate in beam, Γ_b , will be $\Gamma_b^{-1} = 16 \text{ s}$. Due to beam rastering, the beam scans a spot of area A_s , and the relaxation rate in that region, Γ_s will be reduced by a factor $\pi r_b^2/A_s$. Taking $r_s = 0.15 \text{ cm}$, we find that $\Gamma_s^{-1} = 1 \text{ h}$. Since the target cell radius is $r_t = 0.8 \text{ cm}$, the volume averaged ionization rate (in the target chamber alone) will be

$$\Gamma_i = \Gamma_s \frac{A_s}{\pi r_t^2} = \frac{1}{28.5\text{h}} \quad (4.35)$$

Thus, since $n_a \leq 1$, the upper limit for the beam-induced relaxation rate will approximately be

$$\Gamma_{beam} \leq \frac{1}{30 \text{ h}} \quad (4.36)$$

The target polarization loss observed (about 20%, relative) is compatible with the above estimate.

The room-temperature (that is, $\Gamma_{dipolar} + \Gamma_{wall}$) lifetimes of the targets used are shown in the following table.

Target Cell	Lifetime [h]
DontWorry	15
Armageddon	40
BeHappy	40
Nepheli	25
Sysiphos	53
Jin	29

4.5 Target Cells

Optical pumping and spin-exchange takes place in specially prepared glass cells, a typical example of which is shown in Figure 4.3. The cell consists of a spherical pumping chamber, a transfer tube, and a long cylinder where electrons scatter off polarized ^3He nuclei.

4.5.1 Cell Construction

The process of cell construction consists of three basic steps, namely glassblowing of the target cell and the glass string to which it is attached, vacuum system bake out, and gas filling.

The glass surface is very critical to the relaxation polarized ^3He , since it is the interaction of the helium nuclear spins with the surface atoms that forms one of the possible nuclear relaxation channels. There has been evidence that surface microfissures enhance the relaxation rate by trapping the helium nuclei at the surface and hence increasing the interaction time between the two. Therefore, the glass tubing used for the construction of the cell body has been "resized", in order to smoothen the glass surface. Resizing is a procedure during which the commercial glass tubing is brought to a melting temperature, at which it is radially expanded.

The string with the target cell is then mounted on the vacuum system, the layout of which is shown in Figure 4.4. It consists of the gas handling system, the pumping system, and the glass string. The pumping system is driven by a diffusion pump (with a liquid nitrogen trap on the inlet), which is backed by a mechanical pump. The lowest achievable pressure, measured by an ion-gauge, is somewhat less than 10^{-8} Torr. The cell is baked out at a temperature of about 480°C for a period of four to five days, in order for the volatile impurities on the glass walls to be pumped away. During that period, Rb from the ampule is chased with a glassblowing torch into the little recess to the left of the retort. Rb is chased into the recess and moved around somewhat in order to evaporate what appears

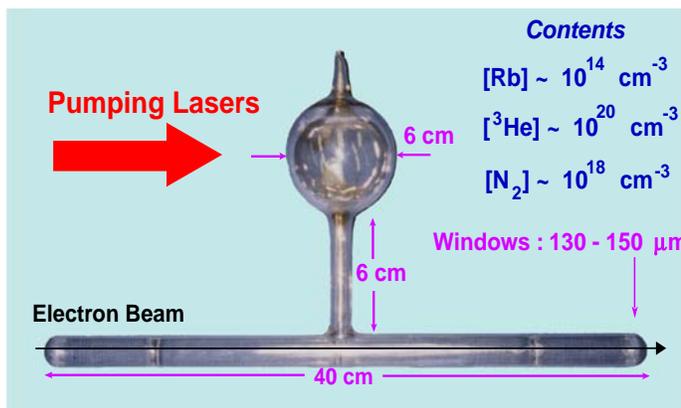


Figure 4.3: Target Cell used at E-94010

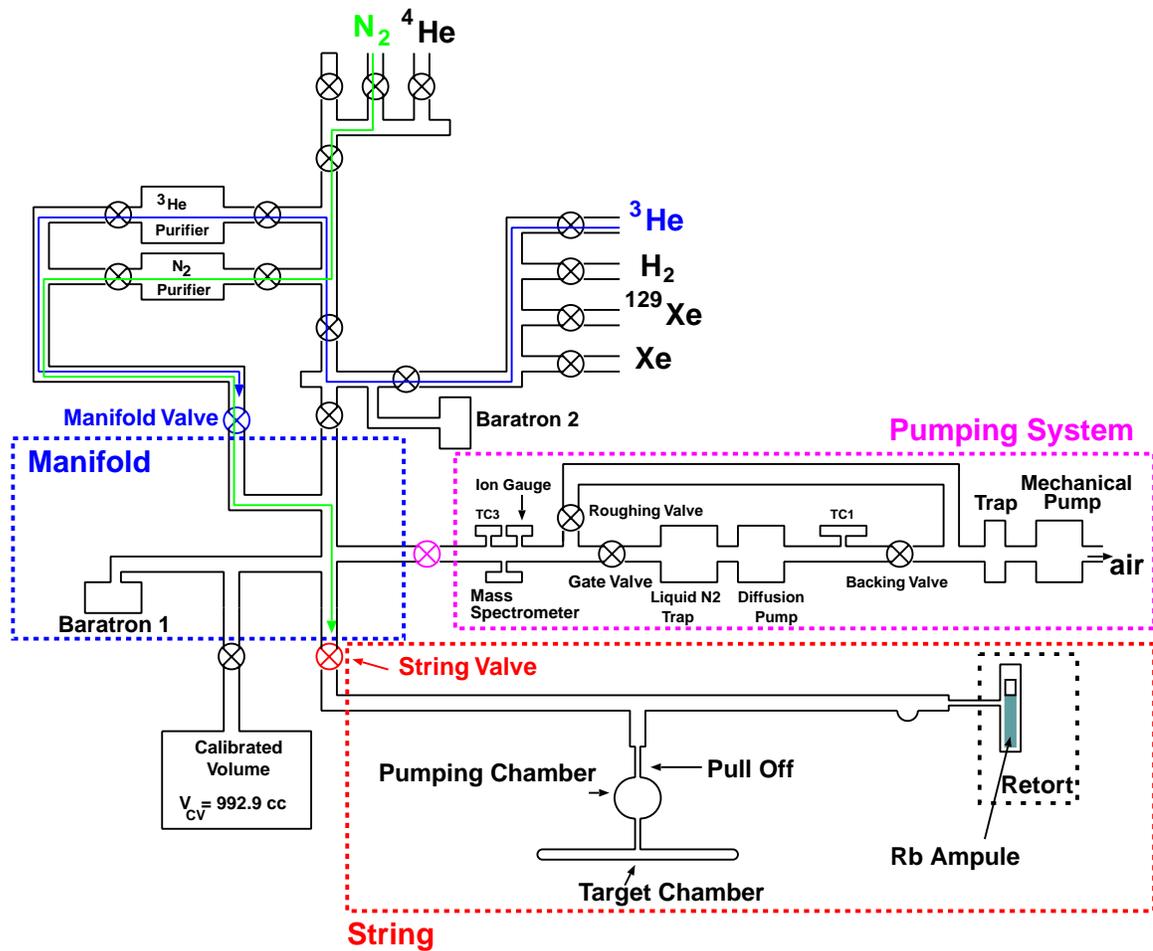


Figure 4.4: Vacuum system Layout and String.

to be the oxidized surface formed by the initial contact of the ampule with the atmosphere. The retort is finally pulled off.

At the end of the bake-out, and before gas filling, the Rb is chased from the recess into the cell. The next step is the nitrogen filling. Nitrogen is flowed through its purifier (green path in Figure 4.4) until the pressure in the string is about 40 torr. The target cylinder of the cell is then cooled down to about 10 K by flowing liquid helium through a dewar that encloses it. The nitrogen accumulates in the cold cylindrical target chamber, and the initial string pressure of about 40 torr is chosen so that the final room temperature N_2 pressure will be the desired 60-70 torr.

The most important effect, though, of the cooling is the fact that the pressure in the string

is always kept below 1 atmosphere. The glass can thus collapse under the atmosphere when the time comes to seal off the cell.

The last step is filling with ^3He . This is a repetitive process, during which a 'fill' volume is charged to a known pressure a number of times. The fill volume consists of the calibrated volume and the manifold volume. By opening the manifold valve, this volume can be charged to a certain pressure (measured by Baratron 1), by flowing helium from the ^3He tank through the helium purifier (blue path in Figure 4.4). By opening the string valve, helium from the fill volume flows into the cold target chamber. This is repeated until the desired average ^3He density in the cell is achieved (9-10 amagats). The cell is finally sealed off using a hand-held torch.

4.5.2 Cell Volumes

The total volume of the cell is needed in order to extract the ^3He density from the vacuum system gas filling data. Moreover, the volumes of the individual parts of the cell, namely the pumping chamber, the transfer tube and the target chamber, are necessary for the calculation of the gas density distribution when a temperature gradient is present. They are also needed in the polarization diffusion model used for the EPR Calibration (see section 4.6.3). There are three ways to measure the cell volume: at the vacuum system, the buoyancy method, and the geometrical measurement using the external cell dimensions. The last two methods measure the outside cell volume, so the glass volume has to be subtracted. The buoyancy method rests on Archimede's principle. A metal block suspended from an accurate scale is submerged in water. If the weight with just the block is W_{block} and the weight with the block and the cell attached to it is $W_{block+cell}$, then the inside cell volume will be :

$$V_{cell} = \frac{W_{block} - W_{block+cell} + m_{cell}}{\rho_{water}} - \frac{m_{cell} - m_{^3He}}{\rho_{glass}} \quad (4.37)$$

The accuracy of the measurement is about 0.5%. An independent check was done using a glass sphere made out of pyrex glass ($\rho_{pyrex} = 2.23 \text{ g/cc}$). By measuring the mass of the sphere when empty and when filled with water, its volume was found to be $303.1 \pm 0.1 \text{ cc}$. The buoyancy method gave $303.0 \pm 1.5 \text{ cc}$, whereas from the vacuum system data it follows that the volume is $298.0 \pm 1.2 \text{ cc}$. In the following, we will use the volumes determined by the buoyancy method. For the individual cell parts we use the volumes measured geometrically

scaled such that their sum equals the total inside volume determined as described previously. These volumes (in cc) are shown in Appendix B.

4.5.3 Cell Densities

There are two independent ways to determine the ^3He density in the target cells. One uses the data from the gas filling procedure during the cell construction. The second is based on absorption spectroscopy on the sealed cell.

Vacuum system density

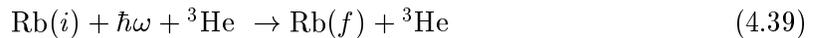
Let $P_j^{initial}$ be the pressure in the fill volume after charging it up for the j -th time, and P_j^{final} the equilibrium pressure after opening the string valve for the j -th time. Let P_{final} be the pressure in the fill and string volume when the string valve is opened after the cell has been pulled off. If N is the number of fill-volume charges, then the number density of ^3He in the cell will be:

$$n_{^3\text{He}} = \frac{1}{k_B T_{fill} V_{cell}} \left[\left(\sum_{j=1}^{N-1} (P_j^{initial} - P_j^{final}) + P_N^{initial} \right) V_{fill} - P_{final} (V_{fill} + V_{string-cell}) \right] \quad (4.38)$$

where T_{fill} and V_{fill} are the temperature and volume of the fill-volume, respectively, and $V_{string-cell}$ is the volume of the string after the cell has been pulled off. As mentioned previously, the fill volume consists of the calibrated volume ($V_c = 993$ cc) and the manifold volume ($V_m = 160$ cc). The uncertainty of the ^3He density depends on the uncertainty of the pressure measurement (negligible, about 0.1%) and the uncertainty of the average temperature of the gas in the fill-volume T_{fill} (1.7%) and the fill-volume itself (0.2%). For one target cell (Nepheli) only the manifold volume was used as the fill volume, making a large number of charges N necessary, and amplifying the final density error.

Pressure Broadening Measurement

The second method to determine the ^3He density relies on the broadening of the absorption lines (D1 and D2) of Rb due to the presence of ^3He , which acts as a high pressure perturber of these lines. One can consider the collision :



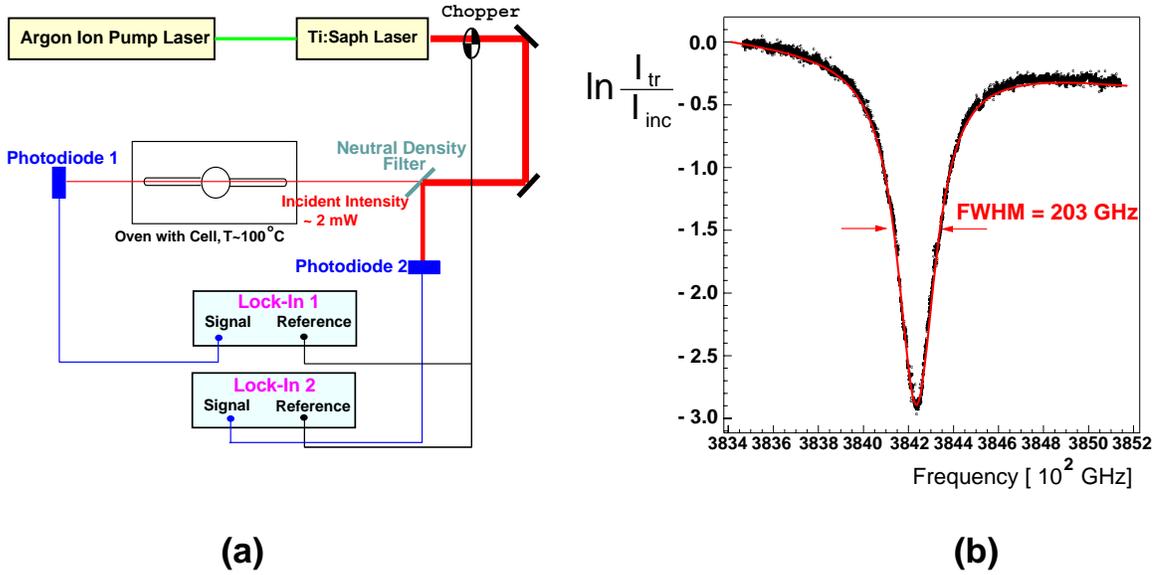


Figure 4.5: (a) Experimental Setup for scanning the D1/D2 Lines. (b) D2 Lineshape data.

to result in a radiating oscillator (Rb) with a varying phase. In the impact approximation [16], i.e. when the collision can be assumed to be instantaneous, the Fourier spectrum of the oscillating amplitude is just a Lorentzian:

$$L(\omega) = \frac{\gamma}{2\pi} \frac{1}{(\omega - \omega_0 - \Delta)^2 + (\gamma/2)^2} \quad (4.40)$$

The actual lineshape has a Voigt profile [22], i.e. it is the convolution of a Gaussian Doppler-broadened line with the Lorentzian collision-broadened line.

The Doppler width is [22] : $\delta f_{Doppler} = 29.23\sqrt{T}$ MHz. At $T=100$ °C , $\delta f_{Doppler}=565$ MHz, which amounts to only 0.3% of the pressure-broadened width. So the convolution integral is indistinguishable from a Lorentzian, and this is the form we used to fit the data.

To the measured width of the absorption lines, there are two contributions : the main one comes from the broadening due to collisions with ^3He .

However, there is a roughly 1% contribution due to N_2 , the density of which is only about 0.1 amg. The relevant proportionality constants, as well as their temperature dependence

	^3He	N_2
D1 full width (GHz/amg)	18.7 ± 0.2	17.8 ± 0.3
D2 full width (GHz/amg)	20.8 ± 0.2	18.1 ± 0.3

Table 4.1: Pressure broadening coefficients.

are known [21], and are reproduced in Table 4.1 . The temperature dependence of these constants ($T^{0.05\pm 0.05}$ for the D1 width and $T^{0.53\pm 0.06}$ for the D2 width) has also been taken into account.

Measurement Technique

As can be seen in Figure 4.5(a), the target cell is placed in an oven heated to about 100 °C. An argon-ion laser pumps a scannable Ti:Sapph laser equipped with an accurate frequency meter. A beam of intensity 2mW is picked-off from the Ti:Sapph beam and sent through the cell onto photodiode 1. Another photodiode (2) is used to monitor the intensity of the incident beam. Both photodiodes provide the input signals for two lock-in amplifiers referenced by the chopper frequency. The logarithm of the ratio of the two lock-in output signals is then fitted to a Lorentzian shape. A typical lineshape is shown in Figure 4.5(b). From the width of the Lorentzian the width due to N_2 collisions is subtracted, and from the remaining width the ^3He density is extracted. The dominant contribution to the final uncertainty is the error in the proportionality constants presented in Table 4.1 (1.6%). The results are shown in Figure 4.6 and included in Appendix C.

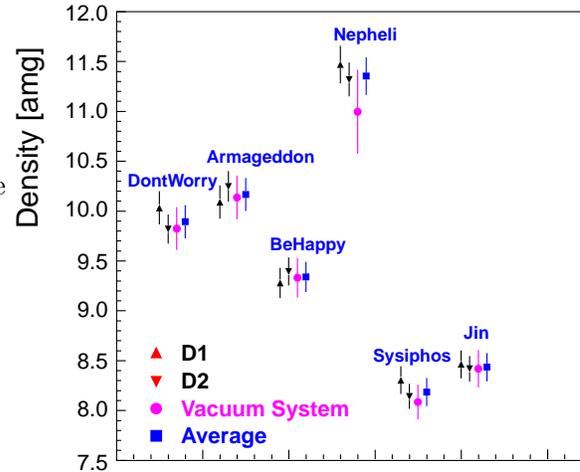


Figure 4.6: Results of ^3He density measurements.

4.5.4 Target Chamber Window Thicknesses

The most accurate method to determine the thickness of a target cell window is the interferometric measurement. It consists of reflecting a laser beam off the inner and the outer surface of the cell windows and observing the interference pattern formed when the reflected beams combine. A schematic setup of the measuring apparatus is depicted in Figure 4.7(a). The beam from a scannable Ti:Sapph laser is reflected on the surface of the window to be

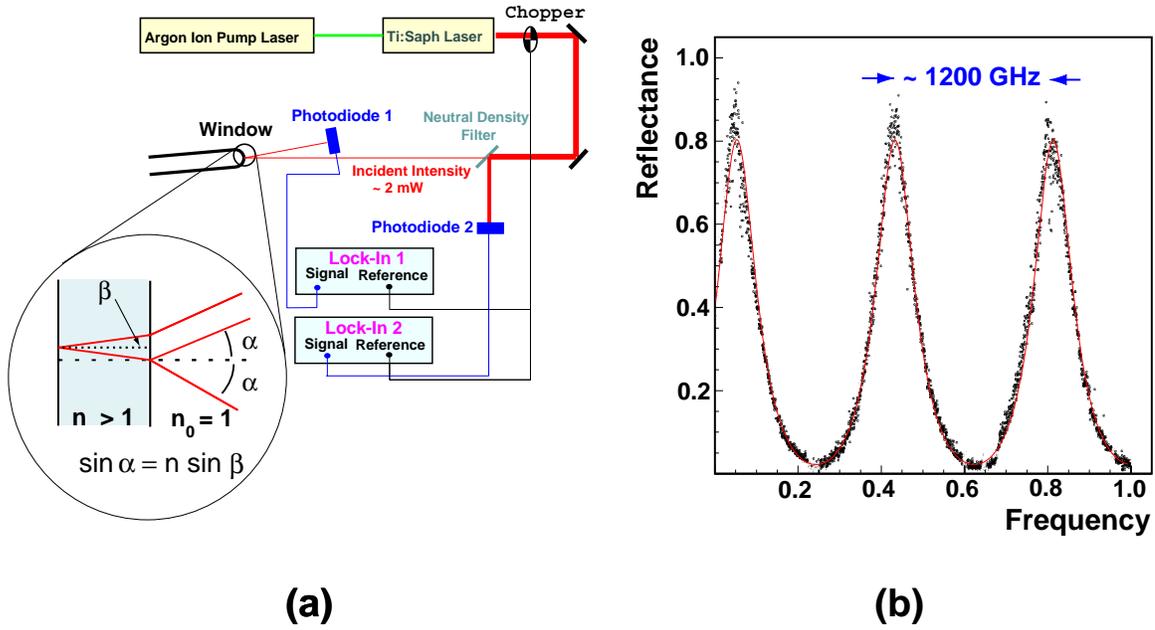


Figure 4.7: (a) Experimental setup for measuring cell window thicknesses. (b) Reflectance data.

measured. If the angle of incidence is α , the index of refraction of the glass n and the angle of refraction β then the reflectance, R , is given by [22]:

$$R = \frac{F \sin^2(\phi/2)}{1 + F \sin^2(\phi/2)} \quad (4.41)$$

where F is the finesse, and

$$\phi = \frac{4\pi f}{c} nd \sqrt{1 - \sin^2 \beta} + \Delta\phi, \quad (4.42)$$

with d the window thickness and f the laser frequency. For an angle of incidence of about 5° , $\sqrt{1 - \sin^2 \beta} \approx 1$ so that

$$\phi/2 = \frac{2\pi f}{c} nd + \Delta\phi. \quad (4.43)$$

By scanning the frequency (we usually scan over 3000 GHz) and fitting the resulting R versus f pattern to the above form, one can very accurately determine the window thickness d . Figure 4.7(b) shows an example of the measured reflectance and the corresponding fit. The abscissa is a normalized frequency, namely $\frac{f-f_0}{f_1-f_0}$, where $[f_0, f_1]$ is the scan interval. Before connecting the windows to the target chamber, we also measured them with a micrometer of $1.3 \mu\text{m}$ resolution. All the thicknesses fall within the range of 120-150 μm , and are shown in the following Table.

Target Cell	Window	Thickness [μm]		Time in beam [days]
		Mechanical	Optical	
DontWorry	2	137.2 ± 1.3	135.9 ± 0.6	16
	21	143.5 ± 1.3	140.1 ± 0.5	
Armageddon	VII	125.7 ± 1.3	121.9 ± 0.6	7
	XVIII	142.2 ± 1.3	139.1 ± 0.7	
BeHappy	4	129.5 ± 1.3	-	12
	5	132.1 ± 1.3	135.3 ± 1.6	
Nepheli			-	6
			-	
Sysiphos	9	152.4 ± 1.3	134.2 ± 1.0	12
	18	132.1 ± 1.3	121.0 ± 1.0	
Jin	14	142.2 ± 1.3	136.1 ± 1.2	23
	15	137.2 ± 1.3	134.8 ± 0.8	

The error in the optical measurement is determined by the fit to equation (4.41), whereas that of the mechanical measurement depends on the resolution of the used micrometer. However, the window thickness traversed by the beam is not known with the accuracy that the above errors suggest, first because of the imperfect alignment of the cell with respect to the beam, and second because the beam covers a spot of about $4 \text{ mm} \times 4 \text{ mm}$ due to rastering.

4.6 ^3He Polarimetry

4.6.1 AFP as Polarization Monitor

The polarization of the ^3He target was monitored about once every 4 hours using the NMR method of Adiabatic Fast Passage (AFP) [25].

The method consists of adiabatically reversing the direction of the ^3He spins. The induced EMF signal in the pick-up coils next to the target cell during this reversal is a measure of the polarization of the ^3He gas. The AFP is performed by sweeping the holding field H_0 through the resonance determined by an RF field of frequency $\nu_{RF}=91$ kHz. The amplitude of the RF field was $2H_1=181.6$ mGauss. H_1 is applied at right angles to H_0 . Figure 4.8 displays the dynamics of AFP in the laboratory- and the rotating-frame. The total magnetic field in the lab-frame is

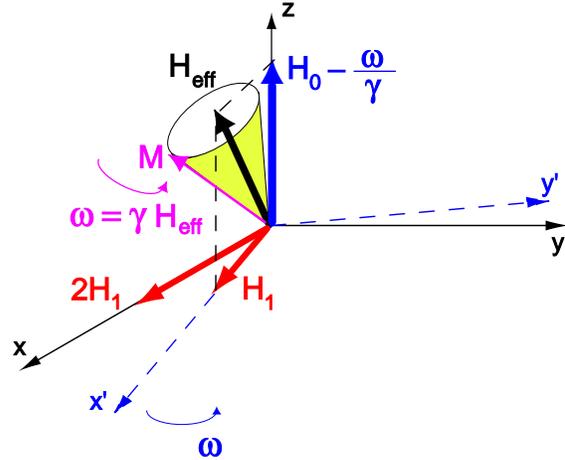


Figure 4.8: Dynamics of AFP

$$\mathbf{H} = \mathbf{z}H_0 + \mathbf{x}2H_1\cos 2\pi\nu_{RF}t. \quad (4.44)$$

In the frame rotating at ν_{RF} [24] the effective field seen by the spins is

$$\mathbf{H}_{eff} = (H_0 - \frac{\nu_{RF}}{\gamma})\mathbf{z} + H_1\mathbf{x}', \quad (4.45)$$

where $\gamma_{He} = 3243$ Hz/Gauss. By sweeping H_0 from $H_{holding}(=25$ Gauss) through resonance $\frac{\nu_{RF}}{\gamma}(=28$ Gauss) to $H_{end}(=32$ Gauss) the effective field \mathbf{H}_{eff} rotates about \mathbf{y}' from $-\mathbf{z}$ through \mathbf{x}' to \mathbf{z} . It can be shown [24] that the magnetization will be precessing about \mathbf{H}_{eff} at an angle θ such that $\tan\theta \approx \frac{H_1}{H_{holding}}$. Since $H_1 = 90.8$ mGauss, $\theta \ll 1$. Consequently the ^3He magnetization will follow \mathbf{H}_{eff} and tip from $-\mathbf{z}$ to \mathbf{z} . Figure 4.9(a) depicts schematically the AFP spin reversal.

The sweep of the holding field H_0 has to satisfy two constraints, in order for the spin-reversal to be efficient, i.e. without polarization losses: the sweep has to be adiabatic, that is, slow enough that the magnetization will always be aligned with the effective field. On

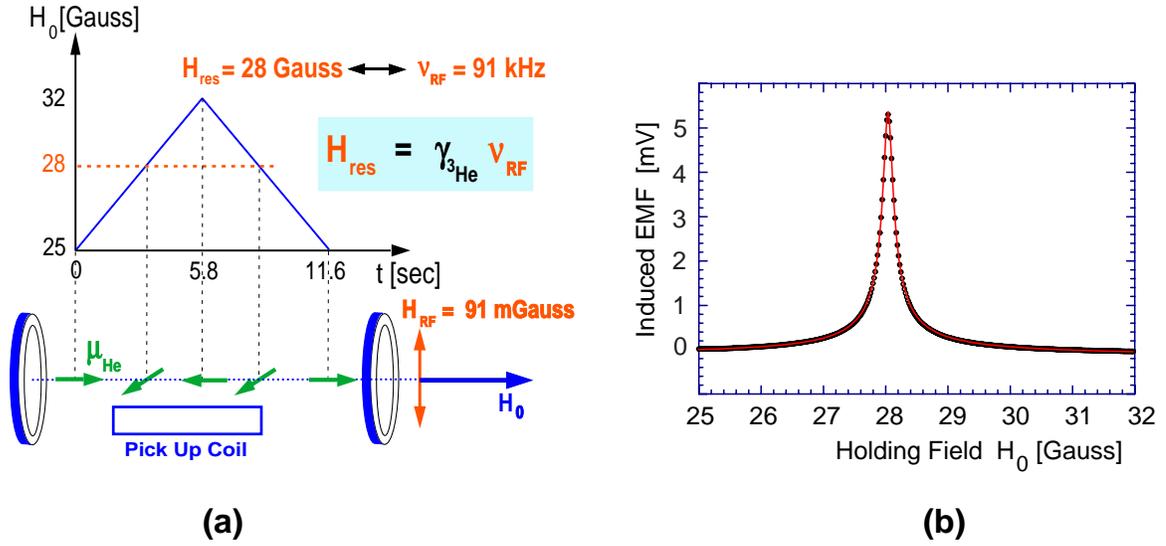


Figure 4.9: (a) Schematic of AFP. (b) Typical ^3He NMR signal.

the other hand, it has to be fast enough that the spins have no time to relax. The slowest precession frequency of the spins about H_{eff} occurs right at resonance, when $H_{\text{eff}} = H_1$. The characteristic precession time is $1/(\gamma H_1)$, whereas the time of passage through resonance is $\tau \approx H_1/\dot{H}_0$. The relaxation rate in the rotating frame is [17]

$$\frac{1}{T_{1r}} = D \frac{|\nabla H_0|^2}{H_1^2} \quad (4.46)$$

The sweep rate \dot{H}_0 should thus satisfy the conditions :

$$\frac{1}{T_{1r}} \ll \frac{\dot{H}_0}{H_1} \ll \gamma H_1 \quad (4.47)$$

Since $T_{1r} \approx 2000$ s and $\gamma H_1 \approx 300$ s $^{-1}$, whereas $\frac{\dot{H}_0}{H_1} \approx 13$ s $^{-1}$, condition (4.47) is easily satisfied.

Transverse RF field H_1

The transverse RF field, H_1 , used during an AFP reversal is provided by a signal generator fed into a power amplifier. The magnitude of H_1 is chosen so that the width of the EMF signal is completely power-broadened. As can be seen in Figure 4.10, the amplitude of the AFP signal is independent of H_1 when in the power-broadening regime. Using the measurement depicted in Figure 4.10, the longitudinal gradient of the holding field $\frac{dB_0}{dz}$ can

be extracted. If $2L(=10\text{ cm})$ is the length of the pick-up coils, and $b_0 = 2L \frac{dB_0}{dz}$, then the amplitude of the AFP signal at a given H_1 is given by

$$S_{max} = \frac{1}{2} \frac{H_1}{b_0} \ln \frac{\sqrt{H_1^2 + b_0^2} + b_0}{\sqrt{H_1^2 + b_0^2} - b_0} \rightarrow 1, \text{ for } H_1 \rightarrow \infty \quad (4.48)$$

By fitting the data to the above functional form, b_0 can be extracted. It was found that $b_0 \approx 42\text{ mGauss}$. We used this value in Section 4.4.2 to estimate the ^3He relaxation due to the field inhomogeneity.

AFP Signal Shape

To the motion of the spins in the rotating frame one has to superimpose the precession around \mathbf{z} with frequency ν_{RF} to fully describe their motion in the lab-frame. It is easily seen that a lock-in amplifier referenced at ν_{RF} can detect the EMF signal that is induced in a pick-up coil placed in the \mathbf{y} direction.

Since the induced signal $S(t)$ is proportional to the transverse magnetization M_T , and $M_T \sim (H_{eff})_T$, the form of $S(t)$ is

$$S(t) \sim M_T \sim (H_{eff})_T = \frac{H_1}{\sqrt{(H_0(t) - \frac{\nu_{RF}}{\gamma})^2 + H_1^2}} \quad (4.49)$$

Thus the functional form of the AFP signal, of which a typical example is shown Figure 4.9(b), is a square root of a Lorentzian. The amplitude of the signal S_{max} is proportional to the ^3He polarization.

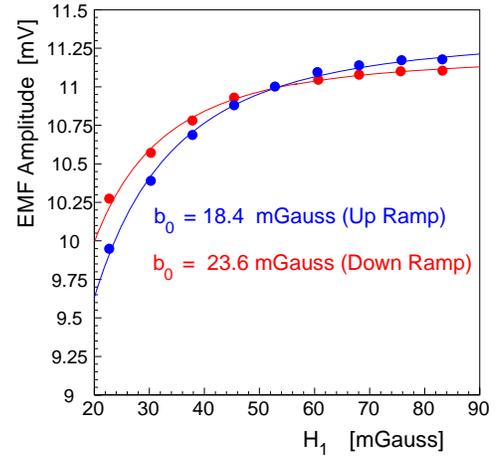


Figure 4.10: AFP signal amplitude as a function of H_1 .

4.6.2 Water Polarimetry

The thermal polarization of protons in water is given by $P_{thermal} = \tanh(\frac{\mu_p B}{k_B T})$. The proton magnetic moment is $\mu_p = 2.793\mu_N$. For a holding field B of 18 Gauss and $T=295$ K, $P_{thermal} \approx 6.23 \times 10^{-9}$. Although very small, this polarization can produce a measurable AFP signal that can be used to calibrate the ^3He -AFP signals.

Since for the protons, $\gamma_p=4.257$ kHz/Gauss, the resonance field for an RF frequency of 91 kHz is $H_{res}=21.27$ Gauss. Therefore the holding field is ramped from 18 to 25 Gauss for the water AFP signals. Figure 4.11 shows the signals obtained during one of the three water calibrations used for our experiment. Fitting the water AFP signals and extracting the polarization corresponding to the signal peak is complicated by the fact that the longitudinal and transverse relaxation times, T_1 and T_2 , are of the same order of magnitude as the sweep time, namely $T_1, T_2 \approx 3$ sec, and the sweep time is $\tau_{sweep}=5.83$ sec. The water signal shape and the corresponding evolution of the polarization have therefore to be extracted from the Bloch equations, which in the rotating reference frame read as follows:

$$\frac{dP_x}{dt} = -\frac{P_x - \chi H_1}{T_2} + \gamma P_y (H_z(t) - H_0) \quad (4.50)$$

$$\frac{dP_y}{dt} = -\frac{P_y}{T_2} - \gamma P_x (H_z(t) - H_0) + \gamma P_z H_1 \quad (4.51)$$

$$\frac{dP_z}{dt} = -\gamma P_y H_1 - \frac{P_z - \chi H_z(t)}{T_1} \quad (4.52)$$

and

$$H_z(t) = H_0 + \alpha t \quad (4.53)$$

where the sweep rate is $\alpha = 1.2$ Gauss/sec and $\chi = \frac{\mu_p}{k_B T} = 3.36 \times 10^{-10}$ Gauss $^{-1}$.

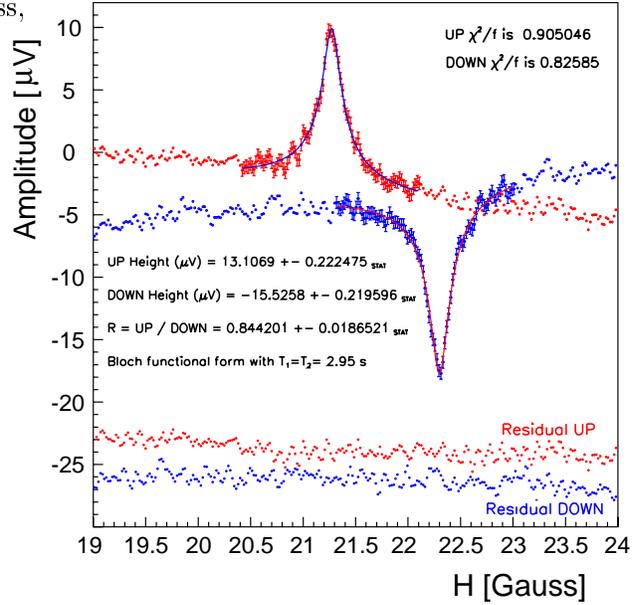


Figure 4.11: Water calibration signals, average of 123 sweeps.

In general there is no analytical solution for equations (4.50)-(4.52), but in the case of $T_1 = T_2$ they can be reduced to one equation for the magnitude of the polarization vector, P_{eff} , where $P_{eff} = \sqrt{P_x^2 + P_y^2 + P_z^2}$, namely

$$\frac{dP_{eff}}{dt} = -\frac{1}{T_1}(P_{eff} - P_{eq}(t)) \quad (4.54)$$

where

$$P_{eq}(t) = \chi \frac{H_1^2 + H_z(H_z - H_0)}{\sqrt{(H_z - H_0)^2 + H_1^2}} \quad (4.55)$$

is the equilibrium polarization that P_{eff} would relax to had it an infinite time. The solution of (4.54) is

$$P_{eff}(t) = e^{-(t-t_0)/T_1} \left(P(t_0) + \frac{1}{T_1} \int_{t_0}^t e^{(t'-t_0)/T_1} P_{eq}(t') dt' \right) \quad (4.56)$$

The signal induced in the pick-up coils is proportional to P_x , where

$$P_x = P_{eff} \frac{(H_{eff})_x}{H_{eff}} = P_{eff} \frac{H_1}{\sqrt{(H_z - H_0)^2 + H_1^2}} \quad (4.57)$$

The first equation in (4.57) tacitly assumes that the polarization vector is aligned with the effective field. Figure 4.12 shows the time-evolution of $P_{eq}(t)$ and $P_{eff}(t)$ obtained by the numerical solution of (4.54). (This is to be contrasted to the helium AFP signal, in which case the limit $T_1, T_2 \rightarrow \infty$ can be used in the Bloch equations (4.50)-(4.52), since $T_1, T_2 \gg \tau_{sweep}$. Then it can easily be shown that $\frac{dP_{eff}}{dt} = 0$).

After expanding the exponential and the denominator of P_{eq} to first order, the form (4.56) of P_{eff} can be used to obtain an approximate analytic solution for fitting the water signal. The error in the fitted signal-amplitude is 1.3%.

We used de-oxygenated, deionized water, the T_1 of which we determined independently, based on the ratio R of the Up- and Down- signal peaks. It was found [18] that $T_1 = 3.0 \pm 0.4$ sec (to be compared with the world value [19] 2.95 sec at 20 °C). T_2 is a function [20] of the RF field H_1 , and for $H_1=90.8$ mGauss we find that [18] $T_2 = 2.7 \pm 0.4$ sec. To

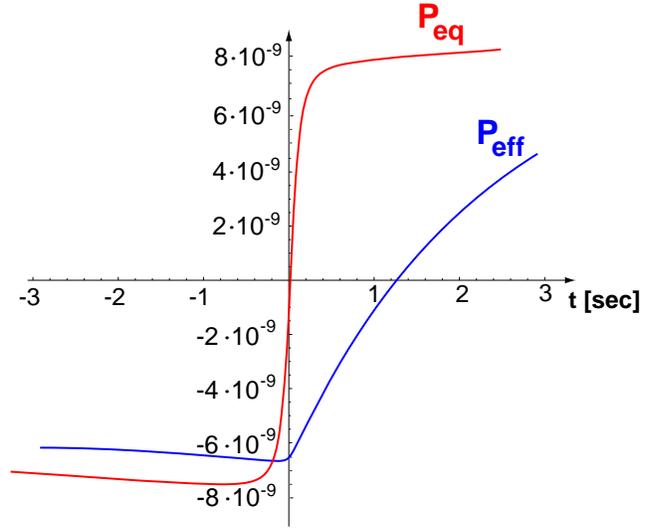


Figure 4.12: Numerical Solution of Equation (4.54).

correct for the fact that $T_1 \neq T_2$ we solve the Bloch equations (4.50)-(4.52) numerically and find that the up- and down- polarizations, P_{up} and P_{down} , that we must associate with the maximum signal heights of the up and down NMR signals have to be corrected by 0.36% and 0.21%, respectively. We thus find that

$$P_{up} = 6.415 \times 10^{-9} \text{ and } P_{down} = 7.655 \times 10^{-9}, \quad (4.58)$$

with the corresponding error of 1.3%.

Corrections

There are several corrections that have to be applied in order to extract a calibration constant k_{water} that characterizes the response of the NMR apparatus.

(i) Flux Correction

The signal measured in the pick-up coils is proportional to the polarization of the medium under consideration, its density and the amount of coupling with the pick-up coils, that is, the flux.

Since the target cells used (either water cells or helium cells) have target cylinders with different radii, the flux produced by them is different and has to be divided out. The flux Φ is defined as

$$\Phi = \oint_{coils} \mathbf{A} \cdot d\mathbf{l} \quad (4.59)$$

where the integration is performed around the pick-up coils, and \mathbf{A} is the vector potential created by the magnetized medium in the cell (for unit magnetization in the z-direction, see Figure 4.13):

$$\mathbf{A}(\mathbf{r}) = \int_{V_{cell}} d^3\mathbf{r}' \frac{\mathbf{z} \times \mathbf{r}}{|\mathbf{r}|^3}. \quad (4.60)$$

The vector potential is calculated by integrating over the volume of the target cell. The transfer tube contributes a negligible amount to the flux, but the pumping chamber reduces the target-cylinder flux by about 10%. The fluxes of different cells can differ by as much as 10%. The error in the flux as a result of the uncertainty of the cell position in the pick-up

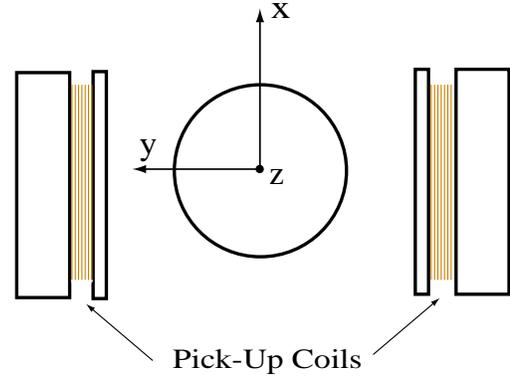


Figure 4.13: Geometry for flux calculation. Only the target cylinder is shown.

coils is found to be 2.1%.

(ii) Q-Curve Correction

The response of the pick-up coils changes slightly with time, one reason being target cell ruptures.

The response was monitored by an excitation coil that produced RF of a given amplitude and varying frequency. The voltage induced in the pick-up coils as a function of frequency is

$$V(f) = A \frac{f}{\sqrt{\frac{1}{Q^2} \frac{f^2}{f_0^2} + (\frac{f^2}{f_0^2} - 1)^2}} \quad (4.61)$$

A, f_0 and Q are obtained from fitting the shape of V vs f with (4.61). The amplitude A depends on geometric factors and the amplitude of the signal that drives the excitation coil. Since the AFP-Signal peak occurs at 91 kHz, the correction factor G_Q is defined as $G_Q = \frac{V(91\text{kHz})}{A \cdot 91\text{kHz}}$. During the experiment G_Q changes by 0.8%, as seen in Figure 4.14.

The corrections mentioned so far are common between the water calibration and the EPR calibration to be described in the following section. It is thus advantageous to define the calibration constant of the NMR apparatus as

$$\kappa = \frac{S[\text{mV}]}{n_t[\text{amg}]P_t[\%]\Phi[\text{cm}^2]G_Q} \quad (4.62)$$

where S is the AFP-Signal peak in mV, n_t the target density in amg ($1 \text{ amg} = 2.688 \times 10^{19} \text{ cm}^{-3}$), P_t the target polarization in %, Φ the flux in cm^2 and G_Q the coil response correction. For the case of water n_t is the proton density, $n_p = 2482 \text{ amg}$, and P_t is given by (4.58).

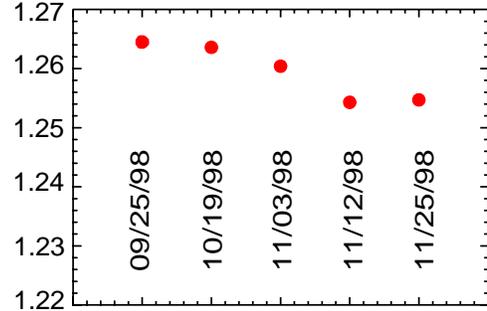


Figure 4.14: Change of G_Q during the experiment

Pertinent to the water calibration are the following two corrections:

(i) Holding Field drift

Since the water signal is an average of a large number of AFP sweeps (100-300), the effect of the drift in the holding field H_0 is of concern. By comparing the resonance position of groups of 50 sweeps, it was found the holding field drifts at a rate $\frac{\delta H_0}{H_0} = 0.001 \text{ h}^{-1}$. In the following table we show [18] the number of sweeps for each of the three water calibrations

done during the experiment, and the correction that has to be applied to the signal peak.

(ii) Target Enclosure

During the experiment the target enclosure was surrounded by an aluminum cover sheet, which was not in place during the water calibrations. It was found that the signal peak

Date	09/25/98	11/03/98	11/25/98
# of sweeps	123	171	213
$C_{\frac{\delta H_0}{H_0}}$	1.0035	1.0156	1.0099

was increased by 1.7% with the aluminum cover in place. Therefore, the water calibration constant has to be corrected by $C_{cover}=0.983$. Finally, one has to multiply by the ratio of magnetic moments $\frac{\mu_{He}}{\mu_p} = 0.762$ and by the ratio of

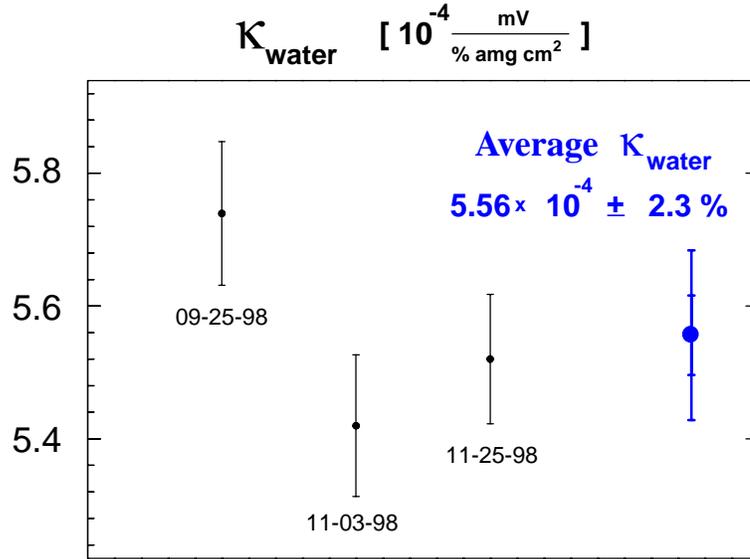


Figure 4.15: Results of the Water Calibration.

pre-amplifier gains used for water and helium signals, namely $\frac{G_{\text{helium}}^{\text{pre}}}{G_{\text{water}}^{\text{pre}}}$ (For the three watercalibrations, $G_{\text{water}}^{\text{pre}}$ was 200, 100 and 1000 respectively, whereas $G_{\text{helium}}^{\text{pre}}$ was always 20). Figure 4.15 shows the three different calibration constants thus obtained and the total average. The final error is dominated by the flux error, the uncertainty in the calculated thermal polarizations corresponding to the signal peak, and the amplitude of that peak.

4.6.3 EPR Polarimetry

The frequency shift $\Delta\nu_{EPR}$ (see 4.14) produced in the Rb EPR frequency of the Zeeman transition ($F=3, M=-3 \rightarrow F=3, M=-2$) due to spin-exchange collisions with ^3He is also a means of polarimetry, since $\Delta\nu_{EPR} \sim \langle K_z \rangle$ and the ^3He polarization is $P_{^3\text{He}} = 2\langle K_z \rangle$. The frequency shift is

$$\Delta\nu_{EPR} = \frac{d\nu_{EPR}}{dB} \delta B \quad (4.63)$$

where δB is given by (4.16).

$\frac{d\nu_{EPR}}{dB}$ can be calculated from (4.6) to be (at 25 Gauss)

$$\frac{d\nu_{EPR}}{dB} \Big|_{M=-3 \rightarrow M=-2} = 485.82 \frac{\text{kHz}}{\text{Gauss}} \quad (4.64)$$

κ_0 is temperature dependent and has been accurately measured [26] :

$$\kappa_0 = 4.52 + 0.00934 T [^\circ\text{C}] \quad (4.65)$$

The actual EPR frequency of Rb will be

$$\nu_{EPR} = \nu_0 \pm \Delta\nu_{EPR} \quad (4.66)$$

where ν_0 is the baseline EPR frequency at the holding field of 25 Gauss. The \pm sign corresponds to the case that the holding field B and the ^3He magnetic moment are aligned (antialigned). By reversing the ^3He spins, $P_{^3\text{He}}$ can be cleanly extracted from (4.66).

EPR Experimental Setup

The experimental setup used for measuring ν_{EPR} is shown in Figure 4.16. The principle of the measurement is the following: frequency modulated RF is applied to the EPR coil from the Voltage-Controlled-Oscillator (VCO), causing transitions from the $M=-3$ to the $M=-2$ Zeeman sublevels of Rb, thereby increasing D1-light absorption. Due to the frequency modulation, the scattered light intensity is thus proportional to the derivative of the Zeeman transition lineshape, and at resonance it is zero.

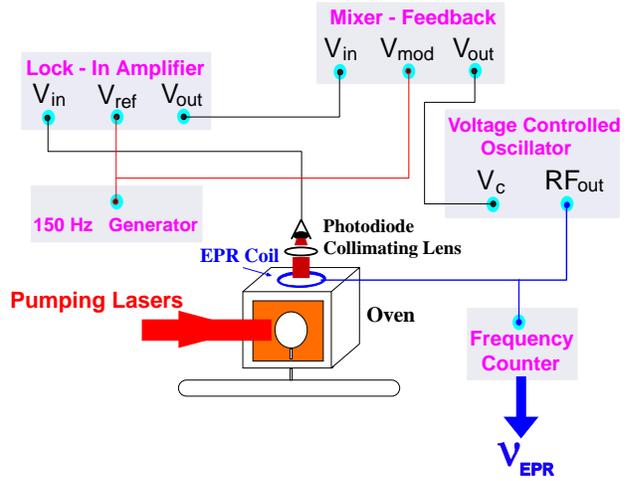


Figure 4.16: Setup for measuring ν_{EPR} .

In order to suppress the dominant D1 component of the scattered light, a D2 filter is used before the photodiode, and the D2 scattered light intensity is observed. The photodiode signal has a component varying with the modulation frequency, and is easily picked-up by the lock-in amplifier referenced to the same frequency. The output of the lock-in is used to drive a feedback circuit that keeps the VCO locked at the Zeeman resonance, which is read by a

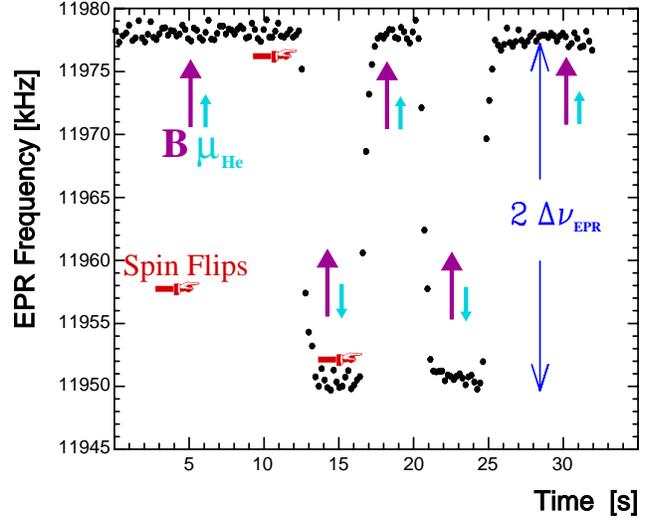


Figure 4.17: EPR calibration data.

frequency counter. This measurement is performed when the ^3He magnetic moment is parallel to the holding field H_0 . Then the ^3He spins are reversed by AFP (this time sweeping the RF frequency, since the holding field has to be constant), and the measurement is performed again. A typical data-set is shown in Figure 4.17.

Polarization Diffusion

The polarization extracted from the EPR data is the polarization of the ^3He gas in the spherical pumping chamber. Since only this part of the cell is being optically pumped, a polarization gradient will develop along the z -direction, as defined in Figure 4.18. It is necessary to calculate the polarization gradient dP/dz , in order to extract the ^3He polarization in the target cylinder. Let P_p (P_t) be the volume averaged, time dependent polarization of the pumping (target) chamber and L_{tr} the length of the transfer tube. We assume that at $z=L_{tr}/2$ ($z=-L_{tr}/2$) $P = P_p$ ($P = P_t$), that is we ignore any gradient in the pumping and target chambers. Let ρ^+ (ρ^-) be the probability of finding a ^3He atom in the spin up (down) state. Then

$$\rho^+ + \rho^- = 1 \quad (4.67)$$

$$\rho^+ - \rho^- = P \quad (4.68)$$

$$\frac{d\rho^+}{dz} = \frac{1}{2} \frac{dP}{dz} \quad (4.69)$$

A polarization gradient along the transfer tube will result in a current

$$J^+(z) = n(z)D(z)\frac{d\rho^+}{dz} = \frac{1}{2}n(z)D(z)\frac{dP}{dz}, \quad (4.70)$$

where $n(z)$ is the ^3He density and $D(z)$ is the diffusion coefficient. Both are a function of z because of the temperature gradient along z .

$$D(z) = D(T_0)\frac{n_0}{n(z)}\left(\frac{T(z)}{T_0}\right)^{m-1} \quad (4.71)$$

with $D(T_0)=2.76 \text{ cm}^2/\text{s}$, at 80°C and 1 atm (where $n_0=0.773 \text{ amg}$), and $m=1.7$. The temperature along the transfer tube will be

$$T(z) = T_t + \frac{T_p - T_t}{L}(z + L/2) \quad (4.72)$$

Taking into account the fact that $J^+(z) = \text{const} = J$, we can integrate dP/dz in (4.70) from $-L/2$ to $L/2$ and get

$$J = \frac{1}{2}D_t\frac{n_t}{L}K(P_p - P_t) \quad (4.73)$$

where $D_t = D(z = -L/2)$ and $n_t = n(z = -L/2)$

and

$$K = (2 - m)\frac{1 - \frac{T_p}{T_t}}{1 - \left(\frac{T_p}{T_t}\right)^{2-m}} \quad (4.74)$$

Thus the rate of change of polarizations will be :

$$\frac{dP_p}{dt} = -\frac{2J}{n_p V_p} A_{tr} \quad (4.75)$$

and

$$\frac{dP_t}{dt} = \frac{2J}{n_t V_t} A_{tr}, \quad (4.76)$$

where A_{tr} is the cross sectional area of the transfer tube. So the rate equations describing polarization diffusion can be written as

$$\frac{dP_p}{dt} = -G_p(P_p - P_t) \quad (4.77)$$

$$\frac{dP_t}{dt} = -G_t(P_t - P_p) \quad (4.78)$$

with

$$G_p = \frac{A_{tr}}{V_p L} \frac{n_t}{n_p} D_t K \quad (4.79)$$

$$G_t = \frac{A_{tr}}{V_t L} D_t K \quad (4.80)$$

Both G_p and G_t are of the order of 1 h^{-1} .

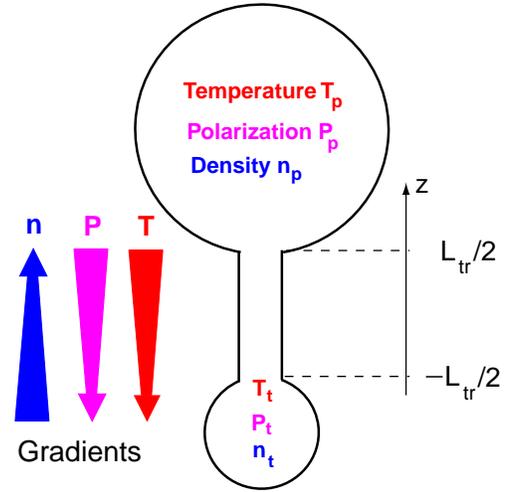


Figure 4.18: Target cell cross section with the directions of temperature, density and polarization gradients.

Complete Rate Equations and steady state

To complete the rate equations, we have to take into account polarization generation and relaxation. In the pumping cell, the rate of increase of polarization due to spin exchange with polarized Rb will be $\gamma_{SE}P_{Rb}$. The polarization also relaxes due to the same mechanism. The relaxation rate due to all other mechanisms is denoted by Γ_p . So,

$$\frac{dP_p}{dt} = -G_p(P_p - P_t) + \gamma_{SE}P_{Rb} - (\gamma_{SE} + \Gamma_p)P_p. \quad (4.81)$$

Similarly,

$$\frac{dP_t}{dt} = -G_t(P_t - P_p) - \Gamma_t P_t. \quad (4.82)$$

Γ_t is in general different from Γ_p , because in the target cell there is the additional mechanism of beam induced relaxation. The EPR calibrations were never performed with the target in beam, so for this case $\Gamma_t = \Gamma_p$. If P_p^∞ and P_t^∞ are the saturation polarizations ($\frac{dP_p}{dz} = \frac{dP_t}{dz} = 0$) of the pumping and target cell, respectively, it follows that

$$P_p^\infty = \frac{\gamma_{SE}}{G_p + \gamma_{SE} + \Gamma_p - \frac{G_p G_t}{\Gamma_t + G_t}} P_{Rb} \quad (4.83)$$

$$P_t^\infty = \frac{G_t}{\Gamma_t + G_t} P_p^\infty \quad (4.84)$$

The solution of (4.81) and (4.82) will then have the form:

$$P_{p,t}(t) = A_{p,t}^{(s)} e^{-\gamma_{slow} t} + A_{p,t}^{(f)} e^{-\gamma_{fast} t} + P_{p,t}^\infty \quad (4.85)$$

with

$$\gamma_{slow} = \frac{1}{2} [G_t + G_p + \Gamma_t + \Gamma_p + \gamma_{SE} \pm \sqrt{(G_t - G_p + \Gamma_t - \Gamma_p - \gamma_{SE})^2 + 4G_p G_t}] \quad (4.86)$$

At time t such that $\gamma_{fast} t \gg 1$ (which is the case since $\gamma_{fast} \approx 3\text{h}^{-1}$) we can omit the second term, and get a relation between P_t and P_p of the form:

$$P_t = \alpha_1 P_p + \alpha_2 \quad (4.87)$$

with

$$\alpha_1 = \frac{\gamma_{fast} P_t^\infty}{\gamma_{fast} P_p^\infty - \gamma_{SE} P_{Rb}} \quad (4.88)$$

$$\alpha_2 = P_t^\infty \left(1 - \frac{\gamma_{fast} P_p^\infty}{\gamma_{fast} P_p^\infty - \gamma_{SE} P_{Rb}} \right). \quad (4.89)$$

This was the case for EPR calibrations performed after the target had been in steady state for several hours. For sequential EPR calibrations for which the condition of the target changed after the first calibration we use equations (4.81) and (4.82) to calculate the target polarization with the appropriate initial conditions.

Temperature and ^3He Density Distributions

In order to calculate the densities n_t and n_p , we need to know the temperature distribution in the target. Figure 4.19 shows the points on the target cells where the temperature was monitored with seven affixed RTD's. The pumping chamber was at a nominal temperature of about 190 °C and the target cylinder at 50 °C at points 1 and 5, and up to 70 °C at point 3.

The temperature of the pumping chamber is actually higher than the value measured by either RTD6 or RTD7, the reason being the heat deposited by the pumping lasers. We estimated the difference, Δ , of the actual pumping chamber temperature from the average $\frac{1}{2}(T_6 + T_7)$. Since the NMR signal is proportional to the ^3He density in the target, the effect of turning the lasers on or off will be to redistribute the gas in the pumping and target chambers, thus changing the NMR signal. It was found [18] that $\Delta = 34 \pm 18^\circ\text{C}$, when using three pumping lasers delivering 90W to the pumping chamber. Thus

$$T_p = \frac{1}{2}(T_6 + T_7) + \Delta \quad (4.90)$$

A completely independent estimate of Δ was made by Walter, Griffith and Happer [27] by studying the energy transport in high density optical pumping cells using Raman scattering.

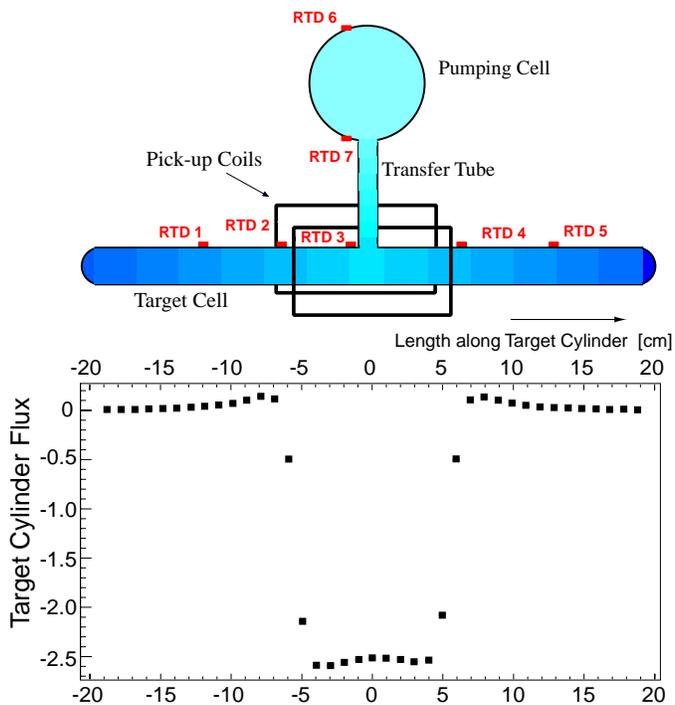


Figure 4.19: Target cell temperature measurements. The color gradient illustrates the ^3He density distribution.

A cell made out of Pyrex glass, having the same geometry as the cells used in this experiment, was optically pumped with varying laser power at the Rb D1 line. A 6-W probe beam from an argon-ion laser (the 5145-Å line) provided the primary Raman beam. It was passed vertically through the cell and imaged onto a double Raman spectrometer. Figure 4.20 shows the photon counts obtained by a PMT at the exit slit of the spectrometer as a function of wavelength. The signal-to-noise ratio is limited by the amount of nitrogen present in the cell (about 60 torr). For 40 W of absorbed pumping laser power, it was found that $\Delta = 58 \pm 25$ °C. This number represents the peak temperature in the cell, and the volume-averaged temperature is expected to be about 20% lower. Within their large errors, both estimates are compatible. We therefore assign a 5% error in the knowledge of the pumping chamber temperature

In the transfer tube and in the target cylinder we linearly interpolate the temperature between the points where it is measured. We can thus calculate the ^3He density along the target cylinder $n_t(x)$. To calculate the EPR calibration constant, κ_{EPR} , we will need the average density between the pick-up coils, namely $n_c = \int_{-l_c/2}^{l_c/2} n_t(x) dx$, where $l_c=10$ cm is the length of the pick-up coils. One has also to consider the flux created by the pumping and target chambers separately, since the gas densities are different. As can be seen in Figure 4.19, the flux created by the target chamber is constant

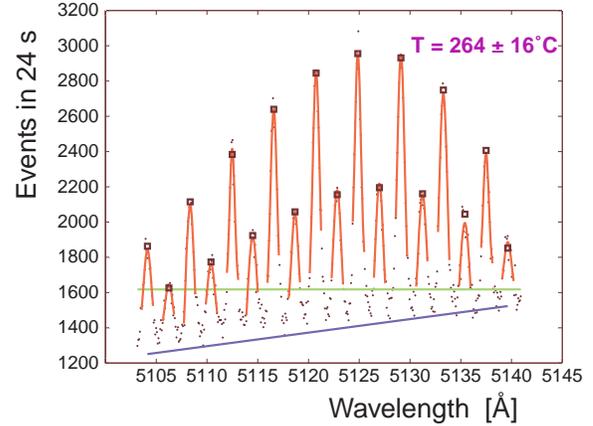


Figure 4.20: Raman spectrum for pyrex cell containing 8.4 amg ^3He and about 60 torr N_2 .

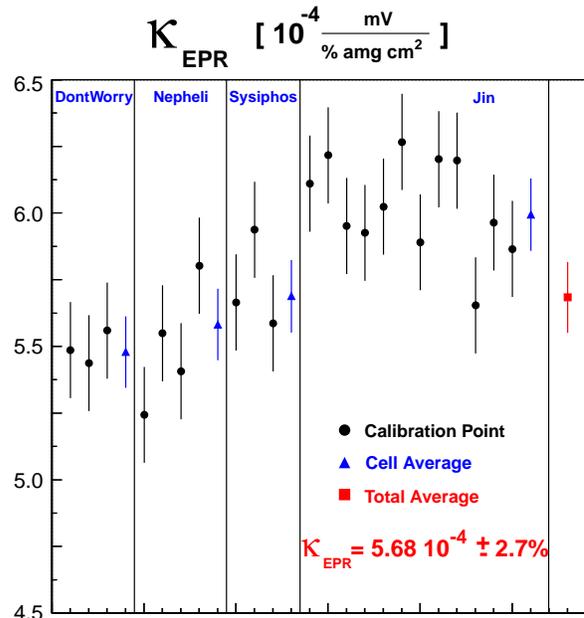


Figure 4.21: EPR Calibration Constants.

along the pick-up coils, and the contribution of the rest of the cylinder is very small. Thus the calibration constant will be

$$\kappa_{EPR} = \frac{S}{P_t n_c (\Phi_t + \frac{n_p}{n_c} \Phi_p) G_Q} \quad (4.91)$$

where Φ_t and Φ_p are the calculated fluxes induced by the target and pumping chambers, respectively. The target polarization calculated by (4.85) is P_t , S is the NMR signal in mV and G_Q the Q-curve gain correction.

Figure 4.21 shows the calibration constants for all EPR calibrations performed during the experiment, as well as their total average. The error is dominated by the error in the flux (2%) and the error in κ_0 . The value of κ_0 given in equation (4.65) holds for a spherical sample. The pumping chamber is not exactly spherical, and furthermore, we have to take into account the contribution of the long-range field created by the transfer tube and the target chamber magnetization. It can be shown [28] that these effects can be taken into account by modifying κ_0 to

$$\kappa'_0 = \kappa_0 - \left(\frac{3}{8\pi} \frac{\partial \phi_{geom}}{\partial y} - \frac{1}{2} \right), \quad (4.92)$$

where \mathbf{y} is the unit vector along the direction of the ^3He magnetization $\mathbf{M}_{^3\text{He}}$ and $\mathbf{H}_{geom} = -\frac{\partial \phi_{geom}}{\partial y} \mathbf{y}$ is the long-range field due to the non-sphericity of the pumping chamber and the ^3He magnetization in the rest of the cell. It is found that this modification decreases κ_0 by only 0.3%. We thus change the error of κ_0 of 1.5% [26] to 1.8%. An error of 1% is finally added due to the uncertainty in the ^3He density distribution between the pick-up coils, resulting from the imperfect knowledge of the temperature distribution (a linear dependence along the target cell has been assumed). The comparison of EPR and Water calibration is shown in Figure 4.22. The ^3He target polarization history during the entire

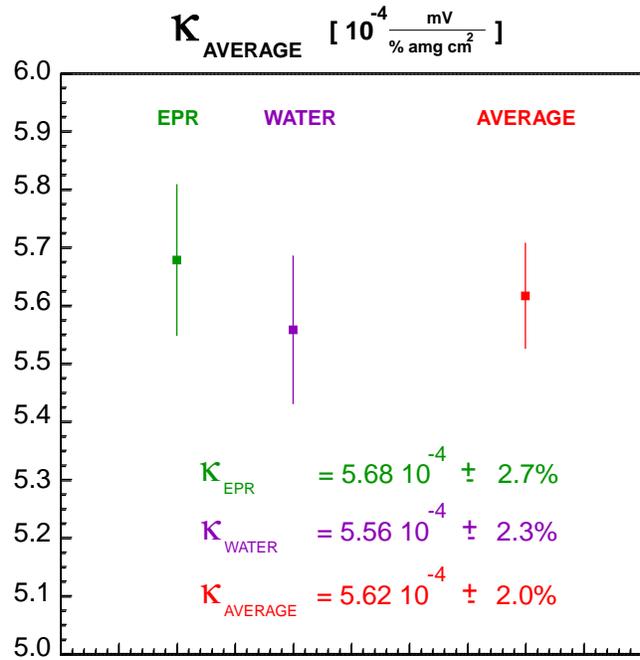


Figure 4.22: Comparison of Water and EPR calibration

experiment is shown in Figure 4.23. It is extracted using the average calibration constant $\kappa_{average}$,

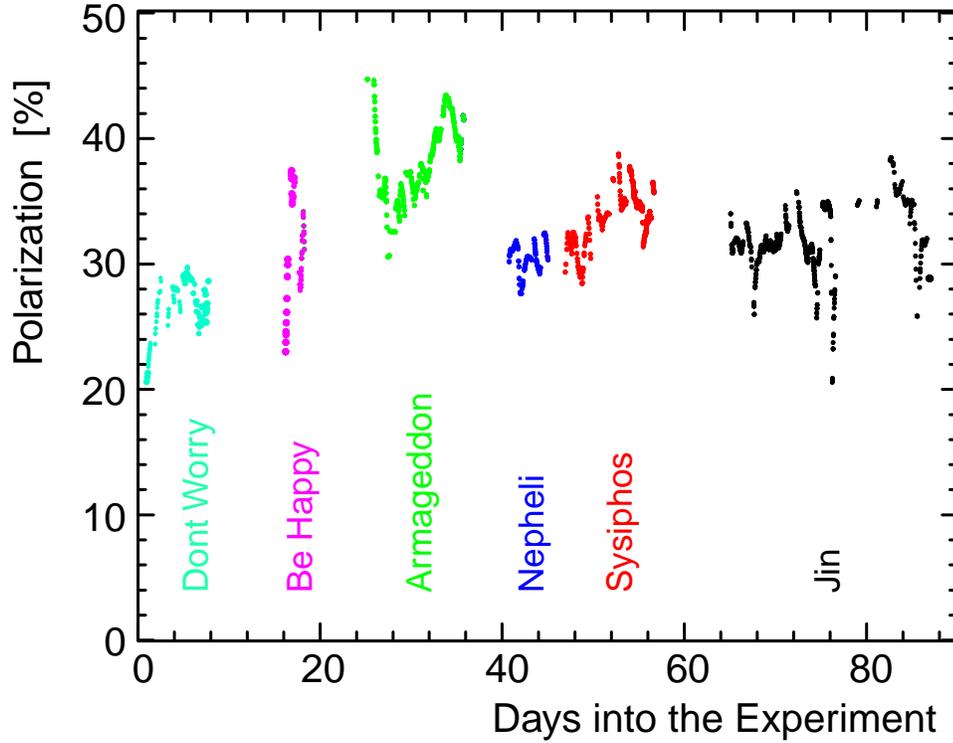


Figure 4.23: ^3He polarization during E-94010

the NMR signal S , the target density in the between the pick-up coils n_t , the flux factor $\Phi \equiv \Phi_t + \frac{n_p}{n_c} \Phi_p$, and the Q-curve factor G_Q :

$$P_t = \frac{S}{\kappa_{average} n_t \Phi G_Q} \quad (4.93)$$

The uncertainty of the polarization stemming from the above quantities is 4.3%. However, as is detailed in the next chapter, the difference of polarized cross sections depends on the product $P_t n_t$, the error of which is determined by the errors of $\kappa_{average}$ and the flux factor only, resulting in an error affecting the physics results of 3%.

Bibliography

- [1] W.Happer, Rev. Mod. Phys. **44**, 169 (1972)
- [2] W. Happer and W.A. Van Wijngaarden, Hyperfine Interactions **38**, 435 (1987)
- [3] S.Appelt *et al*, Phys. Rev. A **58**, 1412 (1998)
- [4] Woodgate, *Elementary Atomic Structure*, Oxford University Press
- [5] E. Arimondo, M. Inguscio and P. Violino, Rev. Mod. Phys. **49**, 31 (1977)
- [6] W. Happer, *Optical Pumping Theory*, Summer Institute of Theoretical Physics, University of Colorado, Boulder, Colorado 1968
- [7] N.R. Newbury *et al*, Phys. Rev. A **48**, 4411 (1993)
- [8] A. Ben-Amar Baranga *et al*, Phys. Rev. Lett. **80**, 2801 (1998)
- [9] E.S. Hrycyshyn and L. Krause, Can. J. Phys. **48**, 2761 (1970)
- [10] D.K. Walter, Private Communication
- [11] S.R. Schaefer *et al*, Phys. Rev. A **39**, 5613 (1989)
- [12] G.D. Cates, S.R. Schaefer and W. Happer, Phys. Rev. A **37**, 2877 (1988)
- [13] S. Incerti, http://www.jlab.org/e94010/tech_notes.html
- [14] K.D. Bonin, D.P. Saltzberg and W. Happer, Phys. Rev. A **38**, 4481 (1988)
- [15] K.P. Coulter *et al*, Nucl. Inst. and Meth. in Phys. Res. **A276**, 29 (1989)
- [16] J.Szudy, W.E.Baylis, Profiles of line wings and rainbow satellites associated with optical and radiative collisions, Phys. Rep. **266** (1996).

- [17] G.D. Cates *et al*, Phys. Rev. A **38**, 5092 (1988)
- [18] J.J. Jensen, Ph.D. Thesis, California Institute of Technology, 2000
- [19] J. Simpson and H. Carr, Phys. rev. **111**, 1201 (1956)
- [20] S. Meibom, Journal of Chem. Phys. **34**, 375 (1961)
- [21] M.V.Romalis, E.Miron, G.D.Cates, Phys. Rev. A **58** 3004 (1998)
- [22] W.Demtröder, Laser Spectroscopy, Springer Verlag 1995.
- [23] M.V. Romalis, Ph.D. Thesis, Princeton University, 1997
- [24] C.P. Slichter *Principles of Magnetic Resonance*, Springer Verlag, 1996
- [25] A. Abragam, *Principles of Nuclear Magnetism* (Oxford University Press, Oxford 1961)
- [26] M.V. Romalis and G.D. Cates, Phys. Rev. A **58**, 3004 (1998)
- [27] D.K. Walter, W.M. Griffith and W. Happer, submitted to Phys. Rev. Lett.
- [28] A.S. Barton *et al*, Phys. Rev. A **49**, 2776 (1994)

Data Analysis and Results

5.1 Data Acquisition and Replay

The E-94010 data were acquired using the CODA environment, developed by the TJNAF Data Acquisition Group. The data were first written to a local disk and then transferred to the Mass Storage System (MSS). The size of the data acquired during the three-month running period was about 5 TBytes. The CODA data file starts with the header, containing information on the event type, event size and run number. The rest of the file contains the physics event data, and the special event data. The latter are the scaler readouts and EPICS data. Scalers count raw detector hits and the number of accepted triggers. They are monitored online and every 10 sec they are fed into the datastream. EPICS data contain information on the status of the experimental equipment (such as magnet currents, high voltages, etc). In the offline analysis the CODA datafile provides the main input of the Hall A event analyzer program, ESPACE (the other input being a database file containing detector calibration constants, physical positions, etc). ESPACE then calculates the focal plane quantities characterizing each detected electron (see Section 5.3). Using the optics database, these quantities can be traced back to the target in order to obtain the interaction point physics variables. The output of ESPACE is in the form of ntuples (the most common data structure in the analysis program PAW), from which the physics observables can be extracted. The reduction of the size of the raw data after going through ESPACE is about a factor of 10.

5.2 Extraction of Polarized Cross Sections from the Data

The primary experimental observable derived from the data are polarized cross sections, defined by

$$\left\langle \frac{d^3\sigma^\pm}{dE' d\Omega} \right\rangle = \frac{1}{P_t P_{beam}} \frac{N_e^\pm(E', \phi, \theta)}{n_t \Delta E' \Delta \Omega (Q^\pm/e)} \quad (5.1)$$

where N_e^\pm and Q^\pm are the number of scattered electrons detected and incident charge during

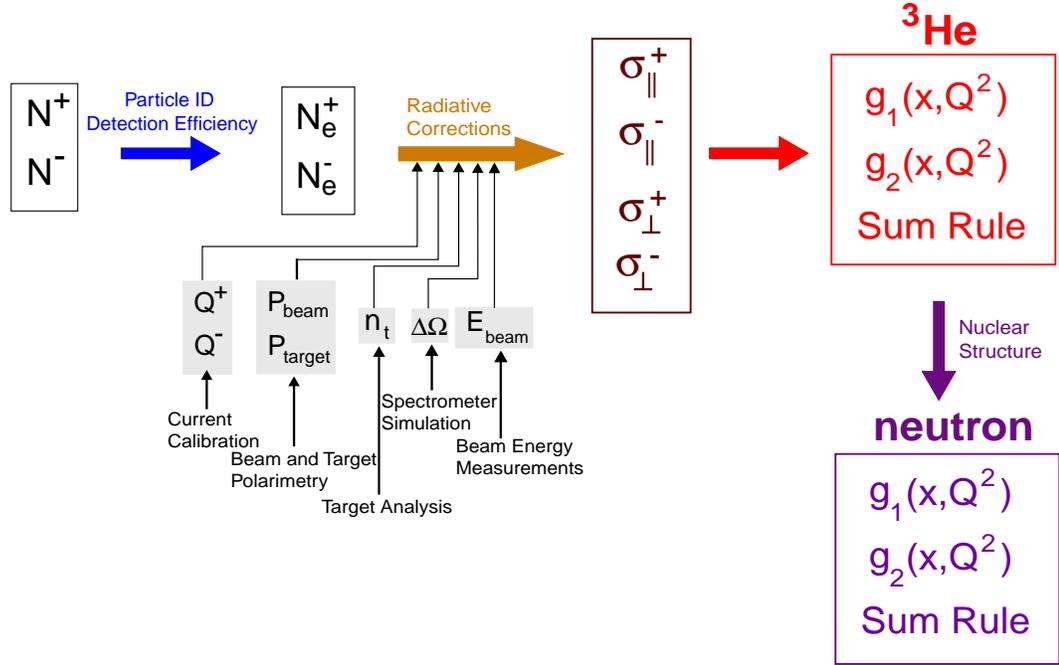


Figure 5.1: Data analysis strategy.

the helicity cycle \pm , respectively, E' their energy, ϕ and θ the polar scattering angles (see Figure 5.2). The target density and polarization are n_t and P_t , respectively, and $\Delta E' \Delta \Omega$ is the energy-acceptance bin over which the cross section is averaged. The polarized cross sections are diluted by the beam and target polarizations, which have to be divided out. Figure 5.1 displays schematically the general data analysis strategy. The initial counts N^\pm are filtered through the electron identification algorithms, and the detector inefficiencies are taken into account, obtaining thus the good electron counts N_e^\pm . The experimental (radiated) cross sections are then obtained from equation 5.1. These have to be corrected for external and internal radiation in order to arrive at the polarized Born cross sections, σ_{\parallel}^\pm and σ_{\perp}^\pm (defined in Section 5.6), from which the main physical observables are extracted,

namely the spin structure functions and the sum rules. These obviously refer to ^3He , and to extract the same observables for the neutron, a nuclear model is needed.

5.3 Spectrometer Optics and Acceptance

The variables needed for the physics analysis are the coordinates of the interaction point of the scattered electron in the target, x_t, y_t, z_t (see Figure 5.2(a)), the scattering angle θ_t (transverse plane), ϕ_t (horizontal plane) and the momentum p . However, the VDC's measure the scattered electron coordinates in the focal plane, that is the focal plane crossing (x_f, y_f) and the direction (θ_f, ϕ_f) where x_f and θ_f are the dispersive variables. If the first set of variables is denoted by the vector $T = (x_t, y_t, z_t, \theta_t, \phi_t, p)$ and the second by the vector $F = (x_f, y_f, \theta_f, \phi_f)$, then the two sets are connected by the magnetic transport matrix \mathcal{M} , $T = \mathcal{M}F$. The reconstruction from the focal plane to the target is done assuming a thin target ($z_t = 0$) and a centered beam. The raster and beam position information allow the determination of x_t and z_t . A first approximation of the magnetic transport matrix is obtained by the knowledge of the spectrometer magnetic field and the spectrometer and target position offsets as measured by the survey team. The matrix elements are

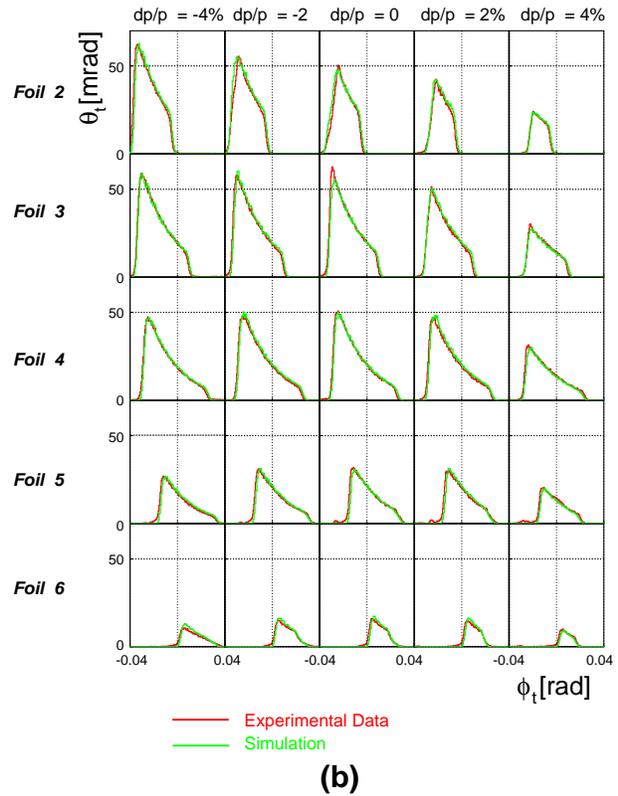
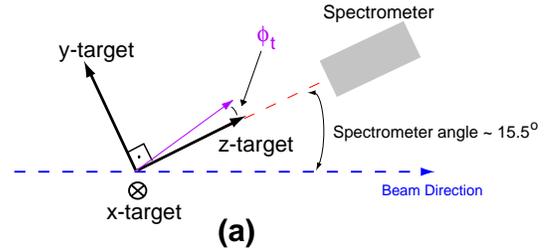


Figure 5.2: (a) Target coordinate system. The transverse scattering angle θ_t is not shown. (b) Comparison of experimental and simulated ^{12}C data for different momenta.

then optimized by using real data obtained during the experiment with the ^{12}C foils (see Figure 3.13). Seven foils (thickness=51.46 mg/cm²) were spaced by 7 cm along the beam direction. Data were taken at 0.862 GeV with the spectrometer collimator in and out, and with a sieve-slit (a tungsten plate with holes at known positions). The reconstruction of the foil positions and the sieve-slit holes allows the optimization of the magnetic transport matrix elements. The same data was used to understand the spectrometer acceptance, using the elastic $^{12}\text{C}(e, e')$ scattering. The world data [4] on the carbon elastic form factors were used for a simulation of the experimental data. The comparison between the two is shown in Figure 5.2(b). The uncertainty in the knowledge of the acceptance resulting from this study [1] is less than 4%.

5.4 Elastic Cross Sections and Asymmetries

5.4.1 Elastic Cross Sections

The elastic $^3\text{He}(e, e')$ scattering can be used as an independent systematic check for the understanding of the experimental apparatus and data analysis. The $^3\text{He}(e, e')$ elastic cross section is

$$\left(\frac{d\sigma}{d\Omega}\right)_{elastic} = \sigma_{Mott} \frac{E'}{E} \left[\frac{G_E^2 + \tau G_M^2}{1 + \tau} + 2\tau \tan^2 \frac{\theta}{2} G_M^2 \right] \quad (5.2)$$

with $\tau = Q^2 / 4M^2$, M the ^3He mass and $G_E(Q^2)$, $G_M(Q^2)$ are the electric and magnetic ^3He elastic form factors, respectively. The Mott cross section is

$$\sigma_{Mott} = \frac{\alpha^2 \cos^2 \frac{\theta}{2}}{E^2 \sin^4 \frac{\theta}{2}} \quad \theta=15.5^\circ \quad \frac{15.4}{E^2 [\text{GeV}^2]} \mu\text{barn} \quad (5.3)$$

The energy and scattering angle of the elastically scattered electrons, incident with energy E , are correlated:

$$E' = \frac{E}{1 + \frac{2E}{M} \sin^2 \frac{\theta}{2}} \quad (5.4)$$

The shape of the elastic peak as a function of invariant mass W is shown in Figure 5.3 for one out of the two energies at which elastic data was taken during E-94010, namely 0.862

GeV and 1.718 GeV. The elastic form factors entering equation (5.2) are known to 2% [2]. Folding in radiative and acceptance effects the known elastic cross section was used [3] to

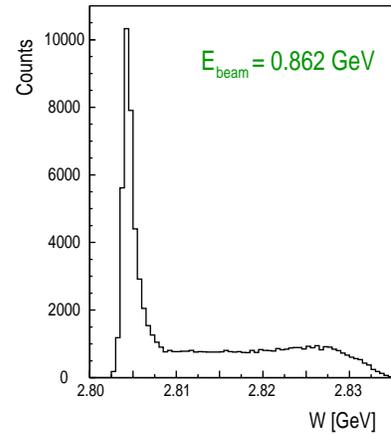


Figure 5.3: ^3He Elastic peak.

simulate the experimental data. Indicative results of the comparison between real and simulated data at 1.717 GeV are shown in Figure 5.4. Similar results are obtained for the data at 0.862 GeV. The dominant contributions to the uncertainty on the real data cross sections are the target density (3%), the effect of the beam energy uncertainty, which due to the strong Q^2 dependence of the elastic cross section (stemming from the Mott cross section and the elastic form factors) results in an error of 2.5%, and the spectrometer

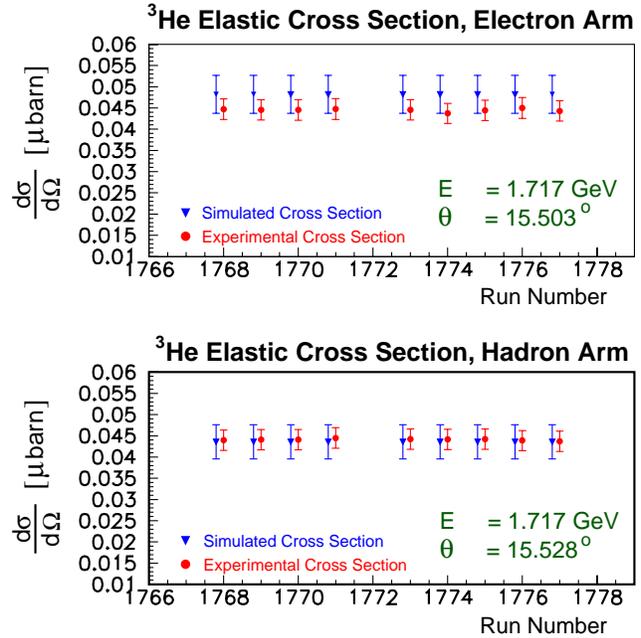


Figure 5.4: ^3He Elastic cross section.

angle uncertainty ($\pm 0.8 \text{ mrad}$, resulting in a 3% cross section error). The uncertainty of the beam current and the nitrogen dilution add each 1%. Finally, the statistical error is negligible. Added in quadrature, these uncertainties yield a total error of $\pm 5.0\%$ and $\pm 6.3\%$ for the 0.862 GeV and 1.717 GeV data, respectively. On the other hand, the uncertainty of the simulated data mainly consists of two contributions : the uncertainty due to the form factor error (4%) and the acceptance error (4%). The uncertainty in the target material crossed by the electrons propagates through the radiative corrections into a 0.6% cross section error. The total uncertainty for the simulated data is thus $\pm 6.4\%$.

5.4.2 Elastic Yield in Reference Cell Data

While the measurement of the elastic cross sections serves as a systematic check of the combined behavior of the spectrometer and the ^3He target, a relative measurement of elastic yields using the reference cell results in a straightforward check of the ^3He target density. We used the reference cell filled with ^3He at three different and known densities, namely 5.0, 6.8 and 8.2 amg. These densities are extracted from the fill pressure of the reference cell and the measured temperature. Any density variation in the beam path due to beam heating has been estimated to be negligible, less than 1%. We measured the counts under the elastic

peak with the reference cell as well as with the ^3He target cell 'BeHappy' at $E_{beam}=1.72$ GeV. Using the known reference cell densities, the ^3He density in the target cell can be extracted. The measurement has been used as a separate estimate of the temperature difference Δ , defined in (4.90). The latter is the difference of the actual pumping chamber temperature from the average temperature measured by the two RTD's attached on the pumping chamber. The ^3He density in the target chamber depends on Δ , because the temperature distribution in the cell determines the ^3He density in each of its parts.

In Figure 5.5 we plot Δ as a function of the ^3He target density. The blue error band represents the uncertainty in the knowledge of the room-temperature density of 'BeHappy'. It actually determines the accuracy with which Δ can be determined. The target density measured with the previously described method is a line perpendicular to the x-axis (density axis) in Figure 5.5. The intersection of this line with the blue band will determine Δ . The grey band around this line represents the error of the density measurement. The latter is complicated by

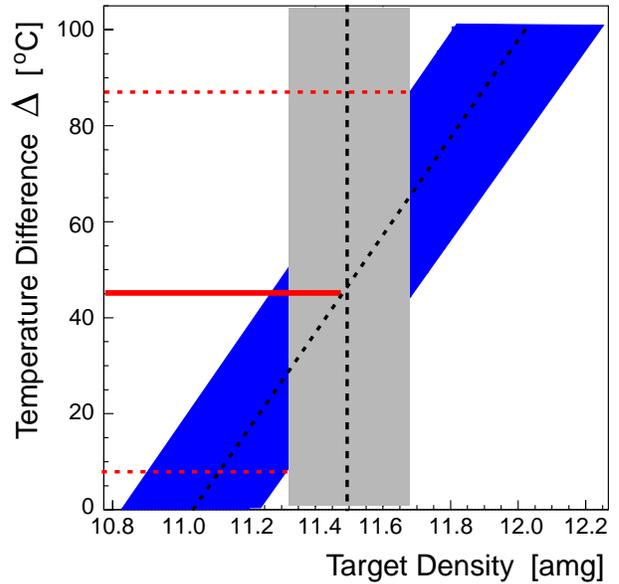


Figure 5.5: Extraction of Δ from reference cell data.

the fact that the reference cell and target cell wall thicknesses (the thickness of the glass of the target chamber cylinder) are different by about 50%, owing to the different glass they were made of (the reference cell was made out of GE-180, the raw tubing of which is 1.67 mm thick, whereas the target cell was made out of Corning 1720, with a 1.11 mm thick tubing. The raw tubes were resized, but the difference in the final thickness is approximately preserved). This difference propagates with a similar magnitude in the radiative corrections to the elastic peak. Since the exact thickness of the target chamber wall of the reference and the target cells was not known, we used the simulation of the elastic peak mentioned in the previous section to fit the data, extract an approximate thickness and apply the corresponding radiative correction factor to the elastic yield. The error in the

extracted ^3He density resulting from this procedure is about 1.5%, represented by the grey band in Figure 5.5. The resulting estimate for Δ is $\Delta \approx 45 \pm 40$ °C, in agreement with the other two estimates described in Section 4.6.3 .

5.4.3 Elastic Asymmetries

The elastic asymmetry for polarized electron-polarized ^3He scattering is [5]

$$A_{\parallel} = -P_{target}P_{beam} \frac{2\tau v_{T'} \cos\theta^* G_M^2 + 2\sqrt{2\tau(1+\tau)} v_{TL'} \sin\theta^* \cos\phi^* G_M G_E}{v_L(1+\tau)G_E^2 + 2\tau v_T G_M^2} \quad (5.5)$$

where $v_{T'}$, $v_{TL'}$, v_L and v_T are kinematic factors. θ^* and ϕ^* are the polar and azimuthal angles of the ^3He spin with respect to the 3-momentum transfer vector \mathbf{q} ($q_{\mu} = (\nu, \mathbf{q})$).

The results of the comparison between the expected (simulated) and measured asymmetries at 1.717 GeV are shown in Figure 5.6. The error bars on the measured asymmetries are statistical only, whereas the error bars of the simulation contain the systematic errors. The expected asymmetry is calculated from (5.5) by folding in the acceptance effects [3], and taking into account the beam and target polarizations. The dominant contributions to the uncertainty stem from the beam and target polarimetries (3% and 4%, respectively), and the elastic form factors (4%). The total systematic error is 6.5% (relative). This comparison provides an important independent check of the combined consistency of beam and target polarimetries.

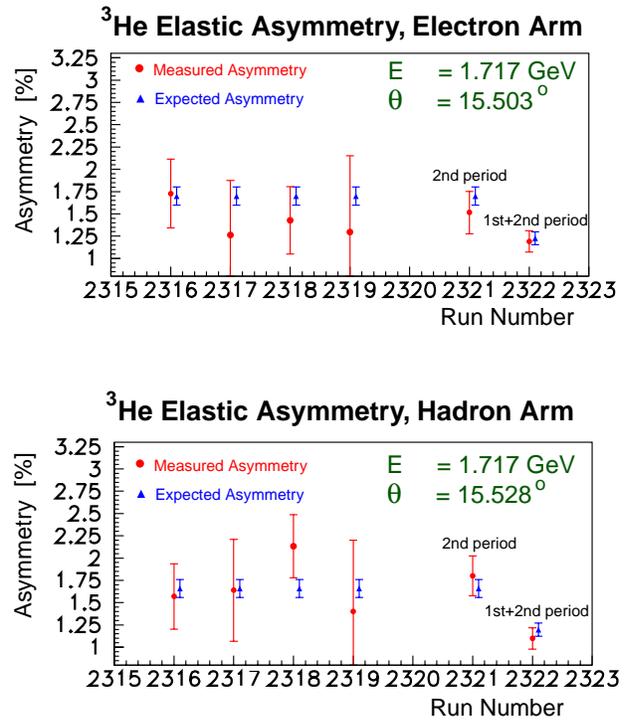


Figure 5.6: ^3He Elastic asymmetry.

5.5 Radiative Corrections

The effects of internal and external radiation have to be unfolded from the measured cross sections in order to extract the Born cross sections. As shown in Figure 5.7, the radiation of soft and hard photons from the electron lines carries away energy and momentum, distorting the kinematic interpretation (x, Q^2) of the events. The spectrometers have a resulting response in the (x, Q^2) plane that reaches to large parts of the plane. The purpose of the radiative corrections is to unfold this response and deduce the cross sections at the specific (x, Q^2) point.

Figure 5.7(a) shows the scattered energy (E') versus incident energy (E) kinematic plane. A spectrometer setting defines a point (or a small region, taking into account the finite resolution) on this plane, into which counts fall. In the presence of radiation counts fall into this region from distant points on the plane. Radiation before (after) the scattering reduces the value of E (E') and moves events from the horizontal (vertical) side of the triangle into the detection region. The triangle is bounded by the line defined by the elastic scattering correlation (5.4), from which events can be only radiated away. Figure 5.7(b) shows the locus of the triangle on the $x - Q^2$ plane.

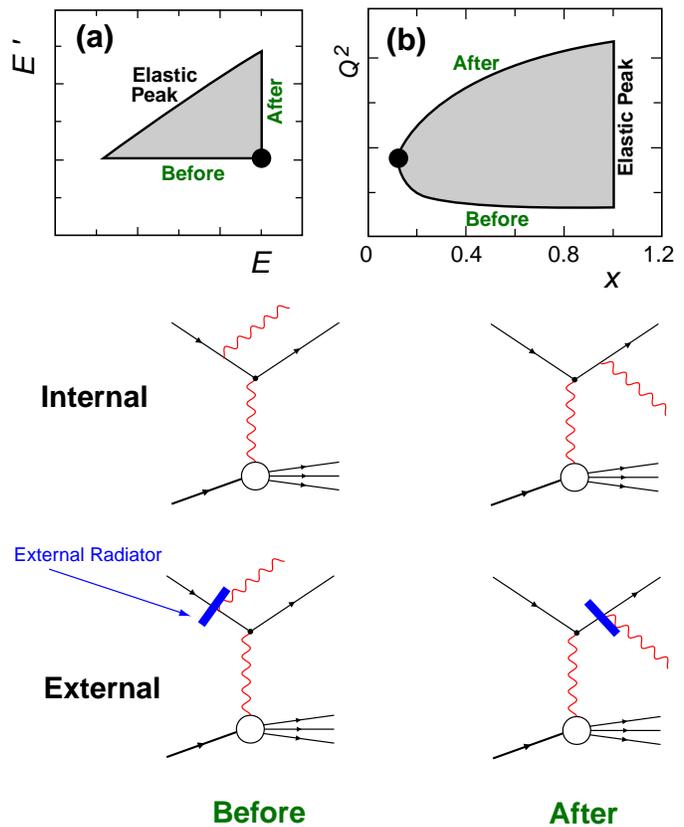


Figure 5.7: Effects of internal and external radiation on the kinematic dependence of the cross section, from [6].

5.5.1 External Radiative Effects

The externally radiated cross section is given by the following convolution integral

$$\sigma_{exp}(E_s, E_p) = \int_{t_{min}}^{t_{max}} \frac{dt}{T} \int_{E_s^{min}}^{E_s} dE'_s \int_{E_p}^{E_p^{max}} dE'_p I(E_s, E'_s, t) \sigma_{int}(E'_s, E'_p) I(E'_p, E_p, t_{exit}) \quad (5.6)$$

where $\sigma_{exp}(E_s, E_p)$ is the measured cross section with incident (detected) electron energy E_s (E_p), $I(E_s, E'_s, t)$ is the probability of an electron of incident energy E_s to loose the energy $E_s - E'_s$ after traversing a material thickness t , $\sigma_{int}(E'_s, E'_p)$ is the internal cross section for an electron of energy E'_s to be scattered into an energy E'_p , and $I(E'_p, E_p, t_{exit})$ the probability of an electron of scattered energy E'_p to loose the energy $E'_p - E_p$ after traversing the exit material thickness t_{exit} . The probability $I(E, E', t)$ is given in [7][8]. It should be noted that the external radiative corrections are independent of the polarization of the incident electron beam.

5.5.2 Internal Radiative Effects

The calculation of the internal cross section σ_{int} involves the polarization of the electron and the target. A customized form of the code POLRAD [9] was used. This code was designed for polarized DIS scattering, and in its original form the quasi-elastic tail is calculated starting from a delta-function at the position $\nu = Q^2/2M_N$, where M_N is the nucleon mass. Since the shape of the quasi-elastic peak has been measure in this experiment, POLRAD was modified [10] to accommodate the actual shape.

5.5.3 Iteration

The final goal of the radiative corrections is to determine the Born cross section $\sigma_{Born}(E_s, E_p)$, which, when radiated (internally and externally), produces the measured cross section σ_{exp} . The process of unfolding σ_{exp} to extract σ_{Born} is iterative. Since the form of the latter is not known, we use σ_{exp} as an initial guess. The iteration proceeds in the following manner:

1. $\sigma_{guess} = \sigma_{exp}$
2. Radiate $\sigma_{guess} \rightarrow \sigma_{rad}$
3. Modify σ_{guess} , $\sigma_{guess}^{new} = \sigma_{exp}/\sigma_{rad}$
4. Go to step 2.

The iteration typically converges after four or five passes, at which point σ_{guess} changes by only 1-2%.

5.5.4 Unpolarized Cross Sections

Figure 5.8 shows the measured unpolarized cross section σ_0 for all six beam energies as a function of energy loss ν . We show the cross section before and after radiative corrections

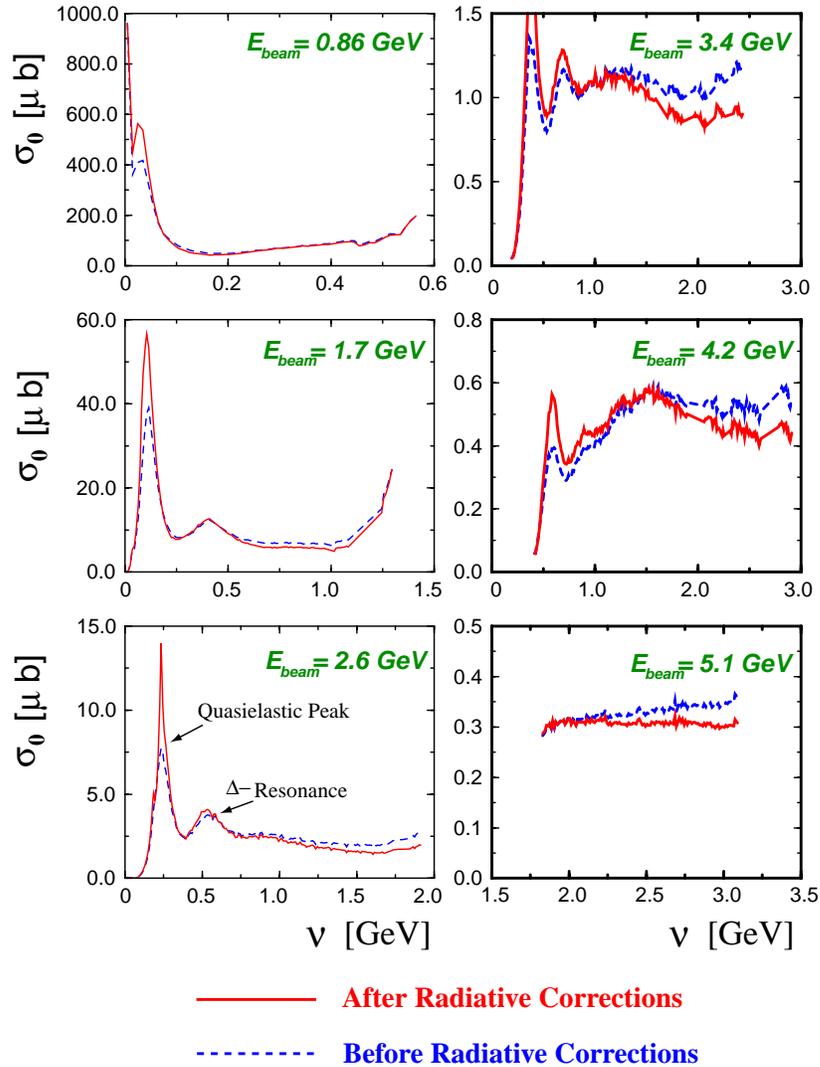


Figure 5.8: Unpolarized cross sections as a function of energy loss ν , with and without radiative corrections.

have been applied [10]. One can clearly see the quasielastic peak and the Δ -resonance. Due

to the inclusive nature of the measurement and the smearing due to nuclear effects, such as Fermi motion, other resonances cannot be resolved. The rapid decrease of the cross section with beam energy is a direct manifestation of the Q^{-4} dependence of the Mott cross section. Furthermore, with increasing beam energy, the peak-structure gradually disappears into a flat response, signifying the onset of the deep inelastic regime.

5.6 Extraction of $g_1^{3\text{He}}$ and $g_2^{3\text{He}}$

After determining the polarized Born cross sections, the ^3He spin structure functions $g_1(\nu, Q^2)$ and $g_2(\nu, Q^2)$ can be readily extracted from the longitudinal and transverse cross section differences. From (2.1) it follows that when the ^3He spins are parallel to the beam direction, the longitudinal cross section difference is

$$(\Delta\sigma)_L \equiv \frac{d^2\sigma^{\leftarrow\rightarrow}}{d\Omega dE'} - \frac{d^2\sigma^{\rightarrow\rightarrow}}{d\Omega dE'} = \frac{4\alpha^2}{Q^2} \frac{1-y}{M} \left[\frac{1+(1-y)\cos\theta}{y} g_1 - \frac{2Mx}{\nu} g_2 \right] \quad (5.7)$$

where y is the electron fractional energy loss,

$$y = \frac{E - E'}{E} \quad (5.8)$$

In the above definition the first (second) superscript arrow refers to the electron (^3He) spin. Similarly, when the ^3He spins are transverse to the beam direction, the transverse cross section difference is

$$(\Delta\sigma)_T \equiv \frac{d^2\sigma^{\leftarrow\downarrow}}{d\Omega dE'} - \frac{d^2\sigma^{\rightarrow\downarrow}}{d\Omega dE'} = \frac{4\alpha^2}{Q^2} \frac{(1-y)^2}{My} \left[g_1 + \frac{2}{y} g_2 \right] \quad (5.9)$$

Since $(\Delta\sigma)_L$ and $(\Delta\sigma)_T$ are measured, equations (5.7) and (5.9) can be solved for g_1 and g_2 . Figures 5.9 and 5.10 show the ^3He spin structure functions g_1 and g_2 for all six beam energies as a function of energy loss ν , whereas Figures 5.11 and 5.12 show the same structure functions at constant Q^2 , as a function of x . Similar comments regarding the Q^2 evolution of the structure functions apply here, as in the case of the unpolarized cross sections. The decrease of the latter with increasing Q^2 is the reason for the increasing statistical error bars of the structure functions. By observing the Δ -resonance peak in $g_1(x)$ and $g_2(x)$, it can be noticed that, approximately, $g_2(x) \approx -g_1(x)$. This can be attributed to the M1 nature of the Δ transition: this implies that the exchanged photon is primarily transverse. Therefore the longitudinal cross section as well as the longitudinal-transverse interference

cross section is small. Since the latter is proportional to $(g_1 + g_2)$, as can be seen from (2.46), it follows that $g_1 + g_2 = 0$. Because of the non-resonant background below the Δ -peak, this equality is not exactly fulfilled.

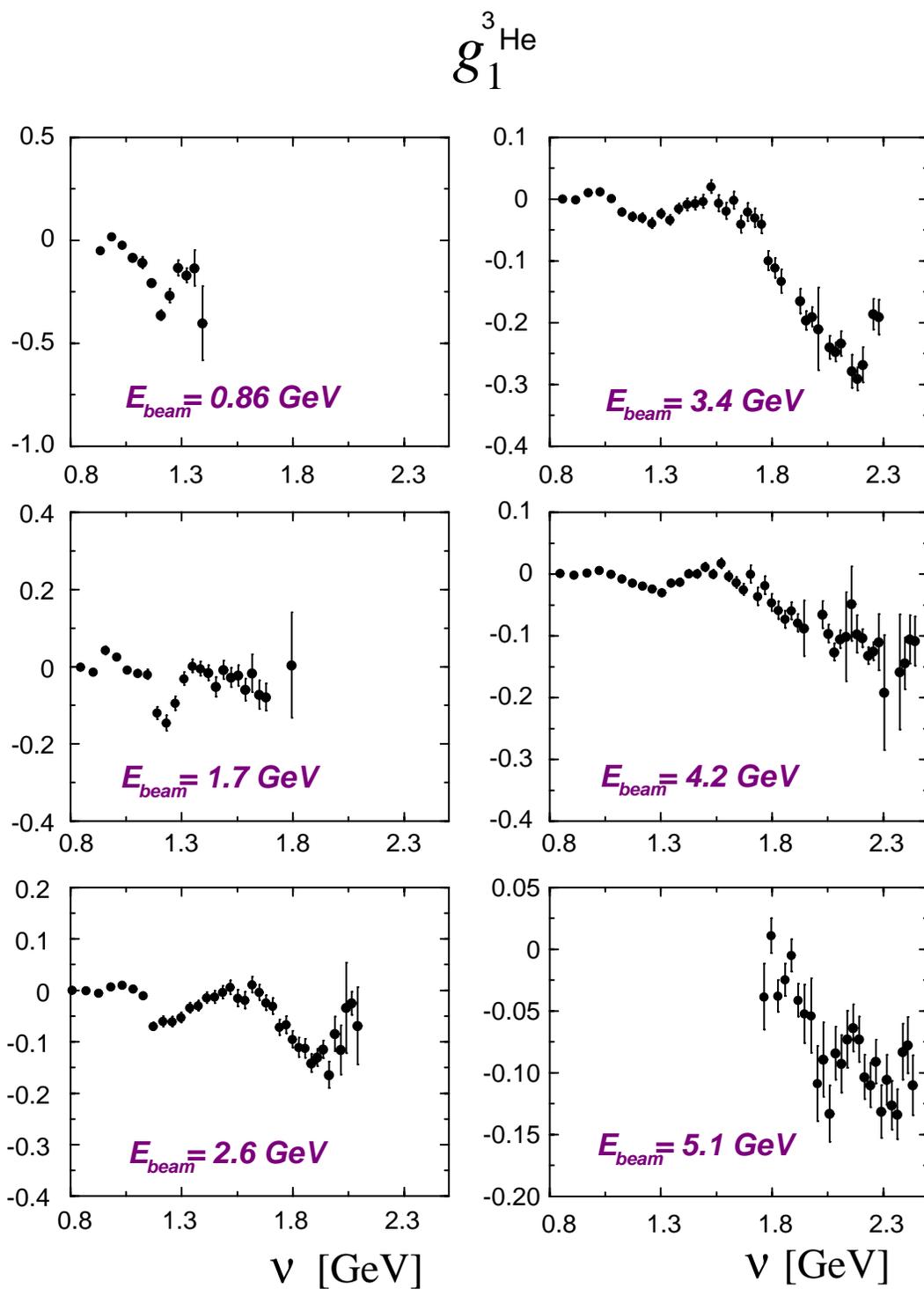


Figure 5.9: ^3He spin structure functions $g_1^{3\text{He}}$ as a function of energy loss ν . Errors are statistical only.

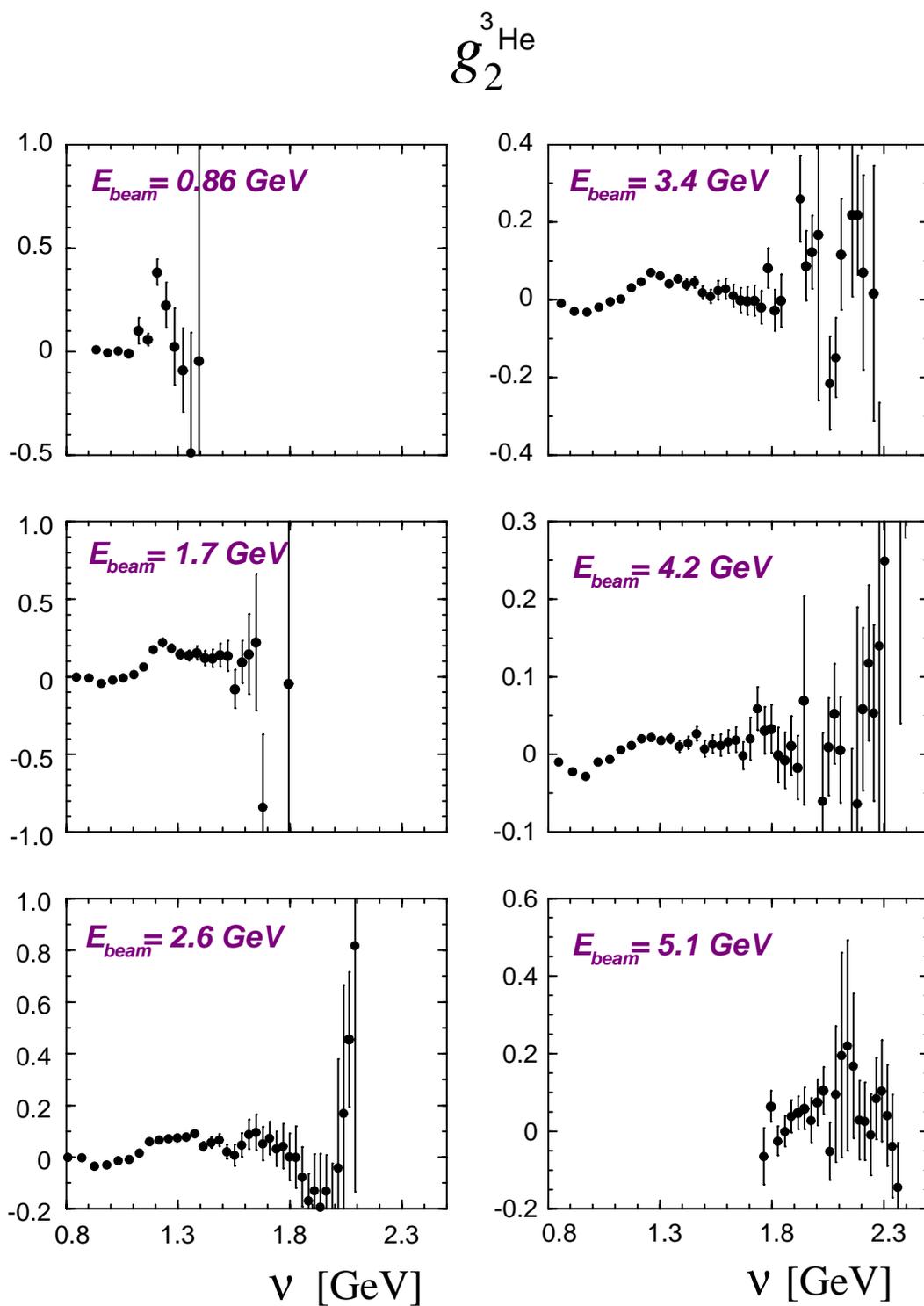


Figure 5.10: ^3He spin structure functions $g_2^{3\text{He}}$ as a function of energy loss ν . Errors are statistical only.

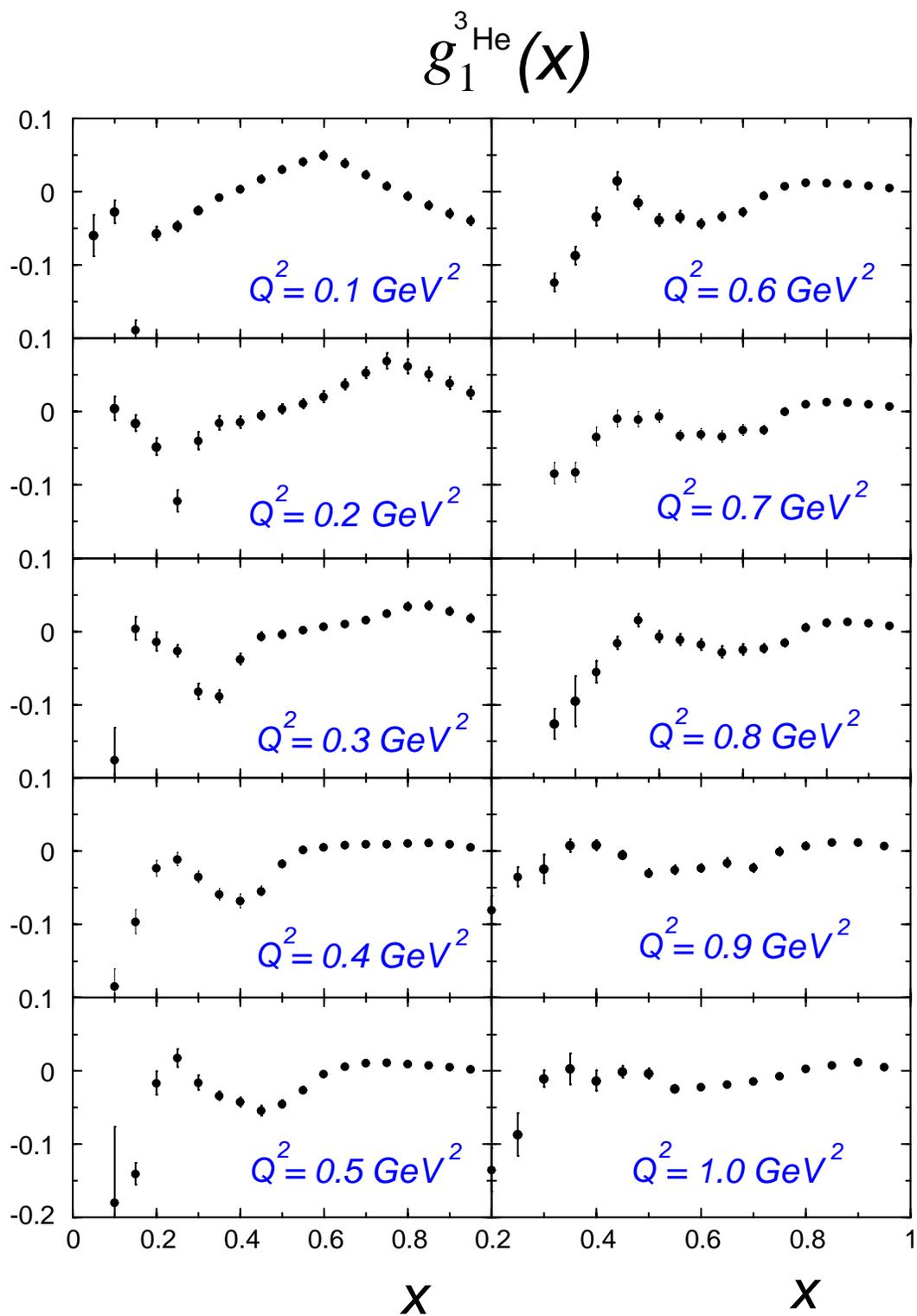


Figure 5.11: ^3He spin structure functions $g_1^{3\text{He}}$ as a function x .

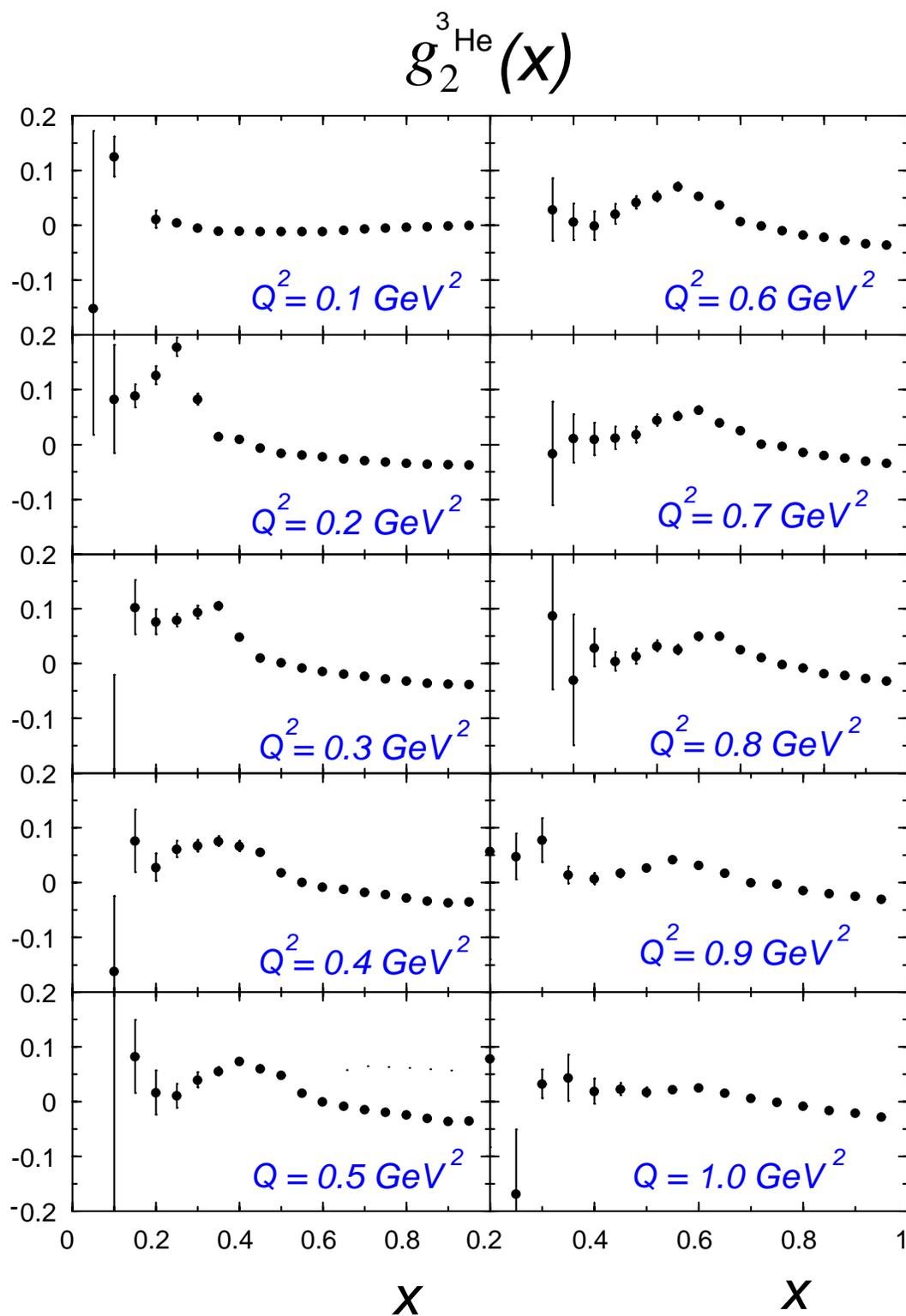


Figure 5.12: ^3He spin structure functions $g_2^{3\text{He}}$ as a function of x .

5.7 Extraction of Neutron Observables from ^3He Observables

5.7.1 Spin Structure Functions

To extract the neutron spin structure functions from the measured ^3He ones, a model for the ^3He nucleus is needed.

Naive Nuclear Model

Let $P_{p(n)}^{(\pm)}$ represent the probability to have a proton (neutron) with its spin parallel (+) or antiparallel (-) to the ^3He spin [11]. In the naive nuclear model that assumes the ^3He nuclear ground state is a pure S -state, $P_n^{(+)} = 1$, and $P_n^{(-)} = 0$, whereas $P_p^{(+)} = P_p^{(-)} = \frac{1}{2}$. In this case, the neutron and ^3He spin structure functions coincide, i.e. $g_1^n = g_1^{^3\text{He}}$. This model is completely inadequate, since it neglects the effective nucleon polarizations within the ^3He nucleus resulting from the S' and D wavefunction components.

Realistic ^3He Wavefunction

In the more realistic model of the ^3He wavefunction, the S' and D components modify the probabilities $P_{p(n)}^{(\pm)}$, which now are

$$P_n^{(+)} = 1 - \Delta, \quad P_n^{(-)} = \Delta \quad (5.10)$$

$$P_p^{(\pm)} = \frac{1}{2} \pm \Delta' \quad (5.11)$$

From three-body system calculations it follows that [12] $\Delta = 0.07 \pm 0.01$ and $\Delta' = 0.014 \pm 0.002$. Thus the effective neutron and proton polarizations in ^3He , $p_{p(n)}$, are

$$p_n = P_n^{(+)} - P_n^{(-)} = 0.86 \pm 0.02 \quad (5.12)$$

$$p_p = P_p^{(+)} - P_p^{(-)} = -0.028 \pm 0.004 \quad (5.13)$$

The ^3He spin structure function is now "diluted" by the proton contribution:

$$g_1^{^3\text{He}} = 2p_p g_1^p + p_n g_1^n \quad (5.14)$$

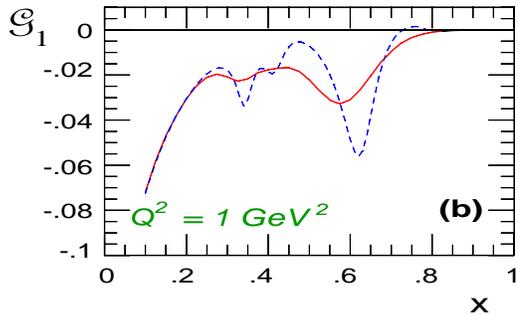
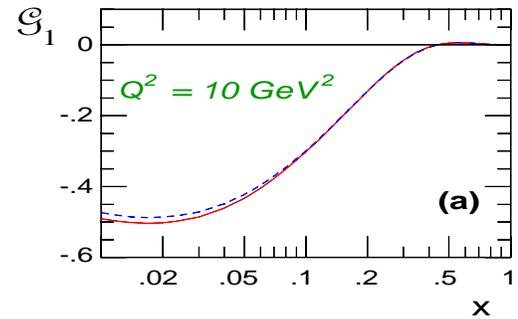


Figure 5.13: Model calculations of the structure function $\mathcal{G}_1^{^3\text{He}}$ in (a) the DIS region, and (b) the resonance region.

This approach completely ignores the Fermi motion of the nucleons and the binding effects. It is, though, highly successful in the DIS region, as shown in Figure 5.13(a), where the function \mathcal{G}_1^{3He} is plotted, where

$$\mathcal{G}_1^{3He} \equiv \frac{1}{1+\gamma^2} \left(g_1^{3He}(\nu, Q^2) - \gamma^2 g_2^{3He}(\nu, Q^2) \right) \quad (5.15)$$

with $\gamma = \frac{Q}{\nu}$. The full (red) curve is the exact calculation based on the convolution model [13]. This model convolves the polarized spectral function of ${}^3\text{He}$ with the nucleon structure functions as input. The latter are obtained by considering the contributions of a number of resonances ($P_{33}(1232)$, $D_{13}(1520)$, $S_{11}(1535)$ and $F_{15}(1680)$), which have been parametrized using existing unpolarized electroproduction data [14]. The dashed (blue) curve is obtained with the same input, but using (5.14), that is, by considering the effective nucleon polarizations as the only relevant nuclear effects. The reason that this approximation is adequate in the DIS region is that as $Q^2, \nu \rightarrow \infty$, the interaction time of the virtual photon with the nucleon is short, compared to typical nucleon energies. Thus there is not enough time for the photon to "feel" the nuclear binding effects. Quite the contrary happens in the resonance region ($Q^2 \leq 1 \text{ GeV}^2$), as shown in Figure 5.13(b).

5.7.2 Generalized GDH Integral

Fortunately enough, the difficulty of extracting the neutron spin structure functions from the ${}^3\text{He}$ ones in the resonance region does not persist in the extraction of the generalized GDH integral. Figure 5.14 shows the integral I_1 for ${}^3\text{He}$ (dots) calculated within the convolution model, compared with the one computed using (5.14) (crosses). As seen the difference is at most 5%. The full line is the free neutron integral.

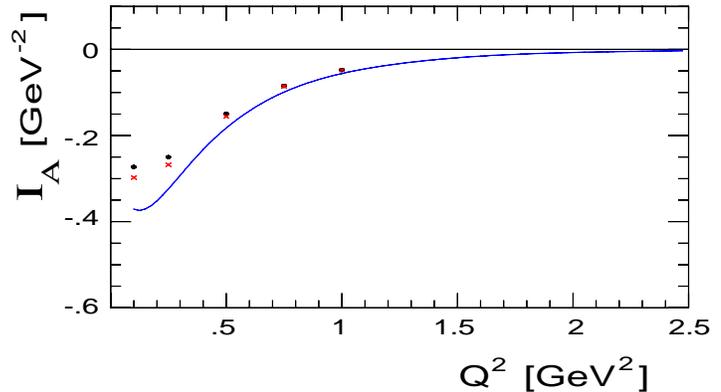


Figure 5.14: Integral of \mathcal{G}_1^{3He} .

5.8 Measurement of GDH Integral

In Figure 5.15 we show the transverse-transverse cross section defined in (2.48) as a function of ν , interpolated at constant Q^2 . Apart from the energy loss (ν) denominator, σ'_{TT} is the integrand entering the GDH integral, that was defined in (2.62). The latter is shown for ^3He in Figure 5.16. In the same Figure we also show the GDH integral I_1 for the neutron. This is simply extracted by applying the ratio of $\frac{I_{Scopetta}^n}{I_{Scopetta}^{^3\text{He}}}$ [13] to the ^3He GDH integral. Both of these integrals, $I_{Scopetta}^n$ and $I_{Scopetta}^{^3\text{He}}$, were shown in Figure 5.14. On the same Figure we superimpose the prediction of the UIM model discussed in Section 2.4.4, along with DIS Hermes data. One can see that $I_1(Q^2)$ qualitatively follows the model prediction. However, it is premature to gauge the quantitative agreement between theory and data, for the following reasons:

(i)

Some of the systematic errors of our measurement have not yet been finalized (in the following no error is quoted for them). The main contributions to the systematics come from (i) target polarization and density (3%), (ii) beam polarization (3%), (iii) spectrometer acceptance (4%), (iv) radiative corrections, (v) kinematic interpolation and (vi) neutron extraction.

(ii)

The energy integration domain for our data is not the same with the one used in the UIM model. The latter integrates σ'_{TT}/ν up to $W=2$ GeV, while our integration interval depends on Q^2 .

5.9 Summary and Outlook

Experiment E-94010 mapped the dramatic Q^2 -evolution of the extended GDH integral of the neutron over a wide Q^2 -range for the first time. Our data will provide a strong constraint for theoretical calculations and phenomenological models trying to describe the structure of the nucleon over the complete kinematic regime, that is, from the real photon point ($Q^2=0$), through the transition from hadronic- to quark-like behavior to the deep inelastic regime. Furthermore, we have motivated the study of the neutron's spin structure at lower Q^2 . Using a new device (septum magnets), experiment E-97110 (scheduled to

run in experimental Hall-A at Jlab) will reach a squared momentum transfer as low as $Q^2 \approx 0.005 \text{ GeV}^2$. This will allow to disentangle model calculations in this regime and test the chiral perturbation theory predictions. It will also permit the check of the GDH sum rule for the neutron and complement the data provided by our experiment.

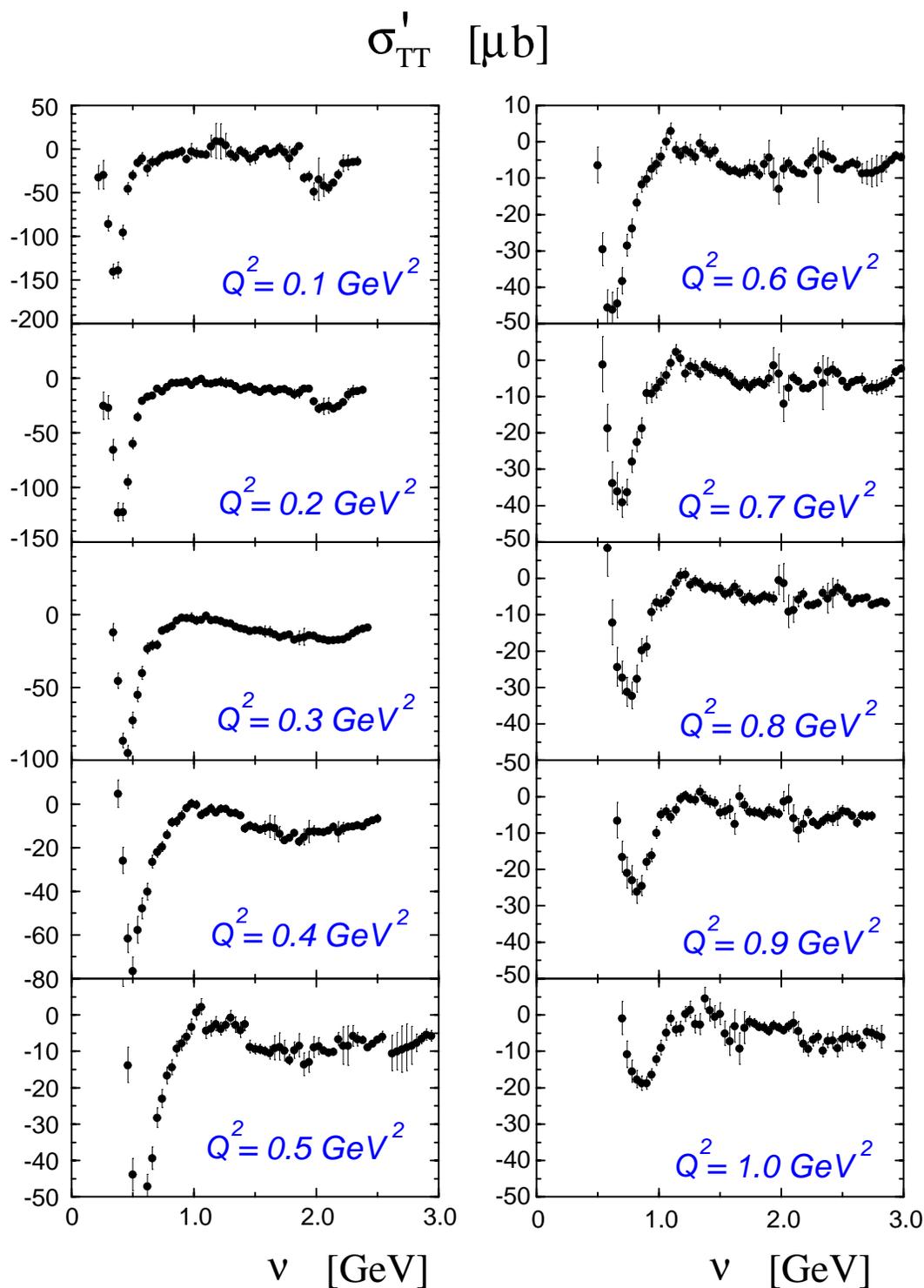


Figure 5.15: σ'_{TT} as a function of energy loss ν , at constant Q^2 .

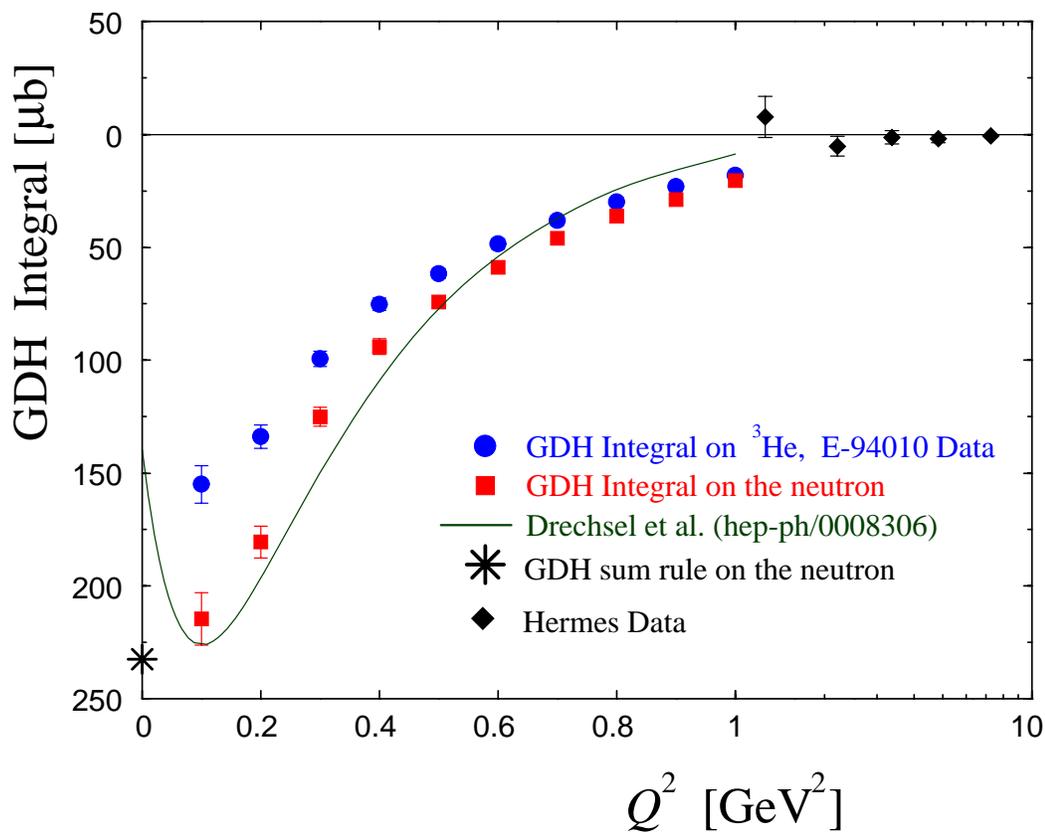


Figure 5.16: Measured ^3He GDH integral, extracted neutron integral and UIM prediction. The DIS Hermes data are from [15].

Bibliography

- [1] X. Jiang, Private Communication
- [2] A. Amroun *et al*, Nucl. Phys. A579, 596 (1994)
- [3] A. Deur, Ph.D. Thesis, University Blaise Pascal, 2000
- [4] L.S. Cardman *et al*, Phys. Lett. **B91**, 203 (1980)
- [5] T.W. Donnelly and A.S. Raskin, Ann. Phys. **169**, 247 (1986)
- [6] C.Y. Prescott, International School of Nucleon Structure, Ed. B. Frois, V.W. Hughes and N. De Groot, World Scientific, Singapore, 1997
- [7] L.W. Mo and Y.S. Tsai, Rev. Mod. Phys. **41**, 205 (1969)
- [8] Y.S. Tsai, SLAC Publications SLAC-PUB-848, 1971
- [9] I. Akushevich *et al*, Comput. Phys. Commun. **104**, 201 (1997)
- [10] S. Choi, Private Communication
- [11] C. Ciofi degli Atti, S. Scopetta, E. Pace and G. Salme, Phys. Rev. C **48**, R968 (1993)
- [12] J.L. Friar *et al*, Phys. Rev. C **42**, 2310 (1990)
- [13] S. Scopetta, A.Y. Umnikov, C. Ciofi degli Atti and L.P. Kaptari, nucl-th/9709015
- [14] V. Burkert and Z. Li, Phys. Rev. D **47**, 46 (1993)
- [15] K. Ackerstaff *et al*, Phys. Lett. **B444**, 531 (1998)

Particle Identification Cuts and Efficiencies

In the following tables we provide the applied cuts the the corresponding electron identification efficiencies along with the pion contamination for the Electron- and the Hadron-Arm. At $E_{beam}=862$ MeV the pion dilution is too small to be measured.

Table A.1: Shower Cuts and Efficiencies, $E_{beam} = 862$ MeV

p_0 (MeV)	E-ARM						H-ARM			
	π/e	E_{psh}/p Cut	E/p Cut	Tot. Eff.	Tot. Rej.	π Ct.(%)	π/e	Cer_{rej}	π Dilution (%)	
897.0	0.12	0.11	0.73	0.993	1.9	6.530	0.01	-	-	
862.0	0.03	0.10	0.74	0.994	1.8	1.824	0.00	-	-	
851.0	0.04	0.10	0.74	0.994	1.3	2.906	0.00	-	-	
828.0	0.03	0.09	0.73	0.993	2.0	1.553	0.01	-	-	
808.0	0.04	0.10	0.73	0.995	1.6	2.305	0.01	-	-	
746.0	0.03	0.13	0.72	0.995	2.7	1.144	0.01	-	-	
689.0	0.05	0.12	0.70	0.995	2.6	1.766	0.02	-	-	
587.0	0.04	0.10	0.68	0.995	3.2	1.404	0.02	-	-	
542.0	0.05	0.13	0.66	0.995	2.9	1.561	0.02	-	-	
461.0	0.04	0.14	0.64	0.995	3.0	1.472	0.02	-	-	
426.0	0.04	0.14	0.63	0.995	3.0	1.448	0.01	-	-	

Table A.2: Shower Cuts and Efficiencies, $E_{beam} = 1718$ MeV

p_0 (MeV)	E-ARM						H-ARM			
	π/e	E_{psh}/p Cut	E/p Cut	Tot. Eff.	Tot. Rej.	π Ct.(%)	π/e	Cer_{rej}	π Dilution (%)	
1730.0	0.09	0.09	0.80	0.976	4.0	2.283	0.02	2.3	0.87	
1607.0	0.01	0.09	0.80	0.993	2.3	0.627	0.00	100.0	0.00	
1484.0	0.03	0.09	0.79	0.990	17.0	0.167	0.02	11.5	0.17	
1369.0	0.04	0.09	0.78	0.989	32.3	0.116	0.03	143.3	0.02	
1264.0	0.05	0.09	0.77	0.993	70.0	0.078	0.06	21.7	0.26	
1167.0	0.11	0.10	0.76	0.993	142.9	0.075	0.11	317.8	0.04	
1077.0	0.18	0.12	0.75	0.995	219.3	0.083	0.19	75.4	0.25	
918.0	0.28	0.11	0.73	0.995	99.6	0.284	0.31	127.0	0.24	
847.0	0.36	0.12	0.73	0.995	64.1	0.556	0.38	131.7	0.29	
782.0	0.41	0.14	0.72	0.995	45.1	0.908	0.41	41.6	0.98	
666.0	0.46	0.12	0.70	0.996	24.1	1.894	0.52	119.7	0.44	

Table A.3: Shower Cuts and Efficiencies, $E_{beam} = 2584$ MeV

p_0 (MeV)	E-ARM						H-ARM		
	π/e	E_{psh}/p Cut	E/p Cut	Tot. Eff.	Tot. Rej.	π Ct.(%)	π/e	C_{errej}	π Dilution (%)
2479.0	0.08	0.05	0.70	0.974	12.8	0.611	0.01	2.4	0.25
2357.0	0.01	0.07	0.83	0.992	6.0	0.181	0.00	26.3	0.01
2175.0	0.03	0.06	0.82	0.987	20.8	0.137	0.02	20.1	0.08
2008.0	0.04	0.08	0.81	0.990	88.5	0.044	0.04	96.6	0.04
1854.0	0.10	0.08	0.80	0.990	187.6	0.056	0.10	71.1	0.15
1711.0	0.20	0.08	0.80	0.991	424.9	0.046	0.20	262.8	0.08
1579.0	0.33	0.08	0.80	0.992	625.8	0.053	0.36	123.6	0.29
1458.0	0.54	0.09	0.78	0.994	847.1	0.064	0.59	129.2	0.46
1346.0	0.80	0.10	0.78	0.995	1409.0	0.057	0.89	171.4	0.52
1242.0	1.08	0.09	0.77	0.993	1384.0	0.078	1.24	118.4	1.04
1147.0	1.38	0.09	0.76	0.992	1126.0	0.122	1.56	205.2	0.76
1059.0	1.61	0.09	0.76	0.993	857.9	0.188	1.86	143.5	1.30
977.0	1.77	0.10	0.74	0.995	696.8	0.253	2.07	166.9	1.24
902.0	1.83	0.12	0.73	0.995	412.3	0.443	2.18	161.1	1.35
832.0	1.97	0.12	0.72	0.995	249.5	0.788	2.27	237.7	0.96

Table A.4: Shower Cuts and Efficiencies, $E_{beam} = 3385$ MeV

p_0 (MeV)	E-ARM						H-ARM		
	π/e	E_{psh}/p Cut	E/p Cut	Tot. Eff.	Tot. Rej.	π Ct.(%)	π/e	C_{errej}	π Dilution (%)
2796.0	0.03	0.09	0.83	0.988	37.0	0.081	0.02	9.1	0.26
2580.0	0.06	0.05	0.81	0.979	91.7	0.065	0.06	53.8	0.10
2199.0	0.23	0.09	0.81	0.992	385.8	0.058	0.23	80.6	0.28
2030.0	0.40	0.09	0.80	0.990	727.1	0.056	0.44	173.8	0.25
1873.0	0.71	0.11	0.79	0.994	1556.0	0.045	0.75	139.0	0.54
1596.0	1.66	0.09	0.79	0.993	2430.0	0.068	1.78	145.6	1.22
1360.0	3.03	0.11	0.76	0.995	3070.0	0.099	3.28	177.8	1.84
1159.0	3.95	0.12	0.74	0.995	3051.0	0.130	4.58	157.0	2.92
988.0	4.31	0.09	0.73	0.993	1005.0	0.429	4.74	217.7	2.18

Table A.5: Shower Cuts and Efficiencies, $E_{beam} = 4240$ MeV

p_0 (MeV)	E-ARM						H-ARM		
	π/e	E_{psh}/p Cut	E/p Cut	Tot. Eff.	Tot. Rej.	π Ct.(%)	π/e	Cer_{rej}	π Dilution (%)
3631.0	0.02	0.06	0.87	0.989	16.5	0.111	0.27	123.2	0.22
3352.0	0.04	0.05	0.86	0.987	73.1	0.052	0.14	118.0	0.12
3086.0	0.08	0.06	0.85	0.987	168.3	0.047	0.53	129.5	0.41
2856.0	0.14	0.06	0.85	0.989	290.0	0.047	1.58	200.7	0.79
2636.0	0.26	0.06	0.84	0.987	459.5	0.057	1.53	181.7	0.84
2433.0	0.50	0.08	0.83	0.988	984.6	0.050	1.59	162.7	0.98
1767.0	3.32	0.07	0.80	0.986	2154.0	0.154	3.58	163.1	2.19
1389.0	7.07	0.09	0.78	0.987	3567.0	0.198	7.79	198.8	3.92

Table A.6: Shower Cuts and Efficiencies, $E_{beam} = 5059$ MeV

p_0 (MeV)	E-ARM						H-ARM		
	π/e	E_{psh}/p Cut	E/p Cut	Tot. Eff.	Tot. Rej.	π Ct.(%)	π/e	Cer_{rej}	π Dilution (%)
3086.0	0.31	0.06	0.82	0.988	652.8	0.047	0.33	93.3	0.35
2846.0	0.58	0.07	0.81	0.990	1036.0	0.056	0.59	91.1	0.65
2625.0	1.02	0.06	0.81	0.987	1443.0	0.071	1.05	170.1	0.62
2423.0	1.65	0.09	0.81	0.988	1976.0	0.083	1.67	147.4	1.13
2233.0	2.68	0.09	0.81	0.992	2644.0	0.101	2.67	134.6	1.98
2059.0	3.87	0.06	0.80	0.986	2327.0	0.166	4.07	170.7	2.39

Target Cell Volumes

Cell	Glass	Pumping Chamber Volume	Transfer Tube Volume	Target Chamber Volume	Total Volume
DontWorry	Corning ¹ 1720	107.7	6.5	82.8	197.0
Be Happy	GE ² 180	121.2	5.1	90.8	217.1
Armageddon	Corning 1720	96.3	4.9	86.9	188.1
Nepheli	Corning 1720	103.3	6.4	91.5	201.2
Sysiphos	Corning 1720	109.5	5.5	97.1	212.1
Jin	Corning 1720	101.0	8.4	90.1	199.5

$${}^1\rho_{1720} = 2.53 \text{ g/cc}$$

$${}^1\rho_{GE180} = 2.76 \text{ g/cc}$$

Target Cell Densities

Cell	D1	D2	Fill	Average
DontWorry	10.00 ± 0.17	9.92 ± 0.15	9.90 ± 0.22	9.94 ± 0.17
Armageddon	10.06 ± 0.17	10.22 ± 0.15	10.28 ± 0.23	10.17 ± 0.17
BeHappy	9.25 ± 0.15	9.37 ± 0.14	9.41 ± 0.20	9.33 ± 0.15
Nepheli	11.44 ± 0.19	11.29 ± 0.17	10.78 ± 0.42	11.31 ± 0.19
Sysiphos	8.27 ± 0.14	8.12 ± 0.12	8.15 ± 0.18	8.18 ± 0.14
Jin	8.43 ± 0.14	8.39 ± 0.13	8.43 ± 0.19	8.41 ± 0.14
Cuervo	10.23 ± 0.21	10.01 ± 0.17	9.66 ± 0.21	9.98 ± 0.21